IACMI/R0001-2022/3.12

Development of Large Scale Extrusion Deposition for Structural Applications

Authors:
Dylan Hoskins
Eduardo Barocio
David Koester
Dayakar Penumadu
Vidya Kishore
Akshay Jacob Thomas
William Henken
Jorge A. Ramírez
Seokpum Kim
Miguel Ramírez
Tyler Smith
Frye Mattingly
Chad Duty
Vlastimil Kunc

Date: 1/5/22

Final Technical Report
PA16-0349-3.12-01

Approved for Public Release.
Distribution is Unlimited.

The Institute for iacmi Advanced Composites Manufacturing Innovation
THE COMPOSITES INSTITUTE

U.S. DEPARTMENT OF ENERGY

The information, data, or work presented herein was funded in part by the Office of Energy Efficiency and Renewable Energy (EERE), U.S. Department of Energy, under Award DE-EE0006926

The authors would like to acknowledge Charlie Hill for his critical role in organizing this IACMI project. Much of what was accomplished could not have been achieved without his contributions. The authors would also like to acknowledge Dr. Kyle Rowe and Dr. Robert Bedsole for their guidance and help to complete the process variability printing and efforts to accomplishing the mechanical testing. A part of this research used resources at the Manufacturing Demonstration Facility (MDF), a DOE-EERE User Facility at Oak Ridge National Laboratory.

Development of Large Scale Extrusion Deposition for Structural Applications

Principal Investigator: Dylan Hoskins

Organization: Local Motors

Address: 2030 Valley Vista Rd, Knoxville TN 37932

Phone: 423-259-0781

Email: dhoskins@local-motors.com

Co-authors: Eduardo Barocio, David Koester, Dayakar Penumadu, Vidya Kishore, Akshay Jacob Thomas, William Henken, Jorge A. Ramírez, Seokpum Kim, Miguel Ramírez, Tyler Smith, Frye Mattingly, Chad Duty, Vlastimil Kunc

Date Published: (January, 2022)

Prepared by:
Institute for Advanced Composites Manufacturing Innovation
Knoxville, TN 37932
Managed by Collaborative Composite Solutions, Inc.
For the
U.S. DEPARTMENT OF ENERGY
Under contract DE- EE0006926

Project Period:
(05/2019 – 04/2021)

Approved For Public Release

TABLE OF CONTENTS

List of Acronyms

AM – Additive Manufacturing
ORNL – Oak Ridge National Laboratory
LSED – Large Scale Extrusion Deposition
NDE – Nondestructive Evaluation
NC – Numerical Code
ABS – Acrylonitrile Butadiene Styrene
IACMI – Institute for Advanced Composites Manufacturing Innovation
BAAM – Big Area Additive Manufacturing
ASTM – American Society for Testing and Materials
DMA – Dynamic Mechanical Analysis
DSC -Differential Scanning Calorimetry
TMA – Thermomechanical analysis
DIC – Digital Image Correlation
CTE – Coefficient of Thermal Expansion
CF-PC – Carbon Fiber Polycarbonate
TTS – Time Temperature Superposition
WLF - Williams–Landel–Ferry
FDM – Fused Deposition Modeling
FFF – Fused Filament Fabrication
SIF – Stress Intensity Factor
SENB – Single Edge Notch Bend
PTFE – Polytetrafluoroethylene
FGM – Functionally Graded Materials
CF-ABS – Carbon Fiber Acrylonitrile Butadiene Styrene
IPM – Inches per Minute
RPM – Rotations per Minute
EDAM – Extrusion Deposition Additive Manufacturing
SVR – Sample Vector Regression
FEA – Finite Element Analysis

List of Figures

List of Tables

List of Appendices

1. EXECUTIVE SUMMARY

Large Scale Extrusion Deposition (LSED) is an evolving additive manufacturing (AM) technology that research, such as that taking place at Oak Ridge National Laboratory (ORNL) and companies like Local Motors, are continuing to utilize and develop new applications. A major LSED application of interest has been molds and tooling as it allows for much shorter production time and lower cost. However, interest has been expanding into using LSED for more structural applications due to more frequent use of high performing polymer composites as feedstock. The use of LSED for structural applications is of particular interest to Local Motors as it is currently being used to create commercially viable, energy efficient electric vehicles. LSED offers a unique opportunity when compared to traditional manufacturing methods as it can significantly reduce the number of components necessary, while decreasing embodied energy and carbon emissions. Even with these benefits however, it is important that LSED is properly understood from a structural aspect as this field has not been as heavily researched as tooling. To ensure a high level of safety and repeatability is an essential responsibility of a manufacturer whose products are structural in nature. As such it is important to understand the materials and LSED process to make structural objects that the manufacturer can be confident in.

The main goals of this project were to: develop and investigate materials that are of interest for structural LSED applications, further develop and understand the current machines used in LSED and develop simulations tools of LSED and the mechanical properties of the created structure. Material development focused on composite materials that have high mechanical properties and are stable in a variety of environments. The materials were tested to determine their as printed mechanical and thermal properties as these are necessary for simulations. Once the materials were investigated thoroughly, it allowed for simulations to be performed to compare to experimental data with simulations. Materials were also vetted to determine candidates for multi-material printing. The machine development focused around the areas of process monitoring, non-destructive evaluation, and quality control. Finally, the goal of the simulations was to develop a realistic model of printed structures, including in-process simulation and dynamic simulation. The routes to get to some of these goals and the depth in which they were investigated changed throughout the project due to personnel changes and the COVID-19 pandemic.

This project resulted in many valuable results such as the development of an nondestructive evaluation (NDE) technique for interlayer defects, proof of simulation for warpage in simple parts, the development and utilization of a profilometer to monitor a print for defects or inconsistencies, thorough investigation of a material used commercially for structural LSED applications and valuable experimental data on the applicability and advantages of multi-material crush structures versus their neat counterparts by creation and testing of samples.

2. INTRODUCTION

Large Scale Extrusion Deposition (LSED) is a technology where pelletized polymer feedstock or pelletized composite feedstock is fed into a large extruder, typically on a gantry system. The feedstock becomes a melt flow through the extruder before exiting the extruder nozzle. The gantry is being controlled by G-code, a type of computer numeric control programming language commonly used in computer-aided manufacturing, that moves the gantry in a given toolpath at a given speed. As the gantry moves in its prescribed motion material is extruded simultaneously thus depositing a layer of material in the XY plane as specified according to the toolpath. The gantry would then move the extruder up a given amount in the Z-direction and this process would be repeated until the final object had been produced. This technology had mainly been of interest commercially for tooling and mainly utilized lower performance polymers such as ABS, Now, more companies are finding uses for it as a process for creating products where structural

integrity is critical, examples of such would be Local Motor's Olli, an autonomous additively manufactured electric shuttle [1]. When creating objects where structural integrity is key it is necessary to have a well understood material and associated process. This project aimed to increase understanding and development of the LSED process and materials used in the LSED process.

This project sought to determine the feasibility for using LSED in structural applications where safety and consistency is paramount to the product. LSED has little literature on its use for large scale production of a product as it is currently used in industry mostly for tooling where it is commonly used in a one-off tooling for prototyping or being researched internally by companies. Thus, for LSED to be more widely adopted in industry it is important to understand the consistency of the process, possible defects that can occur during the process, how to monitor the process for defects, the materials best suited used for LSED, how to evaluate parts in a nondestructive fashion and how to accurately predict the behavior of objects in-process and during use via simulation. Increasing our understanding and developing technology in these spaces is key as quality control and a thoroughly understood manufacturing process and materials is vital, especially in structural components. As the objectives mentioned above were achieved, these accomplishments will allow manufacturers to enter the LSED field more easily. LSED could be used for a variety of industries and products and is currently being used commercially by Local Motors to produce Olli, an autonomous electric shuttle. Due to the ease of design change compared to traditional manufacturing techniques it allows for more fluid revisions and agile responses to design issues. LSED also offers energy savings compared to traditional manufacturing methods with a decrease in embodied energy and reduction in carbon emissions. LSED may soon build fully recyclable products, that can be reused as feedstock. This work focused on achieving the objectives by pursuing three main tasks: material development for LSED, machine development for LSED and develop and verify simulations of the LSED process and mechanical performance of structures.

3. BACKGROUND

LSED has become utilized by more companies and has become the focal points for more researchers. These researchers have been focused on advancing fundamentals of the process, designing for the LSED process, and developing simulation techniques and in-situ monitoring of the process. LSED is a combination of a few technologies that are well researched and understood, with a few added intricacies. These technologies are in essence an extruder, thermoplastic composites, and a CNC control. Intricacies introduced to these technologies are created by the unique layered construction of objects, flow dynamics out of the nozzle and heterogeneous hierarchical thermomechanical properties of a printed part. These intricacies are all deeply connected as the flow from the nozzle orients the reinforcement in the melt flow which contributes significantly to the thermomechanical behavior of the part at a given location, this introduction of heat cyclically in each layer will cause warpage and this warpage is controlled by the thermomechanical properties of the part. The intertwined nature of these intricacies makes it important to understand each of them individually as well as collectively to be able to start understanding the process as a whole. Research groups have been focused on better understanding these intricacies, how to model their behavior and improvement of the process.

For the melt flow observed in LSED, researchers from Texas AM and Baylor have been a leading force. The researchers focus diligently on prior work in the polymer extrusion field, beyond extrusion in additive. Polymer extrusion is not novel, there is much that can be learned from previous works in the field and this knowledge can be built up on to fulfill the current needs in the LSED process. Heller et al. [2]focused on an uncoupled approach to fiber reinforced melt flow, the fibers do not affect the flow of the polymer, deposited on a moving bed to capture the effect on fiber orientation. The extrudate turning upon deposition is what sets this work apart from previous works on fiber reinforced melt flow in additive manufacturing [2]. As the extrudate leaves the nozzle the fibers will change orientation based on deposition height.

However, it should be noted that this work did not take into account printing accessories', such as tampers or rollers', effect on fiber orientation. The results from the simulation combined with some composite mechanics gave material properties of the extrudate that were very comparable to the experimental findings of Duty et.al [3]. Heller's work in this paper shows considerable progress towards being able to accurately model fiber orientation profiles and mechanical properties for LSED processes, which is critical for other modeling and simulation efforts. The criticality of this is especially true when considering fiber orientation measurements in a reinforced polymer are an expensive and time-consuming effort to pursue. Understanding the material properties of parts created using the LSED process is vital to simulation efforts.

Part warpage and residual stresses are intrinsic to parts created using the LSED process. This is due to the deposition of molten material, that has yet to contract, bonding to cooled material, that has already contracted to some extent. As the molten material cools it wants to shrink, however the interlayer bonds have already been formed in the location where the extrudate was originally deposited causing stress to accumulate as the part is built. Simulating this printing process to understand the residual stresses and warpage of the part are necessary for having extremely accurate models of structures and parts created using the LSED process. A research group from Purdue, one of the groups participating in this project, is a leader in the simulation effort for the LSED process. A recent report from the group for an IACMI project, which this project built upon, describes the ADDITIVE3D© process and the results from using it to model the printing process [4]. The ADDITIVE3D© process uses the geometry of the part and the machine code to make the part. Elements are activated as if it was being printed, also emulating thermal input into the system which is used as an input for heat transfer, crystallization, and mechanical analysis. This technique proved to have good correlation for most of the test cases. Showing that this multi-level simulation approach is valid gives hope for adoption in industrial settings [5].

As LSED becomes more popular it becomes important to understand the repeatability of the process. Even before reaching a commercial or industrial setting, researchers need to understand the repeatability of the process so these uncertainties can be factored into research results to provide a more thorough understanding of the research topic. Researchers at Oak Ridge National Laboratory have done some work on understanding quality control and defect identification on LSED parts. One paper introduces a concept to relieve some detrimental artifacts that can present themselves in the LSED process, particularly those seen on BAAM machines from Cincinnati Industries. Chesser et al. [6] introduces the use of a flow diverter to improve control of print seam location and bead thickness when printing corners. These are issues that can not only make parts harder to repeat but can also decrease structural performance of a part if the print seam is not located where it was designed to be located at or if material is thinner than expected in a corner. Borish et al. [7] focused on defect identification and mitigation in the LSED process, again focusing on BAAM machines from Cincinnati Industries. This defect identification was accomplished by relying on a laser profilometer to scan the part and compare it to an ideal version created in the slicing software. The data collected from the part was then compared to the ideal version to allow for correction to the layer height. A technique that if developed could decrease part to part variation, by increasing conformance to the ideal model created by the slicer. ORNL has also focused on other improvements to the LSED process.

One feature that small scale extrusion deposition has when compared to LSED is the ability for some machines to utilize multiple materials within a singular print. The ability to create multi-material prints comes with a range of benefits such as, use of support material and create functionally graded structure. Both of these would open a world of possibilities for the LSED process as overhangs could be printed just like in a small-scale printer using a soluble material for removal and structural optimization while minimizing weight. There are currently no commercial solutions for multi-material LSED, but ORNL has been researching a solution. This solution is centered around a BAAM with two material hoppers that can be switched between in software. Material feeds are naturally positioned at the top of the extruder and as such the material change is not instantaneous, resulting in a continuous transition rather than a stepwise transition. Continuous transition from one material to another requires a foundational work to understand

transition process. Only once the transition process is understood can the multi-material system be utilized fully. Brackett et al. investigates the transition behavior between two common LSED feedstocks, a carbon fiber reinforced acrylonitrile butadiene styrene (ABS) and neat ABS [8]. Results of this study indicate a complex transition behavior that is not symmetric, as the transition from carbon fiber ABS to neat ABS is different from the transition from neat ABS to carbon fiber ABS. Indicating that it is likely that any combination of polymers would have to have a similar investigation to make the most functional use of a material combination in a part. Aside from multi-material capabilities in the LSED process, there is also research occurring in new LSED machines based on robot arms that would increase the degrees of freedom of the LSED process enabling new design possibilities, especially in multirobot scenarios as they could easily utilize different materials [9], [10]. LSED is an evolving technology with many of the leaders in LSED research and commercialization being involved in this project.

4. RESULTS AND DISCUSSION

Material Property Testing

Milestone 3.12.2.3 Mechanical testing has been completed

When going through the engineering design process a material suitable for the requirements must be chosen. To choose the correct material it is important to have knowledge of the material properties of each of the candidates. Using the properties one can ensure that a chosen material will meet the design criteria for a given part. As LSED is a recently developed technology there is a need to characterize these materials before they can be used for structures, especially those critical to safety. Figure 1 displays the coordinate system used at the bead level, which is referenced several times in this report. Material properties considered critical to design were chosen, a table of which can be seen below in Table 1**,** these material properties were then tested according to an ASTM standard for the candidate material. The project was originally supposed to test multiple candidate materials printed on an LSAM, however due to time and cost constraints multiple candidate materials were not tested. The material these tests were run on was polycarbonate reinforced with 20% carbon fiber (CF-PC) by weight printed on a Thermwood Large Scale Additive Manufacturing (LSAM) printer. Results will be discussed in the order shown in Table 1.

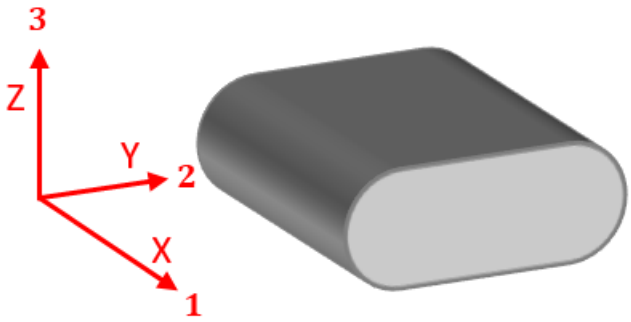

Figure 1 – Bead level coordinate system

Table 1- Material properties to be tested for candidate material

Property / Material Descriptor	Characterization Method	Relevant Standard	Characterization Level
Glass Transition Temperature	Dynamic Mechanical Analysis (DMA)	ASTM D7028	bulk
Glass Transition Temperature	Differential Scanning Calorimetry (DSC)	ASTM D3418	bulk
Void content	Optical Microscopy		bulk
Elastic modulus - E1, Poisson's ratio - v13, Tensile strength - X1	Tensile testing and Digital Image Correlation	ASTM D3039	bead
Elastic modulus - E3, Poisson's ratio - v13, Tensile strength - X3	Tensile test and Digital Image Correlation	ASTM D3039	bead
Shear moduli - G13, G31, Shear Strength X13, X31	V-Notched beam method and Digital Image Correlation	ASTM D5379	bead
Coefficient of thermal expansion as a function of temperature - α1 (T), α2 (T), α3 (T)	Thermomechanical analysis (TMA)	ASTM E831	bead
Relaxation curves for E1(t,T), E2(t,T), E3(t,T) at multiple temperatures	Stress relaxation experiments - DMA equipped with 3-point bending fixture		bead
Thermal conductivity as a function of temperature - K1(T), K2(T), K3(T)	Flash method	ASTM E1461 &	bead
Heat capacity as a function of temperature - Cp(T)	Differential Scanning Calorimetry (DSC)	ASTM E1269	bulk
Stress Intensity Factor	Single Edge Notch Bend	ASTM D5045-15	bulk

Glass Transition Temperature

Glass transition temperature was measured in two different ways, dynamic mechanical analysis (DMA) and differential scanning calorimetry (DSC). DSC was performed on a TA Instruments Q-2000 DSC at The University of Tennessee's Polymer Characterization Lab. The sample was a section of a pellet of the candidate material and a non-hermetic aluminum pan was used as the container for the sample. Candidate material was dried for 24 hours at 82°C. This ensured that there was no moisture in the material that could alter the test results. The material was tested between room temperature and 300°C at a ramp rate of 10°C per minute. A graph of the results can be seen in Figure 2 below. The results show the glass transition temperature to be at 153°C.

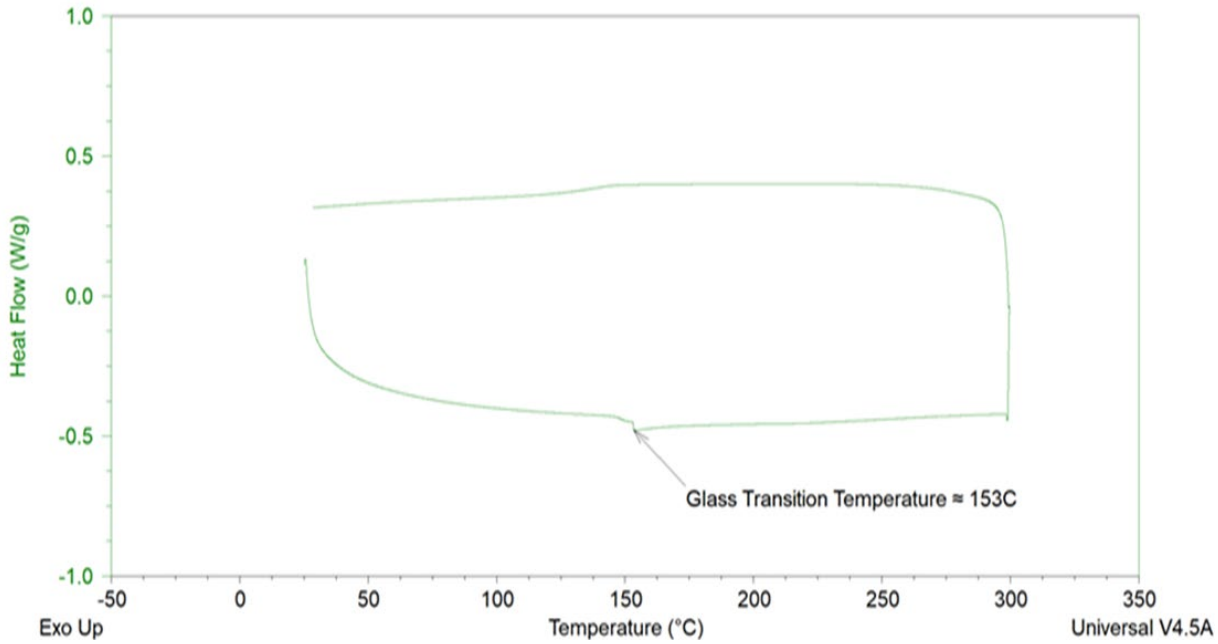

Figure 2 - Graph of CF-PC DSC results

Torsional DMA was conducted on a TA Instruments DHR-2, a forced resonance analyzer. Samples were sectioned from a printed plank using an Isomet 1000 precision saw, the sample dimensions were 55mm x 13mm x 4mm. As this is not a directionally dependent property the sample orientation with respect to printing will not be discussed. Samples were dried at 82°C. Parameters for the DMA testing were a ramp rate of 2.5°C per minute, 0.05% strain, frequency of 1Hz. There are three ways to classify glass transition temperature using DMA: peak of loss modulus, onset of decline in storage modulus and peak of tan(delta). The results of the DMA can be seen in Figure 3 below. The data shows the three classifications for glass transition temperature as 146°C for peak of loss modulus, 145°C for onset of decline in storage modulus and 150°C for peak of tan(delta). These results are comparable to that of the DSC testing, allowing a glass transition temperature of 150°C to be used with a high level of confidence in accuracy.

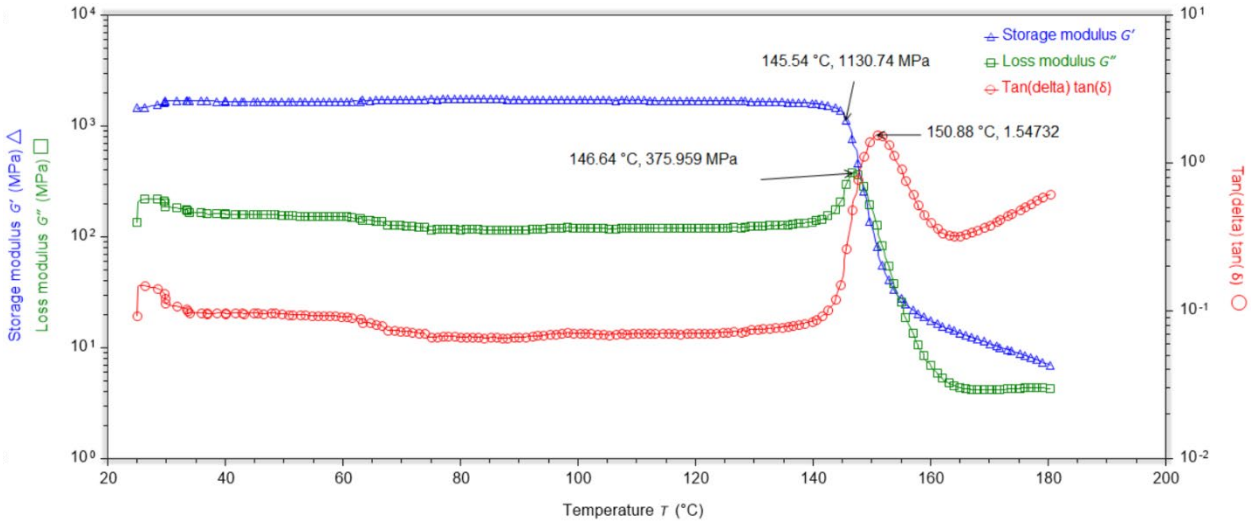

Figure 3 - Graph of results from CF-PC DMA testing

Porosity

Porosity characterization through optical microscopy was used to measure void content. Four sets of 20% carbon fiber polycarbonate single bead walls were sectioned from a printed plank using an Isomet 1000 precision saw, polished, and then imaged with an optical microscope. An example of the as printed specimens can be seen in Figure 4 below. The composite images were then processed through image analysis to measure the internal porosity within each bead. Each set (A-D) was printed under altered conditions as described in Table 2, nominal conditions being 500 in/min, 0.2" x 0.5" bead with a 0.5" nozzle and 2 minute 20 second layer time. Bead area was reduced by 0.009 in^2 in all calculations for bead to nozzle area ratio values to account for bead not being perfectly rectangular. Samples were taken from a single bead wide printed wall; each sample is identified by a letter and number. This letter and number trace the printing parameters used in that particular sample. The samples received had already been sectioned once and had varying numbers of layers dependent on these printing parameters, with the minimum number of layers being 4 and the maximum number of layers being 9. In some of these samples the outermost beads were only partial beads having been cut down the middle of those beads during the prior sectioning. For example, sample wall A1 was printed with a layer time of 2:20 and contained 6 total beads (as seen in Appendix A).

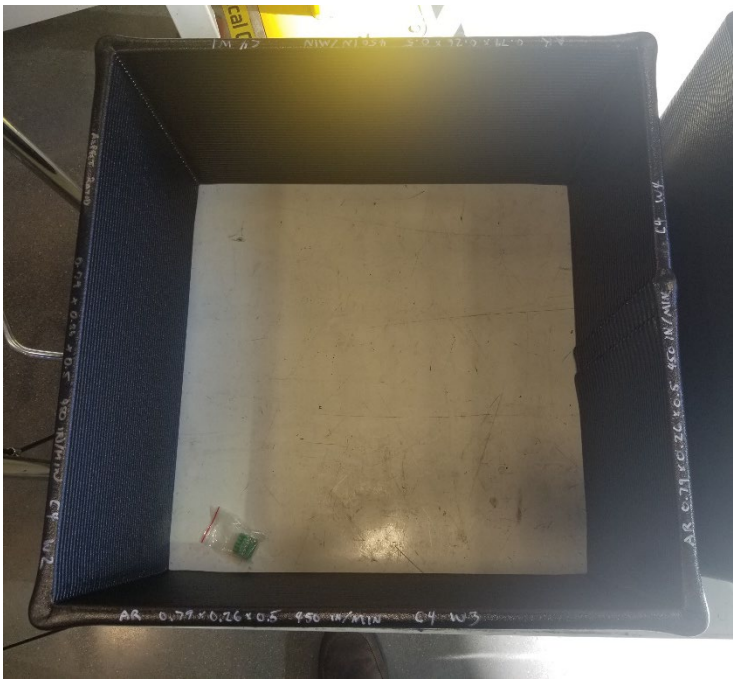

Figure 4 Image of as printed process variability sample

Table 2 - Process Variables for Each Sample Wall of CF-PC

	A	B	C	D
Sample ID #	**Layer Time (mins)**	**Print Speed (in/min)**	**Bead Aspect Ratio & Bead-to-Nozzle-Area Ratio**	**Nozzle Sizes (in diam)**
1	2:20	100	3, 0.77	0.3
2	3:20	300	4, 0.77	0.4
3	4:20	500	5, 0.77	-
4	6:00	-	3, 0.97	-
5	-	-	4, 0.97	-
6	-	-	5, 0.97	-

It was assumed for the purpose of this analysis that each bead was within the steady state region of the print, though some trends in the data may indicate otherwise. A half-inch thick slice of each wall was cut with a precision diamond saw at low rpms to avoid damaging or shattering the internal fibers. These slices were then mounted in epoxy resin and polished at progressively finer grits ranging from 180-4000. A final polish was performed with a silica slurry ranging from 5-0.5 microns. Sets D and C were only polished to 5 microns after it was determined this would not noticeably alter the image analysis.

A Zeiss Axio Imager was used to image each sample at 60x. The primary goal of the imaging process was to achieve the highest contrast between the porosities and other surface features to allow for the easiest and most reliable image analysis. After imaging all of sets A and B one major problem was encountered. All the samples had suffered some degree of surface scratching during the polishing procedure. A single bead of sample A1 was imaged at 250x in addition to examine the surfaces of the internal fibers as it was

suspected the damage came from fibers falling out of the polymer matrix and being dragged across the surface during the polishing. Figure 5 shows a close-up of a few fibers within sample A1. Note that the fibers are completely shattered and that there is polymer between the fiber fragments indicating this damage occurred during the extrusion process while the polymer was still molten, and not during the sample preparation itself.

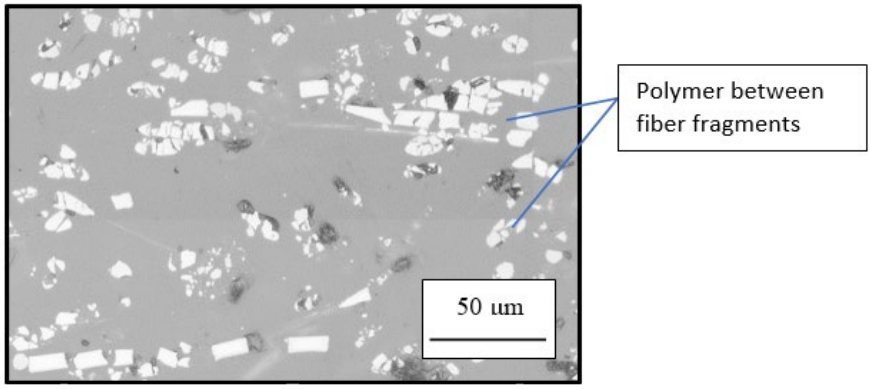

Figure 5 - Fiber Breakage within Sample A1

Image analysis was performed using ImageJ Fiji. Step one was selecting the area of each bead to be analyzed. The area between each bead was avoided as the purpose of this analysis was not to focus on the lack of fusion porosities between layers, and instead look at the porosities within the beads themselves. Furthermore, areas of poor contrast due to imaging error or large polishing defects were avoided. Note that even after the total repolish of all samples, some scratching still persisted leading to a slight overestimation of the internal porosity. Each individual bead was saved as a separate 8-bit black and white image including the partial beads on each end of the wall. A value of 1 was subtracted from every pixel leaving the 255-pixel value "blank." A threshold was performed on a copy of the image to reduce the entire image into minimum and maximum value pixels. Because of the high contrast achieved during microscopy, this separated the dark regions (pores, scratches, and fiber pullout) from all other features (fibers and background matrix).

The "analyze particle" tool was used to fill in the holes within pores that hadn't been fully selected. It also removed all particles below a manually set minimum total pixel count. This was set to remove "pores" small enough to be indistinguishable from the holes left behind by fibers that had fallen out of the matrix. It also had the benefit of removing "salt and pepper" imaging defects. The new image was overlayed on top of the previously saved image inserting the porosity data into the single blank pixel value (255). At this point the porosity could be easily viewed in relation to the almost unaltered background image and easily retrieved as it is the only pixels within the image at that specific value. The total porosity is calculated by the ratio of pixels at value 255 to the total number of pixels in the selection of interest. Figure 6 shows the compound image for sample A1 bead 5.

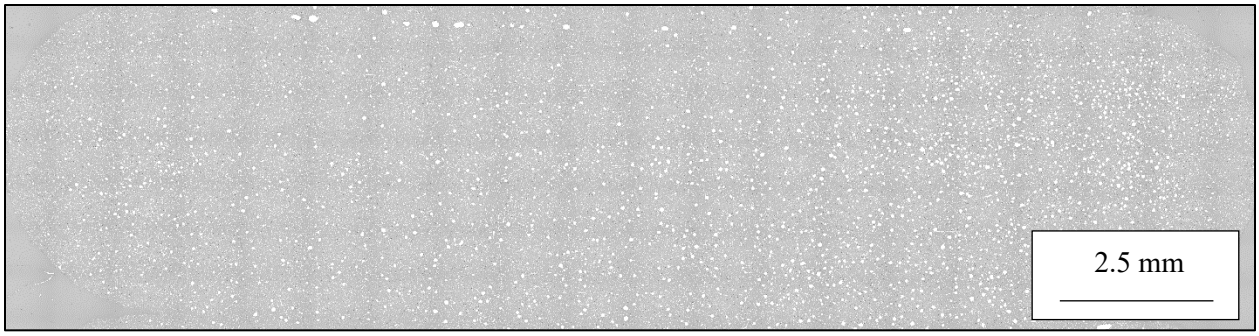

Figure 6 – Sample A1, Bead 5, 6.8% Porosity

While all the raw porosity data may be found in Appendix A, Figures 7 and 8 show the collected porosity data across all sample sets. The average porosity across all samples was found to be 8.3% (with a standard deviation of 2.3%), which is much higher than anticipated. Varying the print conditions was able to reduce the porosity to a minimum of 4.5%, but poor print conditions could produce porosity as high as 13.5%. Within set A the porosity had high variance and did not seem to be correlated to the increase in layer time. Set B shows a drop in average porosity from 7.5% to 5.6% (a 25% decrease) between the initial print speed of 100 in/min and the second two speeds of 300 and 500 in/min, but there is no significant difference between those second two speeds. For set C, the first detail to note is that sample C4 had the lowest average porosity of any sample tested (4.7%) and the lowest standard deviation of any sample (0.3). However, it also had the fewest beads to analyze (2 complete and the half bead on each end). The total surface area of the beads in C4 was similar to others, but the individual beads were much larger. Looking at the rest of set C shows that porosity seems to be mostly affected by the beat-to-nozzle-area ratio with an increase in porosity from 8.4% to 11.7% (a 39% increase) as the ratio shifted from 0.77 to 0.97. Sample C4 is an exception to this rule and may simply be an outlier. The second modification within set C was the bead aspect ratio, which did not show a strong correlation to porosity within this set of print conditions. Set D also shows inconclusive results for whether the nozzle size itself plays a role in porosity formation. While the average porosity differs by a percent between D1 and D2, there is such high variance and the presence of a strong outlier in each that further research would be required to make any more specific claims.

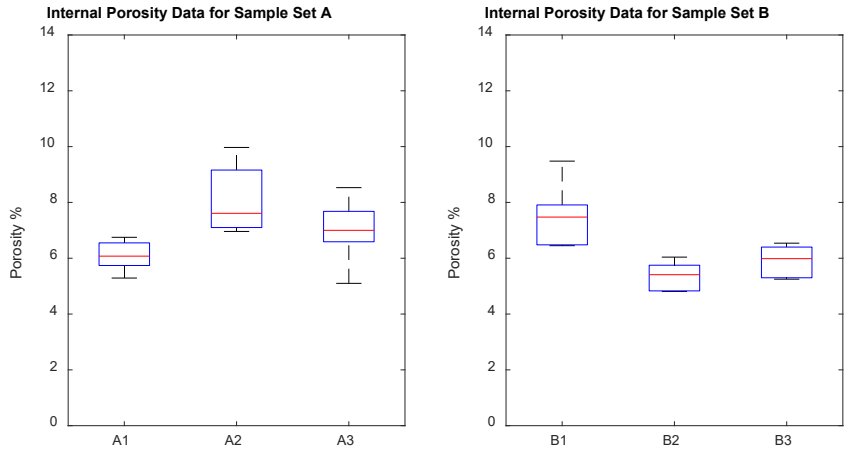

Figure 7 – left: Porosity Data for Sample Set A, right: Porosity Data for Sample Set B

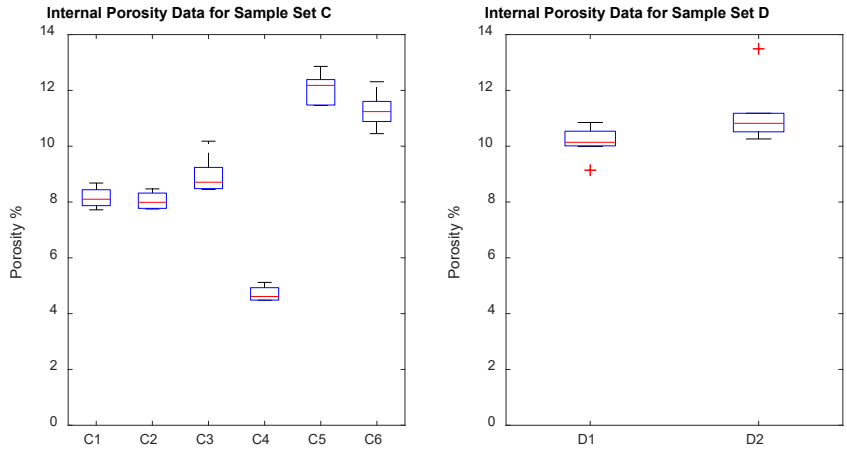

Figure 8 – left: Porosity Data for Sample Set C, right: Porosity Data for Sample Set D

One final trend to point out in the raw data is that across every sample set, the half-beads were typically outliers with measured porosities about 1% higher than any of the complete beads. Without knowing the print order or whether those partial beads were transitional beads between each sample set, the cause of this discrepancy in observed porosity is unknown. A potential answer lies in the fact that the porosities within each bead were highly regionalized as can be seen in the compound image (Figure 6) shown in the microscopy section. In that image, the top left half of the bead has visibly far less porosity than the bottom right. This would allow the partial beads to show a statistically different internal porosity than the average of the complete beads. However, this would make more sense if the partial beads were overestimates about half the time and underestimates the other half.

Tensile Strength and Elastic Modulus

Like void content, there are several parameters in LSED that may impact tensile strength and stiffness. A parameter study was performed using the same process variability study described in the void content section, Table 1. This process variability study on tensile strength ties in directly with Milestone 3.12.2 and 3.12.3 as understanding the effect of the process variables are key to set a target range for creating the highest quality part. Tensile samples were created from the process variability prints. Specimens were created following a modified ASTM D638 Type III specimen, the modification being the sample dimensions were scaled up by a factor of 2. Specimens were tested on an Instron Model 1332 with a 250kN load cell. Samples were strained at a rate of 0.1 mm per minute. Digital image correlation (DIC) was conducted on some samples to determine the Poisson's ratio. Investigation was not done on material properties in the Y-direction due to difficulties creating and testing of LSAM Y-direction samples.

The parameter known to have the largest effect on Z-direction tensile strength, layer time. Longer layer times lead to decreased strength, as can be seen in Figure 9 below. A decrease in elastic modulus was not seen as layer time increased though. The decrease in Z-direction strength is due to the temperature of the previous layer being lower as more time passes, a decrease that is not observed in Z-direction modulus. A drop in tensile strength by 57% between the shortest and longest tested layer times. Lower temperature of the previous layer means that the new layer will not be able to bond to it as well. This decreased strength because of longer layer times shows the necessity of controlling layer time to be the minimum possible, without causing bead collapse due to printing on still molten material. Leading to not only stronger parts being printed, but also lower printer utilization per part, which is important in a manufacturing scenario. Experiments on layer times effect on X-direction properties revealed layer time does not affect X-direction strength or stiffness.

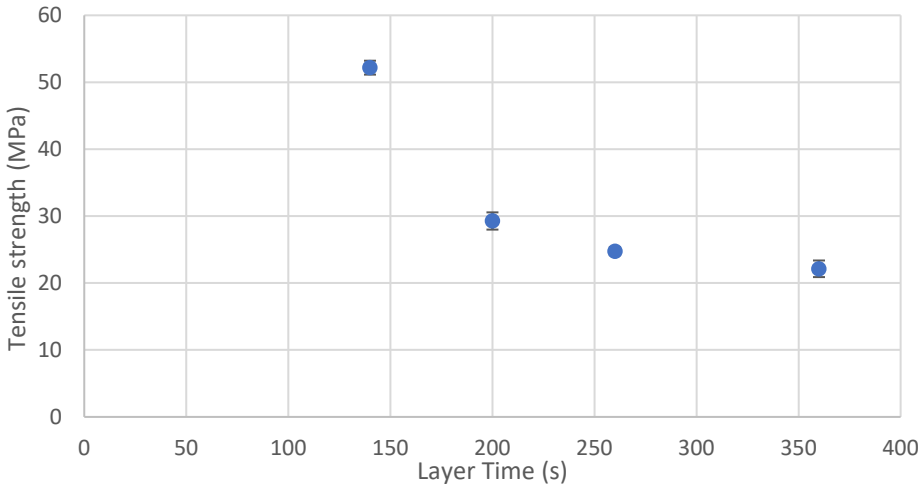

Figure 9 - Graph of effect of layer time on CF-PC Z direction tensile strength

Print speed directly affects the flowrate of the material, which changes the velocity and shear profile of the melt in the extrusion process. The change in shear profiles can impact fiber alignment of the extrudate, this fiber alignment playing a large part in material properties of the composite. As such it is an important parameter to understand the effects of, especially for design optimization. The results for print speed effect on elastic modulus can be seen in Figure 10 below. There is a slight increase in both X- and Z-direction modulus as printing speed increases. Figure 11 shows the effect of print speed on tensile strength. Increasing print speed seems to increase X-direction strength slightly and decreases Z-direction strength slightly. It is likely that the roller on the LSAM decreases the effect of printing speed on material properties, as the roller will compact and cause flow of material after the extrudate leaves the nozzle. A system that has no similar roller system may see a larger impact of material performance based on print speed.

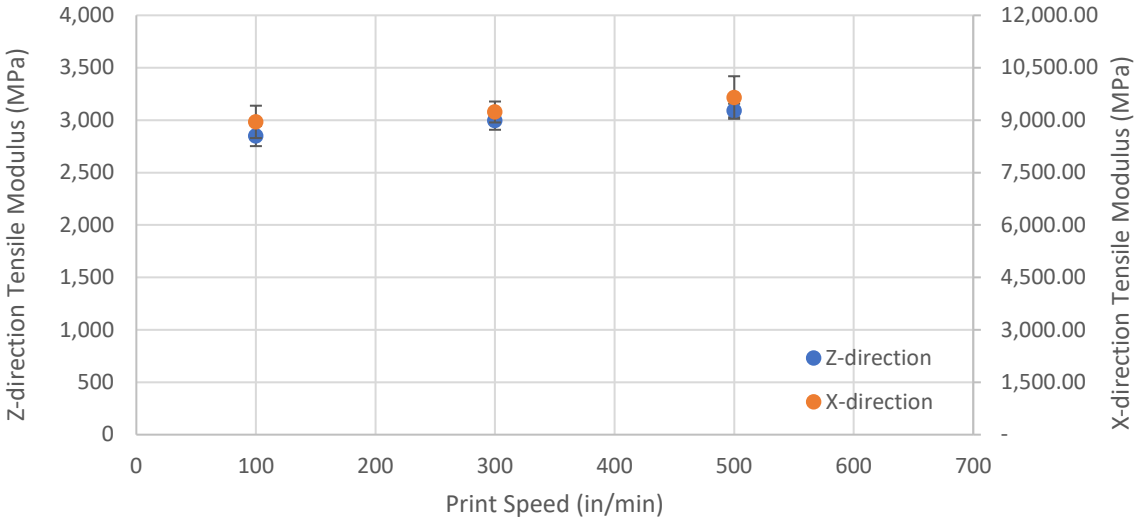

Figure 10 - Graph showing effect of print speed on CF-PC elastic modulus in the X- and Z- directions

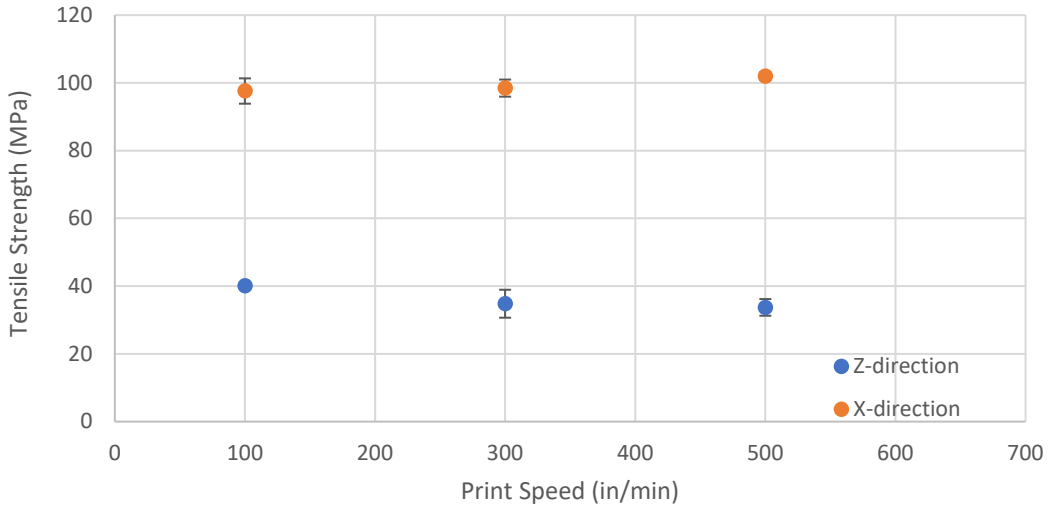

Figure 11 - Graph showing effect of print speed on CF-PC tensile strength in the X- and Z-directions

Aspect ratio is an also an important parameter in making a quality part. If a bead is too tall, it is likely that the bead will collapse on itself during the process. Bead collapse would create a poor-quality part and possibly cause a print to fail if several layers are collapsing. It will also affect the fiber orientation in the extrudate, on the LSAM or a system with no roller, as the flow during the turn after extrusion and the flow during the rolling process will be affected by aspect ratio of the bead. Figure 12 below expresses the relationship between aspect ratio, bead-to-nozzle area ratio and X-direction modulus. Increasing aspect ratio decreases modulus for both bead-to-nozzle area ratios. A decrease that is likely caused by more material flow from the rolling process in the width of the bead causing lower fiber alignment in X-direction. Based on these samples, higher bead-to-nozzle ratio seems to be more affected by changes in aspect ratio, but also offers potential higher X-modulus at lower aspect ratio than lower bead-to-nozzle ratios. Z-direction modulus appears to follow a similar trend, results of which can be seen in Figure 13. It does appear that Z-direction modulus is less affected by aspect ratio than the X-direction modulus. X-direction modulus seeing a decrease of 36% on 0.97 bead-to-nozzle ratio and a 16% decrease in the 0.77 bead-to-nozzle ratio compared to a 33% decrease in 0.97 bead-to-nozzle ratio and 3% decrease in 0.77 bead-to nozzle ratio in the Z-direction.

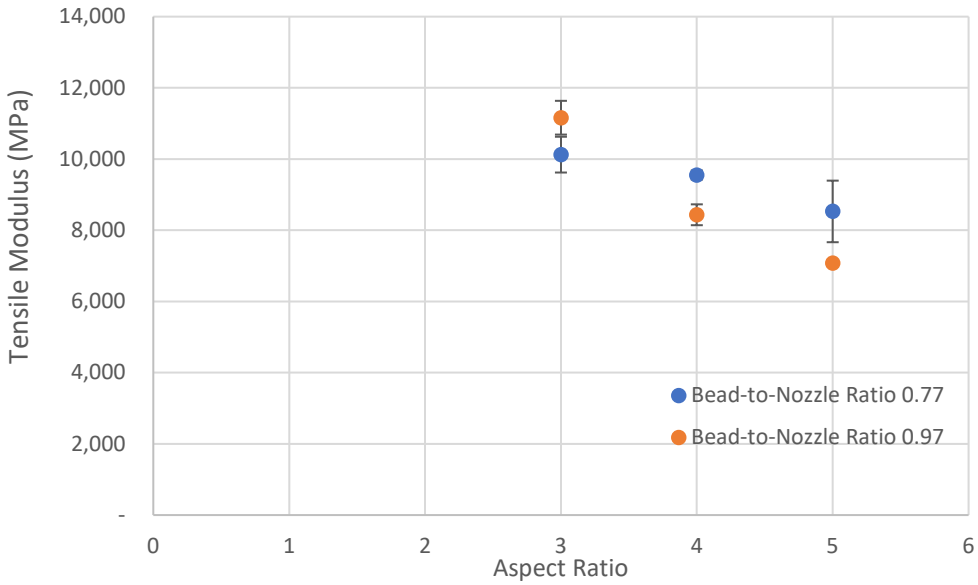

Figure 12 - Graph of aspect ratio impact on CF-PC X-direction tensile modulus

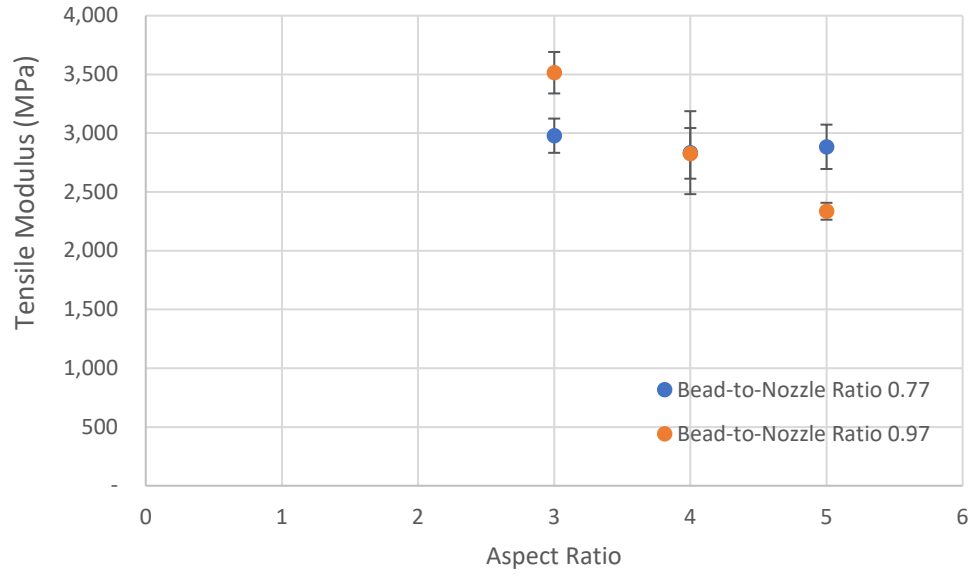

Figure 13 - Graph of aspect ratio impact on CF-PC Z-direction tensile modulus

The effect of aspect ratio on tensile strength is also related to fiber alignment in the bead. The direction with more aligned fibers will see an increase in strength. Figures 14 and 15 shows that 0.97 bead-to-nozzle displays a slight negative trend in both X-direction and Z-direction tensile strength, but there is no discernable relationship revealed in the 0.77 bead-to-nozzle ratio. A possible explanation for this would be more flow from the rolling process in the width of the bead to reach higher aspect ratios causing lower alignment in the X-direction and Z-directions.

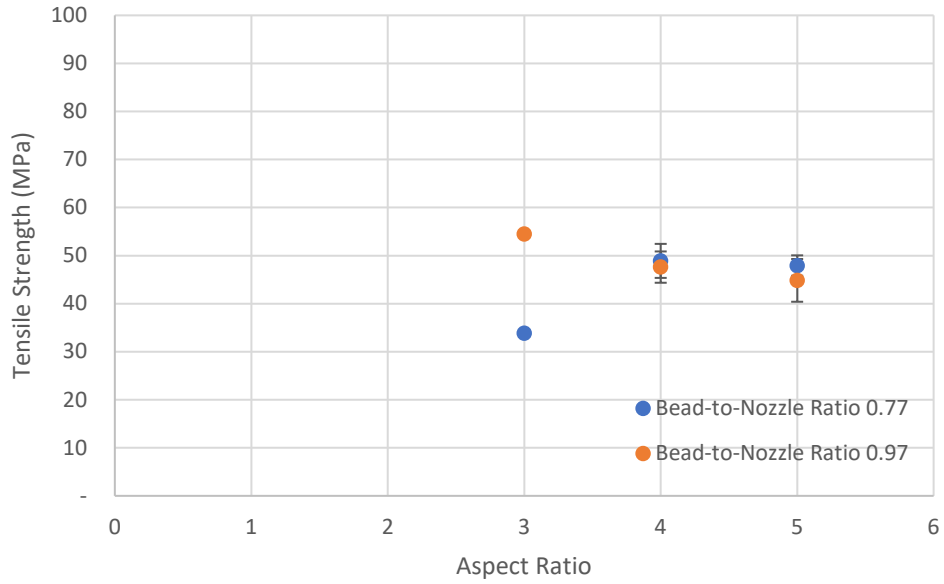

Figure 14 – Graph of aspect ratio impact on CF-PC X-direction Tensile Strength

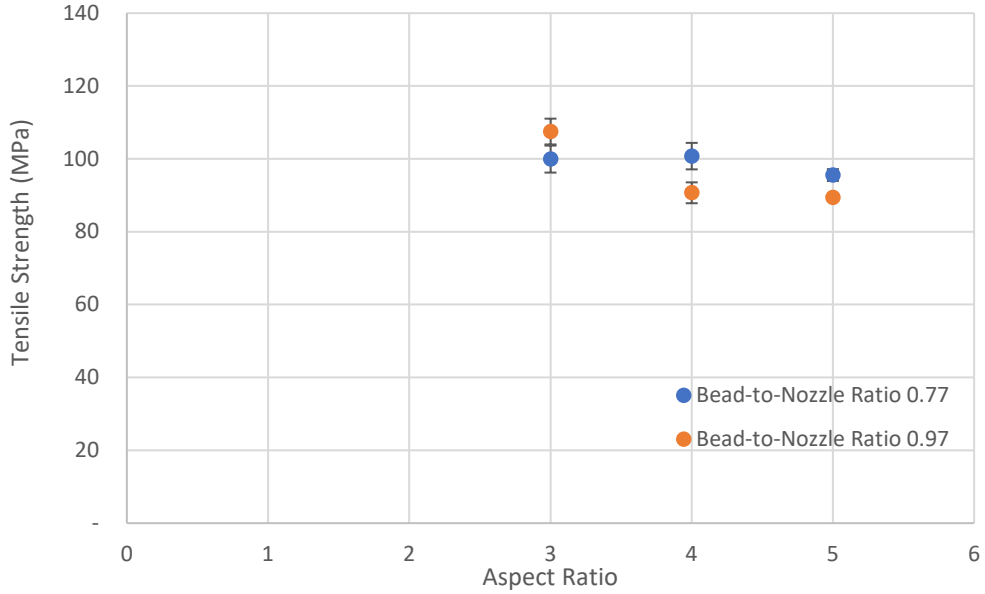

Figure 15 - Graph of aspect ratio impact on CF-PC Z-direction tensile strength

The final process variable that was assessed was the effect of nozzle size. Nozzle size will affect the amount of shear the material experiences as it comes out of the nozzle to be deposited. This shear will affect the fiber alignment in the extrudate, causing smaller nozzle sizes to have higher fiber alignment in the print direction. Changing nozzle size did not seem to have an effect on X- or Z-direction elastic modulus. However, it did affect X- and Z-direction tensile strength as seen in Figure 16 below. Increasing nozzle size decreased tensile strength in both directions. Increase in the X-direction is easy to explain due to fiber alignment effect discussed earlier, however the decrease in the Z-direction is not as clear. Z-direction decrease could be due to flow restriction changing the

polymer chains at the surface or an increase in the resin at the surface.

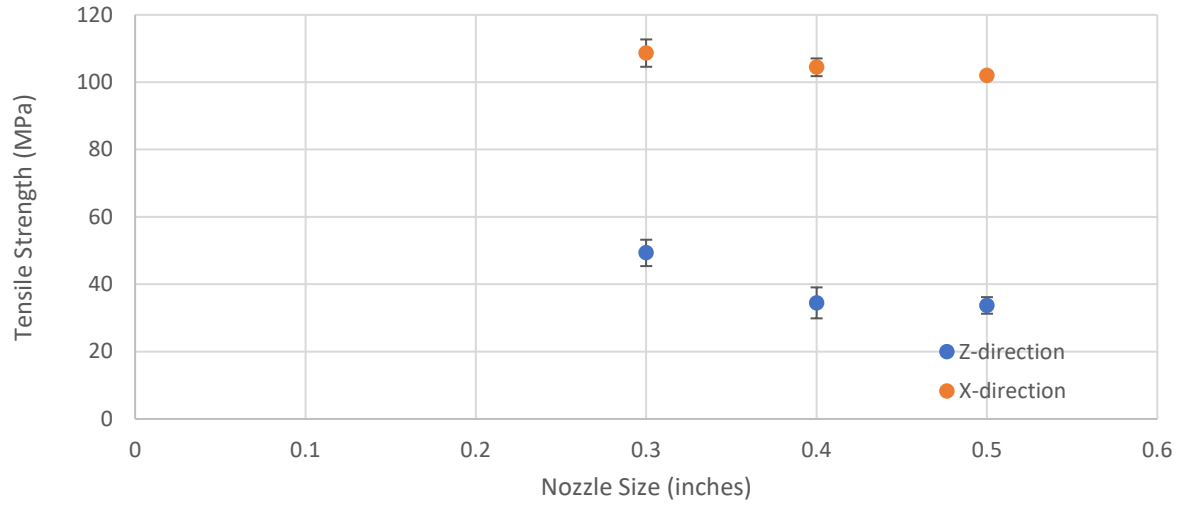

Figure 16 - Graph of nozzle size impact on CF-PC tensile strength

Poisson's Ratio

Poisson's ratio was measured using DIC of samples in tension. Poisson's ratio was not measured for all the process variables. Just on the nominal print conditions mentioned earlier. Poisson's ratio was measured on two samples and the average of the samples was taken as the representative value of the material. Poisson's ratio was calculated by plotting axial strain vs. transverse strain and fitting a line to the results, the slope of the line is the Poisson's ratio. Poisson's ratio was dependent loading direction and observed transverse direction. Results have shown that Poisson's ratio is highly variable within a printed part. These values were necessary for use in simulation as it represents how the material strains in the transverse direction when put under axial strain. Behavior of the material ranged from comparable to polycarbonate to comparable to carbon fiber depending on loading direction and transverse direction measured. The results can be seen below in Table 3.

Table 3 - Table of Poisson's ratio values for CF-PC at nominal conditions

Sample Orientation	Sample 1	Sample 2	Average
ν_{XY}	0.2669	0.2451	0.256
ν_{XZ}	0.35*	0.3653	0.35765
ν_{ZY}	0.2987	0.3016	0.30015
ν_{ZX}	0.11*	0.1407	0.12535

Shear Modulus and Strength

Shear modulus and shear strength was measured in the XZ direction and ZX direction. Test methodology is reflective of the ASTM D 7078-05 standard for v-notch rail shear, but with a slight modification. The test fixture is designed to accommodate specimen twice the dimensions for wide v-notched specimen, seen in Figure 17, of the ASTM standard. The ZX and XZ orientations are shown below with the arrows indicating how shear is induced by displacement.

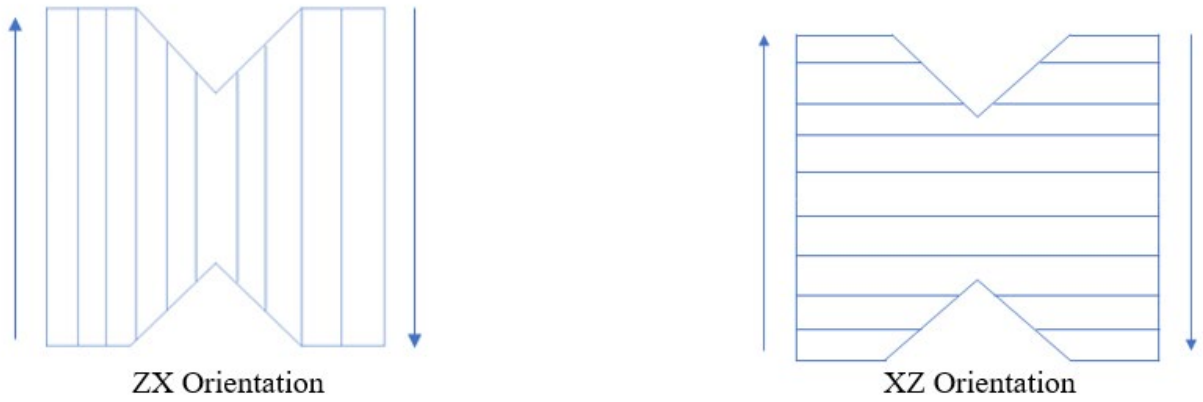

Figure 17 - Images of bead orientation in shear samples

Each sample was created from single bead width wall printed at the nominal print conditions mentioned earlier. The wall was planed flat to get rid of exterior bead geometry and then cut on a waterjet to get the correct sample geometry. Samples were then speckled and placed in the customized shear fixture to load until shear failure. Samples were gripped via twelve bolts tightened to 100 foot-pounds using a torque wrench. A strain rate of 0.0008 in/s was used with the Instron. Proper camera and lighting equipment were set up to operate with GOM Correlate, an open source 2-D DIC software. Data was analyzed by correlating strain measurements taken from DIC and load cell values from the Instron frame. Stress-strain plots were generated in MATLAB to determine slope for shear modulus. Ultimate strain was calculated by matching strain at shear failure using DIC. Results can be seen in Table 4 below. Shear modulus and strength between the two orientations are basically indistinguishable considering standard deviation.

Table 4 – Mechanical properties from CF-PC v-notch shear testing

CF-PC Mechanical Properties						
Orientation	**Modulus, G [MPa]**	**Standard Deviation (G) [MPa]**	**Ult. Strength, σ_{ult} [MPa]**	**Standard Deviation (σ_{ult}) [MPa]**	**Ult. Strain, ε_{ult} [%]**	**Standard Deviation (ε_{ult}) [%]**
XZ	1960.2	105.5	32.6	1.59	2.43	0.39
ZX	1905.7	146.9	33.8	0.69	2.91	0.20

Coefficient of Thermal Expansion

Coefficient of thermal expansion (CTE) was measured on a TA Instruments Q-400EM TMA, between room temperature and 155 °C at a rate of 5 °C/min. Sample was an entire bead sectioned using an Isomet 1000 precision saw (3 mm x 13 mm x 4 mm). A force of 0.02N was held for the experimentation. CTE was then calculated using TA Instruments Universal Analysis software by fitting a straight line to the dimensional change and temperature data between room temperature and 150°C, which is below glass transition temperature. Results of the experiments were an X-direction CTE of 7.3 µm/(m°C), a Y-direction CTE of 77.8 µm/(m°C) and a Z-direction CTE of 92.3 µm/(m°C) all of which are measured below glass transition temperature of the material.

Density

The density of the printed carbon fiber reinforced polycarbonate (CF-PC) was calculated from the volume and mass of the samples provided to the Thermophysical Laboratory for characterizing thermal conductivity and heat capacity. The average density of the printed material was 1.187 g/cm^3.

Heat Capacity

The heat capacity was characterized as a function of temperature for the printed materials according to the ASTM E1269 [11] standard. The heat capacity is determined by differential scanning calorimetry under an inert atmosphere and with sapphire as the reference material. The reference material and the sample are subjected to the same heat flux and the differential powers required to heat the reference material and sample at the same rate were determined using the digital data acquisition system. Utilizing the mass of the reference material, the differential power, and the known heat capacity of the sapphire, the heat capacity of the sample is computed. Figure 18 shows the heat capacity characterized as a function of temperature for the CF-PC. A discontinuity in the heat capacity occurs at around the glass transition temperature (indicated with vertical dashed lines in Figure 18).

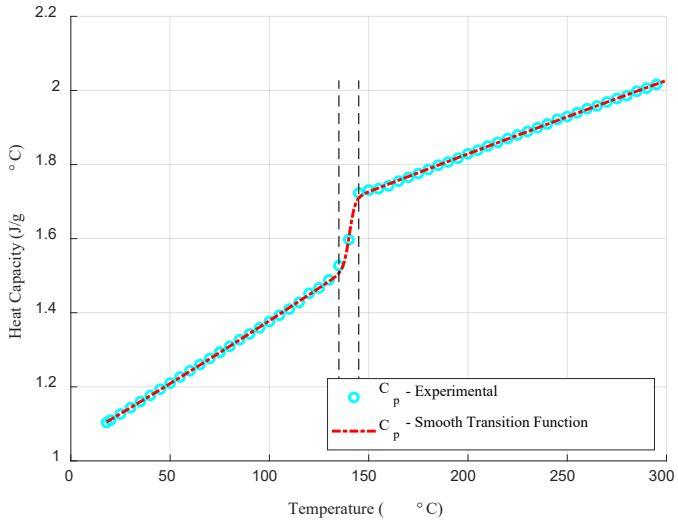

Figure 18 – Heat capacity of CF-PC as a function of temperature.

A piecewise function with a smooth transition introduced with a sigmoid function (red dashed line in Figure 18) was used to describe the evolution of heat capacity with temperature from the room temperature to the processing temperature of 300 °C. The heat capacity is described as a function of temperature as given by

Equation (1). Quadratic functions are used to describe the heat capacity for temperature above ($C_p^{aT_g}$) and below ($C_p^{bT_g}$) the glass transition temperature.

$$C_p(T) = \big(1 - S(T)\big) \cdot C_p^{bT_g}(T) + S(T) \cdot C_p^{aT_g}(T) \quad (1)$$

Table 5 lists the parameters of the quadratic and sigmoid functions that describes the heat capacity of the CF-PC as a function of temperature.

Table 5 - Parameters of piecewise function with a smooth transition used to describe the heat capacity of CF-PC as a function of temperature.

$C_p(T) = p_1T^2 + p_2T + p_3$			
	$p_1\ (J/g°C^3)$	$p_2\ (J/g°C^2)$	$p_3\ (J/g°C)$
$C_p^{bT_g}\ (J/g°C)$	$1.815 \cdot 10^{-6}$	$3.119 \cdot 10^{-3}$	1.048
$C_p^{aT_g}\ (J/g°C)$	$-3.988 \cdot 10^{-7}$	$2.183 \cdot 10^{-3}$	1.408
$S(T) = 1/(1 + e^{(-(T-C_1)/C_2)})$			
C_1		140.367	
C_2		1.417	

Thermal Conductivity

The thermal conductivity was determined from measurements of thermal diffusivity, heat capacity, and density for the three principal material directions. Thermal diffusivity was measured as a function of temperature using the laser flash method according to the ASTM E1461 [12] standard. Thermal conductivity is determined from the product of the thermal diffusivity, the heat capacity, and the density. The density was calculated from the mass and geometry of the samples whereas the heat capacity was measured via DSC. A constant density value was assumed in the calculation of the thermal conductivity. In the laser flash method, the front face of a small disk-shaped sample is subjected to a short laser burst while the resulting temperature rise on the rear face of the sample is recorded and analyzed. The laser flash apparatus employed at Thermophysical Laboratory consists of Korad K2 laser, a high vacuum system including a bell jar with windows for monitoring of the sample, a tantalum or stainless-steel tube heater surrounding a sample holding assembly, a thermocouple or and IR detector, and a data acquisition system with signal conditioners. The specimens provided to Thermophysical Laboratory for characterizing the thermal conductivity were extracted in the three material directions (disks of about 12 mm in diameter) from a block printed in the LSAM system with CF-PC. Figure 19 shows the thermal conductivity as a function of temperature in the three principal material directions of the printed CF-PC.

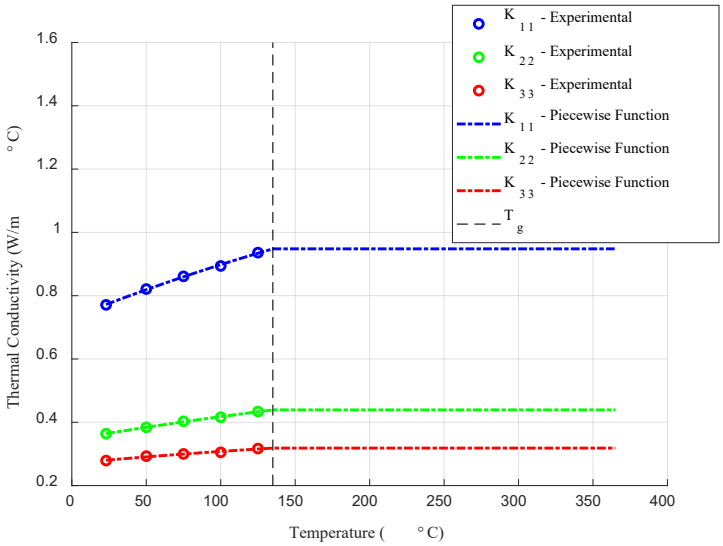

Figure 19 – Thermal conductivity in the three principal directions of printed CF-PC

A piecewise function was used to describe the evolution of the thermal conductivity as a function of temperature in the heat transfer analysis of the process simulations. A quadratic function was used to describe the thermal conductivity from the room temperature to the T_g (145.5 $°C$) whereas a constant value was assumed beyond that temperature. Table 6 lists the parameters of the piecewise functions used to describe the thermal conductivities of CF-PC as a function of temperature.

Table 6 - Parameters of piecewise functions used to describe thermal conductivities of CF-PC as a function of temperature.

$K_{ii}(T) = p_1T^2 + p_2T + p_3$			
$T < T_g$	$p_1\ (W/m°C^3)$	$p_2\ (W/m°C^2)$	$p_3\ (W/m°C)$
$K_{11}\ (W/m°C)$	$-1.864 \cdot 10^{-6}$	$1.864 \cdot 10^{-3}$	$7.303 \cdot 10^{-1}$
$K_{22}\ (W/m°C)$	$-8.033 \cdot 10^{-7}$	$7.964 \cdot 10^{-4}$	$3.463 \cdot 10^{-1}$
$K_{33}\ (W/m°C)$	$-5.460 \cdot 10^{-7}$	$4.279 \cdot 10^{-4}$	$2.706 \cdot 10^{-1}$
$T > T_g$			
$K_{11}\ (W/m°C)$	$9.48 \cdot 10^{-1}$		
$K_{22}\ (W/m°C)$	$4.39 \cdot 10^{-1}$		
$K_{33}\ (W/m°C)$	$3.18 \cdot 10^{-1}$		

Thermoviscoelastic Behavior

Unlike other types of materials, polymers show a pronounced viscoelastic mechanical material behavior. This means that they exhibit both the solid characteristics of elastic materials and store elastic energy when loaded, but also dissipate a part of the energy and flow on the microscale showing a fluid-like behavior. Therefore, time becomes an essential parameter for the material description. A detailed discussion of the reasons for this combined behavior based on the morphology of polymers and related physics is beyond the scope of this report, therefore the reader is referred elsewhere for further details [15].

The printed material undergoes temperature changes from the extrusion temperature to the room temperature; therefore, the temperature influence on the viscoelastic material properties must be

characterized and modeled to get the full thermoviscoelastic material behavior required for additive process simulations. The thermoviscoelastic behavior is characterized by performing stress relaxation experiments at different temperatures in a temperature range from room temperature to about the glass transition temperature of an amorphous polymer such as polycarbonate. Stress relaxation experiments are conducted at different temperatures in a DMA, wherein a strain step is applied, and the resulting stress is recorded as a function of time. Stress relaxation experiments were carried out with samples of CF-PC in a DMA model Q800 from TA Instruments© and in a temperature range from $30\ °C$ to $200\ °C$. Figure 20 shows the stress relaxation experiments carried out in the 1-direction and in the 3-direction for sample of CF-PC printed in the LSAM system.

A)

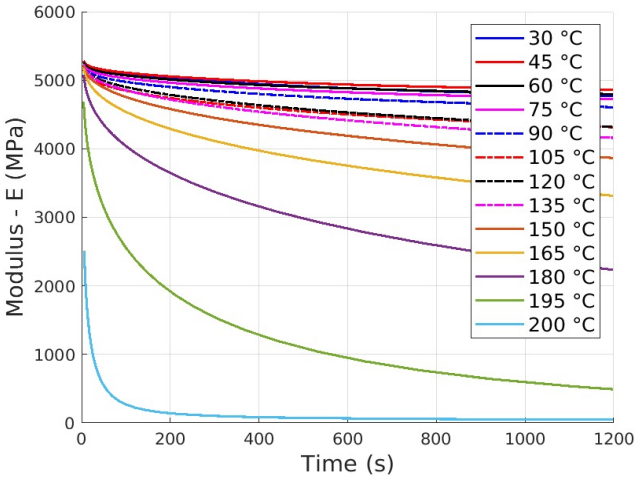

B)

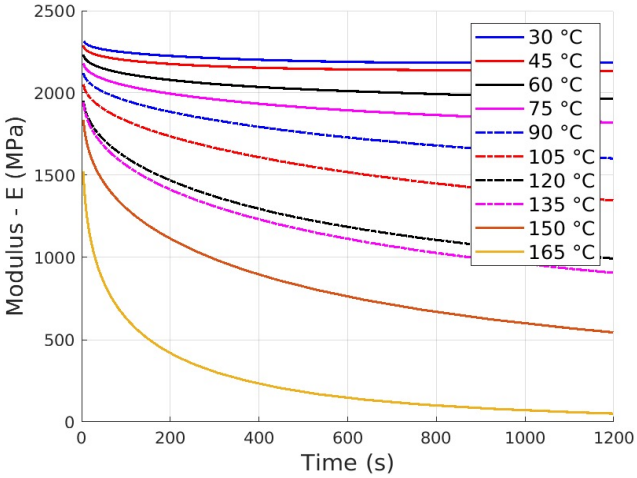

Figure 20 - Stress relaxation experiments carried for CF-PC at multiple temperatures. A) Stress relaxation behavior in the 1-Direction. B) Stress relaxation behavior in the 3-direction.

For a thermorheologically simple material, the stress relaxation curves obtained from stress relaxation experiments are shifted horizontally to form a relaxation master curve. Further, following the time-temperature superposition principle, the time shifting process also implies that the stress relaxation behavior characterized at a given temperature is equivalent to the behavior characterized over a longer time at a lower temperature [13]. Similarly, for a thermorheologically simple material, the relaxation times of the polymers scale in a similar way with temperature [13].

The stress relaxation experiments at different temperature were shifted with respect to a reference temperature T_o to generate a master curve as shown in Figure 21 A and B. The time shifting procedure is carried out in the logarithmic scale, and data for temperatures higher than the reference temperature are shifted to the right whereas data for temperatures lower than the reference temperature are shifted to the

left in order to form a continuous function that spans over multiple decades of time. During the time shifting process, the logarithm of the time shifted for a specific temperature provides the shift factor a_T which will be utilized to establish the relationship between time and temperature (time-temperature-superposition (TTS).

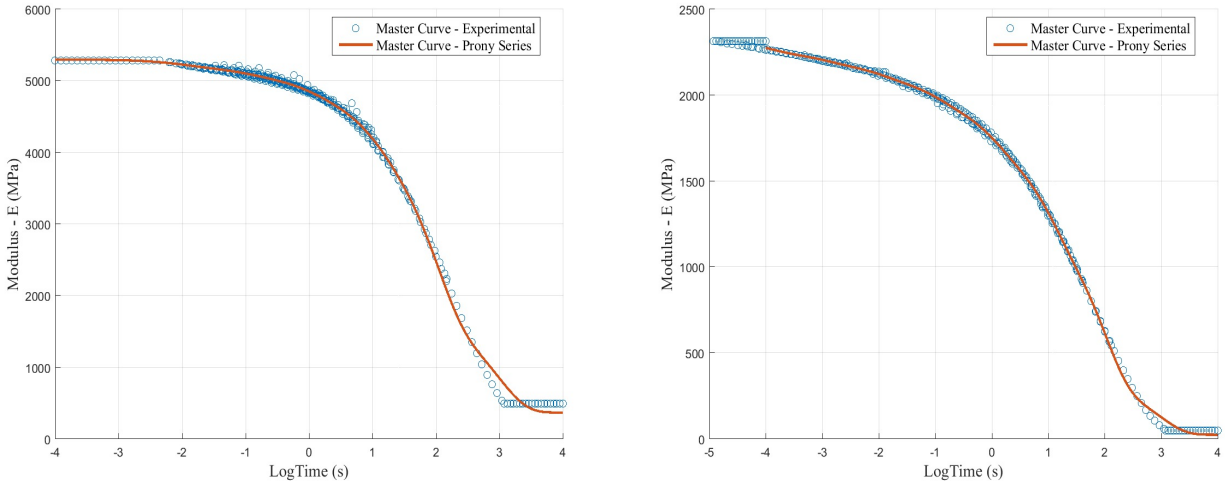

Figure 21 - Master curves characterized for the CF-PC in (A) 1-direction and (B) 3-direction.

Following generation of the master curve, a generalized Maxwell model consisting of N Maxwell elements (spring and dashpot configured in series) connected in parallel is used to capture the evolution of modulus with time given in the master curve [13]. Equation (2) shows the generalized Maxwell model which is also referred to as Prony series. The Prony series involves N coefficients E_w and N relaxation times λ_w which allows describing the material relaxation behavior over a broad time scale. The accuracy of the material description is controlled by the number of Maxwell elements utilized. To account for the modulus at equilibrium ($t \to \infty$), an equilibrium modulus E_∞ is used in Equation (4) [13]. To fit the Prony series to the experimental master curve, the procedure described by Brinson and Brinson [13] was adopted. Which suggests predefining relaxation times based on the range of reduced time obtained from the experimental results and to use between 1 and 2 Maxwell elements for each decade in time. Thus, eight maxwell elements were used to describe the thermoviscoelastic behavior of the CF-PC. The fitting of the Prony series to the experimental data is carried out through the local optimization routine lsqcurvefit available in Matlab©. Figure 21 shows the comparison between the master curve characterized experimentally and a Prony series with one Maxwell element per decade fitted to the same experimental data.

$$E(t) = E_\infty + \sum_{w=1}^{N} E_w \exp\left(-\frac{t}{\lambda_w}\right) \qquad (2)$$

To describe the behavior of the fiber reinforced printed material as a function of time and temperature, an orthotropic thermoviscoelastic constitutive relation is utilized. An orthotropic thermoviscoelastic material description requires nine different master curves, one for each independent stiffness tensor component. To reduce the characterization effort, the following assumptions were made for the relaxation behavior of the material based on the three orthogonal planes of material symmetry recognized from the experimental and virtual characterization of the printed material. Since fibers are dominantly aligned parallel to the printing direction (1-direction), they were assumed to dominate the relaxation behavior in this direction. In contrast, the matrix behavior was assumed to govern the relaxation behavior of the material in the transverse directions and shear planes. Consequently, two different sets of samples are investigated to determine both the fiber and matrix dominated relaxation characteristics. By testing samples for both the printing direction (1-direction, fiber dominated) and the transverse stacking direction (3-direction, matrix dominated), the experimental effort is significantly reduced. Following the argumentation above, the characterized matrix relaxation behavior was adopted for the modulus in the transverse in-plane direction (2-direction) and the

shear moduli. Thus, the relaxation behavior was normalized, and the resulting relaxation functions were used to scale the elastic properties characterized at room temperature experimentally and virtually. This assumption has shown promising results in previous validation of deformation predictions in additive process simulations [14].

To account for the effects of temperature on the viscoelastic behavior, the shift factor function $a_T(T)$ is used to establish a relationship between the real time t and a reduce time ξ. For the case of transient temperature conditions, the reduce time $\xi(t)$ can be expressed as given by Equation (3) [15]

$$\xi(t) = \int_0^t \frac{1}{a_T\big(T(\tau)\big)} d\tau \tag{3}$$

where τ is an arbitrary real variable in the interval $[0, t]$. A piecewise function consisting of a William-Landel-Ferry (WLF) equation and a modified version of the WLF equation [16] were used to describe the shift factors as a function of temperature (Equation (4)). While the WLF equations captures the dependance of temperature on the shift factors appropriately for temperatures around and above the glass transition temperature [15], the modified equation can be employed for temperatures below the reference temperature T_0 [16].

$$\log(a_T) = \frac{-C_1(T - T_0)}{C_2 + (T - T_0)}, WLF$$
$$\log(a_T) = \frac{C_1(T_0 - T)^{C_3}}{C_2 + (T_0 - T)^{C_3}}, modified\ WLF \tag{4}$$

Figure 22 shows the shift factors obtained experimentally and the fit of piecewise function to the experimental data.

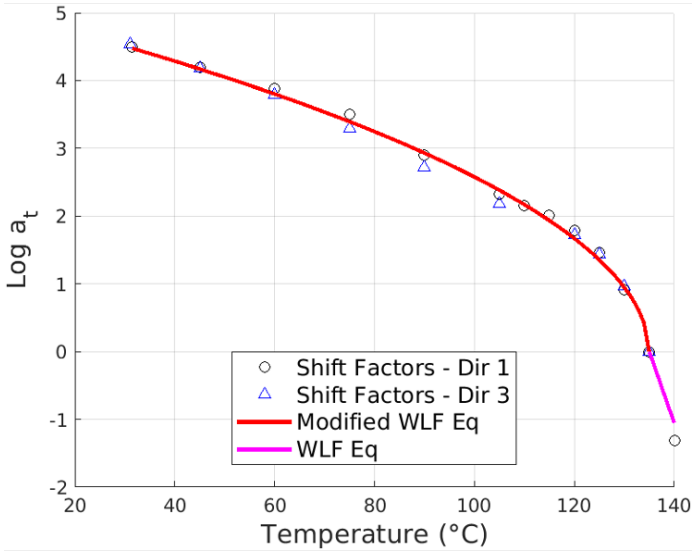

Figure 22 - Shift factors and shift factor function characterized for the CF-PC.

Table 7 lists the parameters of the WLF and modified WLF equations characterized for the CF-PC. The modified WLF equation is used for temperatures below the reference temperature, whereas the WLF equation is used for temperatures above the reference temperature.

Table 7 - Parameters of modified WLF equation characterized for CF-PC.

WLF Equation		Modified WLF Equation	
Parameter	Value	Parameter	Value
C_1	200.0	C_1	-206.99
C_2	946.28	C_2	500.00
C_3	NA	C_3	0.52
T_0 (°C)	135.0	T_0 (°C)	135.0

After generating master curves for the fiber dominated material direction (1-direction) and the matrix dominated direction (3-direction), the relaxation functions described through Prony series were normalized. Prony series for the polymer and fiber dominated properties were approximated using the normalized relaxation functions and the elastic properties determined experimentally and through micromechanics. The components of the stiffness matrix were constructed utilizing a quasi-elastic approximation [17]. Figure 23 shows the Prony series for the nine stiffness components used to describe the thermoviscoelastic behavior of the CF-PC printed in the LSAM system.

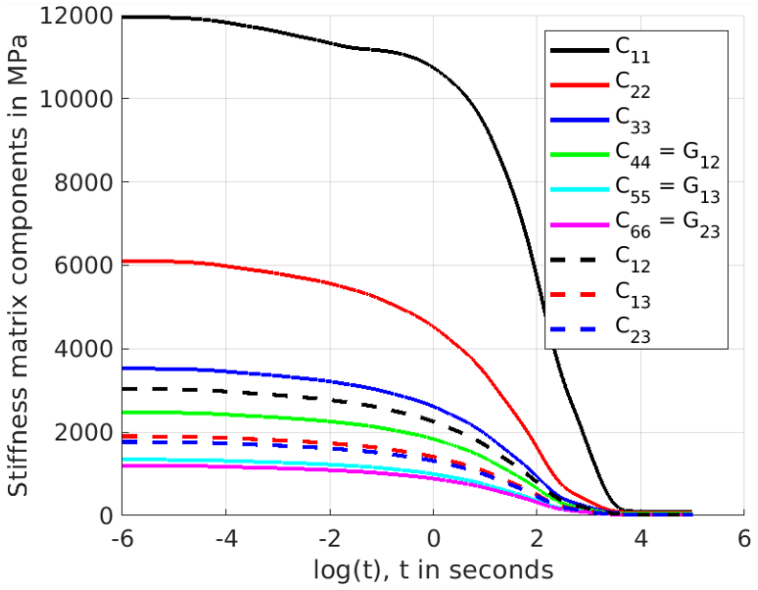

Figure 23 - Components of stiffness matrix described through Prony series for the CF-PC.

The Prony coefficients (expressed in MPa) for the nine stiffness components plotted in Figure 23 are listed in Table 8.

Table 8 - Prony series of stiffness components characterized for the CF-PC.

λ_w	C_{11}	C_{22}	C_{33}	C_{12}	C_{13}	C_{23}	C_{44}	C_{55}	C_{66}
Inf	86.64	61.64	35.56	30.74	19.24	17.88	24.92	13.46	11.97
1.00E-04	171.16	163.11	94.09	81.33	50.92	47.32	65.93	35.62	31.68
1.00E-03	232.31	176.07	101.57	87.79	54.96	51.08	71.17	38.45	34.19
1.00E-02	339.73	238.10	137.35	118.73	74.33	69.07	96.25	51.99	46.24
1.00E-01	0.00	416.79	240.43	207.82	130.11	120.91	168.48	91.01	80.94
1.00E+00	436.89	687.06	396.34	342.59	214.48	199.31	277.73	150.02	133.43
1.00E+01	1447.64	1267.73	731.30	632.13	395.75	367.76	512.45	276.81	246.20
1.00E+02	5228.54	2338.39	1348.92	1166.00	729.97	678.36	945.25	510.60	454.12
1.00E+03	4005.57	747.59	431.25	372.77	233.38	216.87	302.20	163.24	145.18

Crack Propagation

3D printed carbon composite materials produced from Thermwood's LSAM are orthotropic in nature. Short carbon fibers preferentially align along the print direction as thermoplastic melt flows from the nozzle [18]. Mechanical properties are higher along the print direction due this fiber alignment. These printed materials are weaker in the layer stack direction because mechanical properties are polymer dominated [2]. Failure occurs most often between the deposited layers, and fracture mechanics can help quantify this failure behavior. Capturing the fracture behavior of additively manufactured materials has become an important topic studied for fused deposition modeling (FDM) [19] and fused filament fabrication (FFF) [20]. Quantifying the fracture toughness of AM materials becomes important as efforts are made to evaluate crash worthiness in automotive applications.

Many methods of studying fracture mechanics exist for various material systems [21]. To study resistance to crack growth between printed layers, the critical stress intensity factors (SIF) in mode-I failure is evaluated, K_{IC}. Interlaminar fracture toughness has been selected as the most pertinent fracture test in large-scale additive manufacturing of structural parts like the Olli lower chassis produced by Local Motors. Especially important is that as 3D printed structures grow so does the possibility of defects/cracks within printed material. Characterizing stress intensity factors for interlaminar fracture is important to understanding material resistance to crack growth. Mode-I stress intensity factor K_{IC} is also important to the eventual development of suitable constitutive models such as a cohesive zone model and realistic modeling of critical energy release rates used in crash simulations.

Stress intensity factors are highly dependent upon geometry. Fortunately, ASTM D5045 does exist to help standardize the geometric dimensions[22]; however, this standard relies on the isotropic assumption. For most neat plastics and metals this assumption is perfectly fine, but not for fiber reinforced composites. This isotropic assumption does not apply since material properties can vary by orders of magnitude along the fiber reinforcement direction compared to the transverse direction of reinforcement. The material system being evaluated is 20% fiber weight fraction of carbon fiber reinforced polycarbonate. Modulus in the print direction is approximately 2.7 times greater than the transverse layer stack direction. For this reason, an isotropic assumption would not fit well for this material. An orthotropic assumption fits much better for this material system. This study compares the critical stress intensity factor derived from isotropic and transversely isotropic assumptions for LSAM produced composite materials.

Isotropic SIF Determination by Modified ASTM D5045-15

Fracture toughness is highly dependent upon geometry and much work has been performed to establish

validity requirements to adequately capture critical SIF's. For this reason, a modified ASTM D5045-14 test was utilized to quantify SIF's. Namely, geometric conditions stated within this standard were imposed on single-edge-notch-bend (SENB) specimen [22]. Information on which can be seen in Figures 24 and 25 below.

$$0.45 \leq a/W \leq 0.55$$

$$W - a \geq 2.5\left(\frac{K_Q}{\sigma_{YS}}\right)^2$$

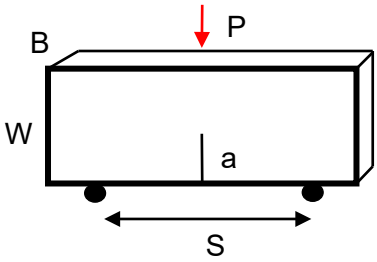

Figure 24 - Geometric validity requirements and SENB geometry definition

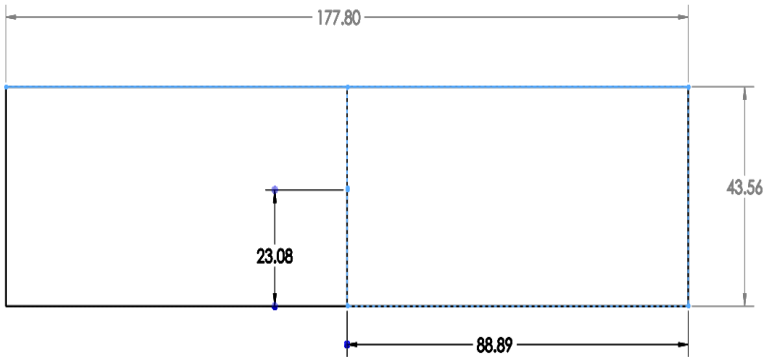

Figure 25 - Sample dimension in mm

Crack length and specimen width is defined by *a* and *W* respectively. The sample is tested in a 3-point bend configuration with the load applied at *P* while supported at the span *S*. Special care was taken to ensure the SENB samples were as close possible to $\frac{S}{W} = 4$ for the given 15.24 cm span. Specimen thickness *B* is also important to maintaining plane-strain assumptions during calculations. Stress intensity factors are calculated using Equation 5 (mode I critical stress intensity factor) and Equation 6 (definition of calibration factor) where $x = {}^{a}/_{W}$ and the load P_C is determined from the critical moment of crack extension [22]. Image capture at 25 Hz was utilized to determine the load at the moment of crack growth.

$$K_{IC} = \left(\frac{P_C}{BW^{1/2}}\right) f(x) \qquad (5)$$

$$f(x) = \frac{[1.99 - x(1-x)(2.15 - 3.93x + 2.7x^2)]}{(1+2x)(1-x)^{3/2}} \qquad (6)$$

Orthotropic SIF Determination by Digital Image Correlation (DIC)

Due to the orthotropic nature of the material system evaluated, a novel method of using digital image correlation to capture opening and sliding displacements was utilized. The method relies on a least-squares regression of a strain field to calculate the orthotropic SIF. The details of this method are highlighted in Tippur's work based on the classical equations developed by Irwin et. al [23][24]. This method can be

utilized for dynamic and quasi-static crack growth. For the purpose of this initial work, only the quasi-static SIF's were determined using Equation 7 (Sliding Displacement) and 8 (Opening Displacement) [24].

$$u(r,\theta) = K_I\sqrt{\frac{2r}{\pi}}Re\left[\frac{1}{\mu_2-\mu_1}(p_1\mu_2 z_1 - p_2\mu_1 z_2)\right] + K_{II}\sqrt{\frac{2r}{\pi}}Re\left[\frac{1}{\mu_2-\mu_1}(p_1 z_1 - p_2 z_2)\right] \quad (7)$$

$$v(r,\theta) = K_I\sqrt{\frac{2r}{\pi}}Re\left[\frac{1}{\mu_2-\mu_1}(q_1\mu_2 z_1 - q_2\mu_1 z_2)\right] + K_{II}\sqrt{\frac{2r}{\pi}}Re\left[\frac{1}{\mu_2-\mu_1}(q_1 z_1 - q_2 z_2)\right] \quad (8)$$

For plane strain assumption of interlaminar fracture of an orthotropic material with x-z and y-z planes of symmetry planes, Equation 9 is the complex root of Equation 10. Equations 11 and 12 are material constants and Equation 13 is needed to satisfy the boundary conditions of the crack contour.

$$\mu_j (j = 1,2) \quad (9)$$

$$S_{11}\mu^4 + (2S_{13} + S_{55})\mu^2 + S_{33} = 0 \quad (10)$$

$$p_j = {\mu_j}^2 S_{11} + S_{13} \quad (11)$$

$$q_j = \mu_j S_{13} + \frac{S_{33}}{\mu_j} \quad (12)$$

$$z_j = \sqrt{cos\,\theta + \mu_j\, sin\,\theta} \quad (13)$$

In the above equations, K_I is the mode-I SIF, K_{II} is the mode-II SIF (which is expected to be near zero for this symmetric loading case), *u* and *v* are the sliding and opening displacements, and S_{11}, S_{22}, S_{33}, S_{12}, S_{13}, S_{55}, and S_{66} are coefficients of the *S*-matrix as determined experimentally and by assuming transverse isotropy [25]. The material properties of this material system were determined from previous characterization at Local Motors by ASTM D638 and ASTM D7078. DIC was also used in parallel to determine Poisson's ratio. The material properties input used are $E_1 = 7.67\ GPa$, $E_3 = 2.82\ GPa$, $G_{13} = 1.96\ GPa$, $v_{13} = 0.35$ with a transverse isotropic assumption.

DIC imaging at 25 Hz was used to capture the full-field strain behind the crack tip during SENB testing. The DIC system captures these strain fields, shown in Figure 26, in a rectangular coordinate system. Note how the sample presented in Figure 24 and Figure 25 has been rotated 90° in Figure 26 to match the typical convention of fracture mechanics. Conventionally, the crack front runs horizontally starting on the left-hand side. All the following analysis is conducted utilizing this fracture mechanics convention.

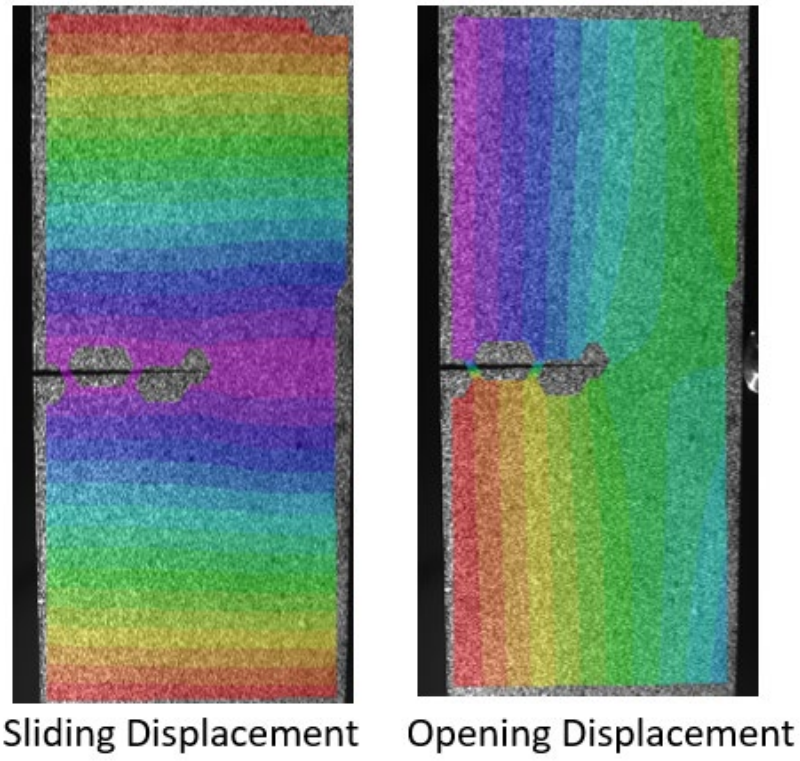

Figure 26 - DIC captured opening and sliding displacement contours surrounding crack front

The rectangular coordinate system is then converted to a polar coordinate system originating from the crack-tip. Crack-tip location is manually selected at each frame using a MATLAB script to convert the rectangularly mapped strain field into the polar opening and sliding displacements needed for calculation. Figure 27 highlights this process.

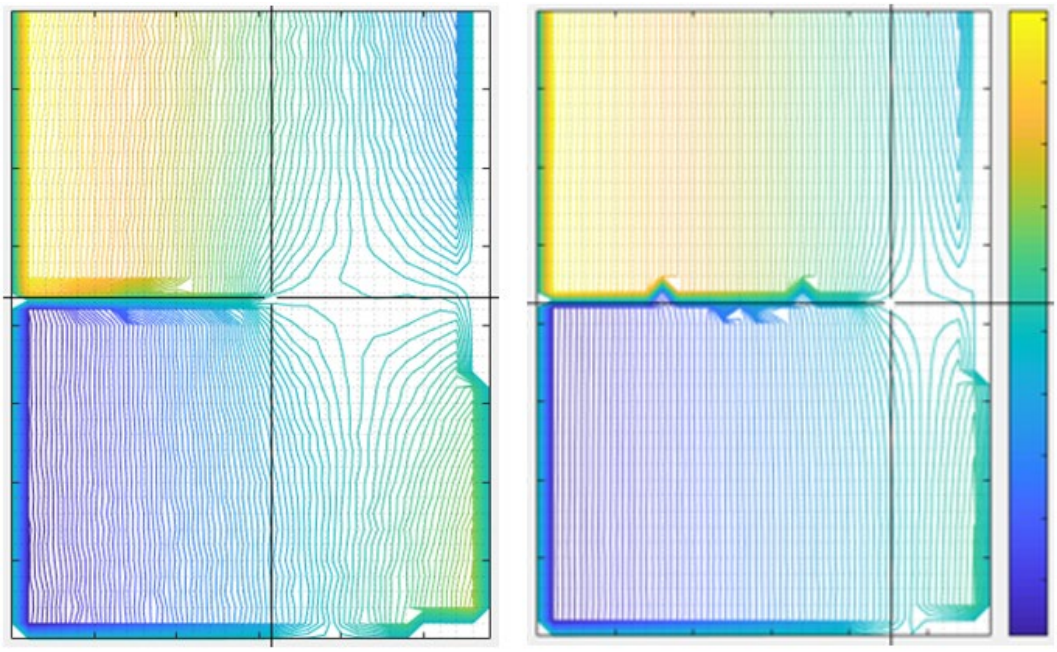

Figure 27 - Selecting the crack tip before and after crack extension

The crack-tip location is carefully selected and measured over time to determine the critical moment before crack extension. Once the critical moment has been determined, then the opening and sliding displacements are sampled from behind the crack-tip. Figure 28 visualizes the locations from which the opening and sliding displacements are taken from with respect to the crack-tip.

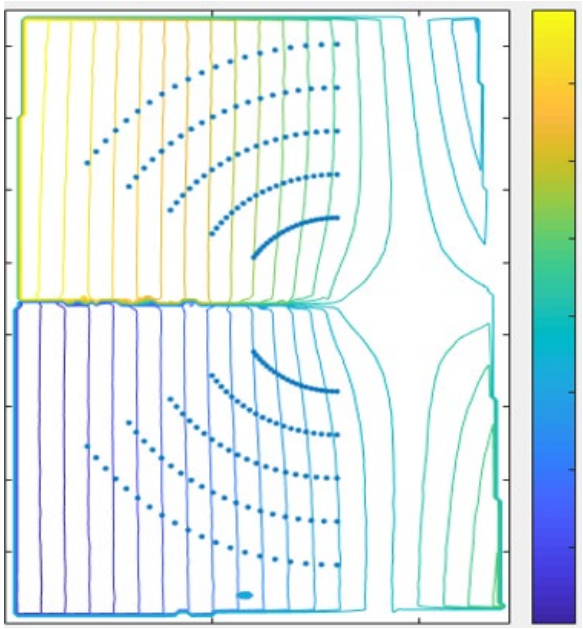

Figure 28 - Sampling locations for opening and sliding displacements

Once the opening and sliding displacements have been determined at the critical moment, then K_{IC} can be determined.

Sample Preparation

The validity requirements established in Figure 24 dictated the sample geometry, but great effort was made to produce pre-notched SENB samples. To achieve the desired pre-notched effect, a layer of Polytetrafluoroethylene (PTFE) tape was placed between printed layers as shown in Figure 29.

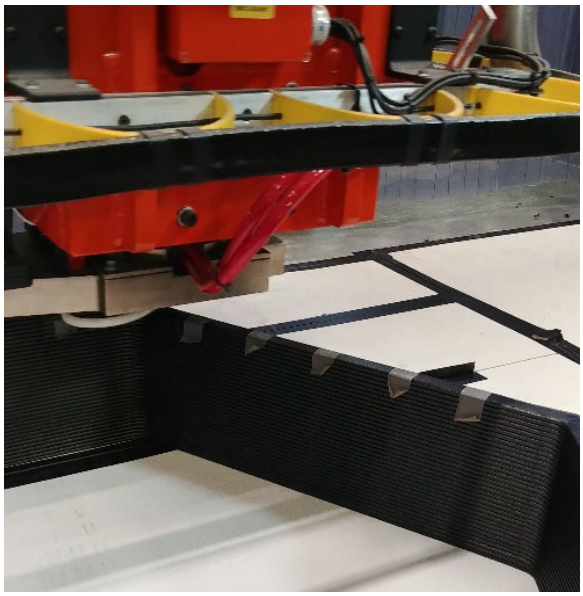

Figure 29 - Printing with PTFE tape between layers

A single walled (one bead thickness) hexagon was used as the print structure. Each wall of the hexagon was then cut away and planed to about 0.4” using an industrial planer before being sanded using a 400-grit sandpaper. Hexagon walls were cut to 12” by 16”. This is exemplified in Figure 30.

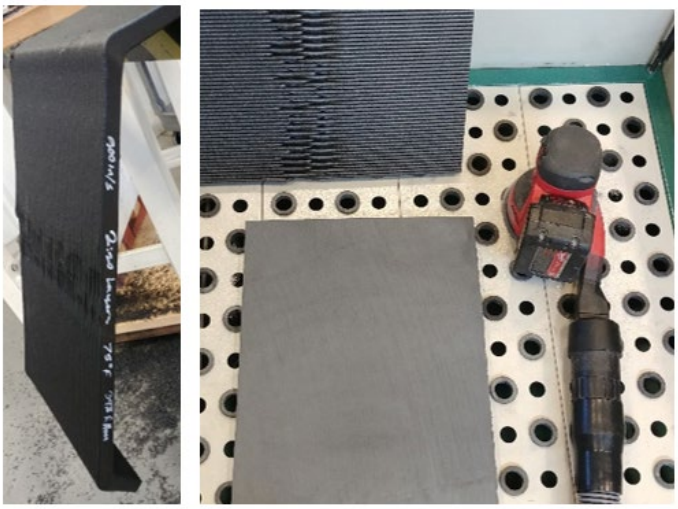

Figure 30 - Cutting the hexagon walls and sanding the planed surface

Fortunately, this material clearly shows the embedded PTFE tape on the sanded wall surface. To center the SENB sample on the embedded PTFE tape, a SENB sample stencil was made to mark the wall surfaces, Figure 31.

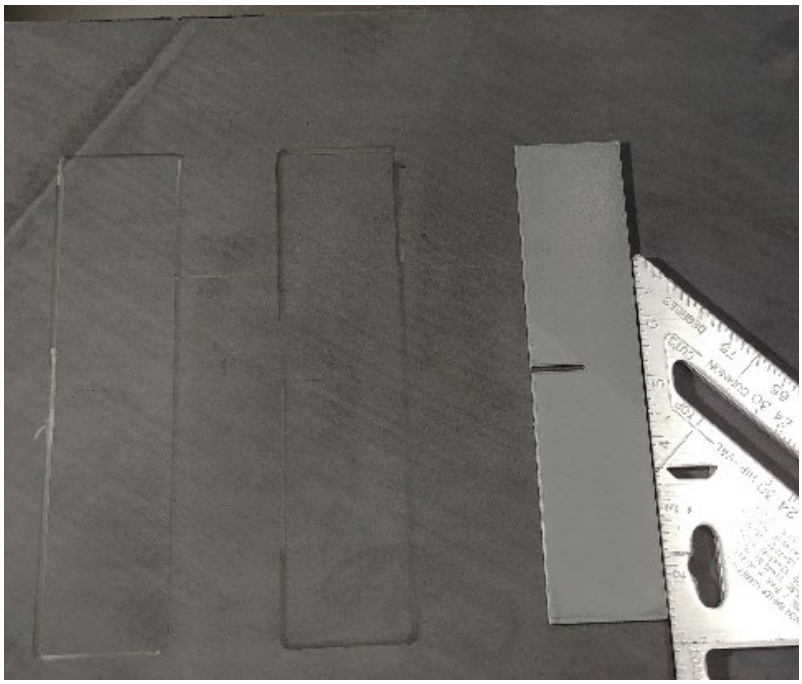

Figure 31 - SNEB sample stencil centered on embedded crack

The stencil was placed in such a way that the PTFE crack occupied half the sample width. Cuts into the hexagon walls were made with a diamond bladed tile saw. Cuts were made to expose one end of the PTFE tape to allow for exposure of the crack front, Figure 32.

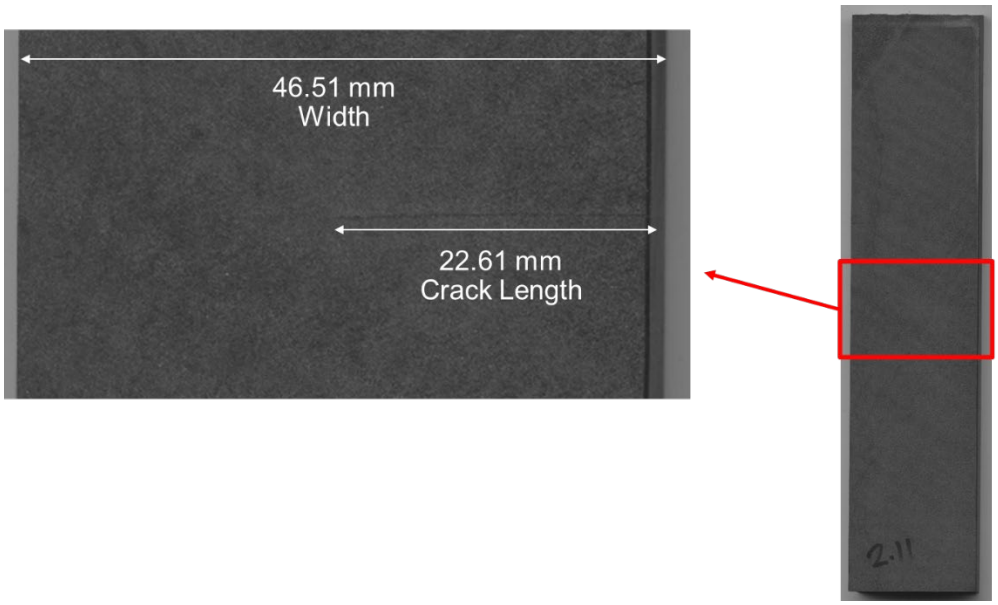

Figure 32 - Cut sample with exposed crack front

Lastly, the SENB samples were speckled and mounted on an MTS 810 using a 3-point bend fixture, Figure 33.

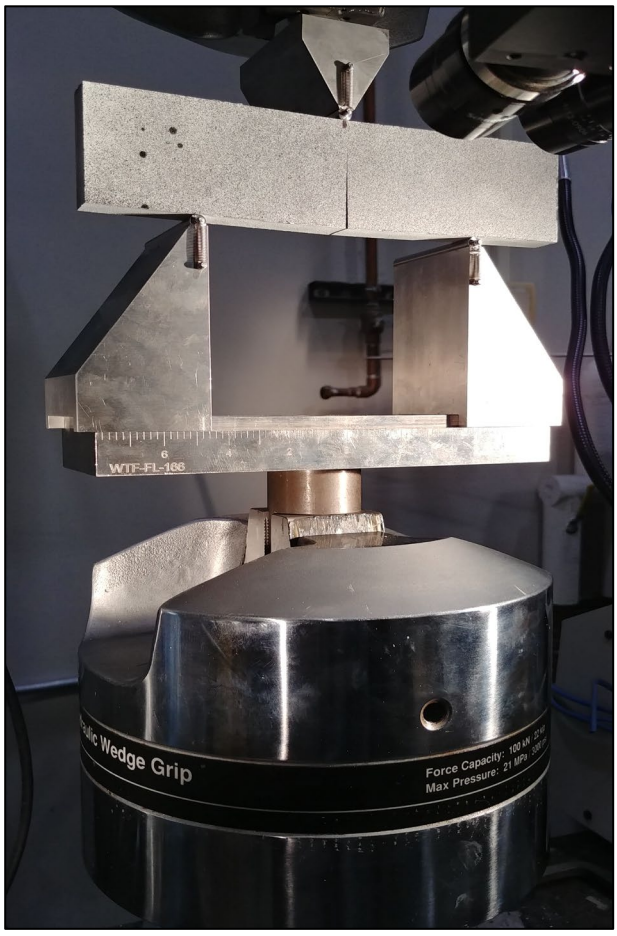

Figure 33 - Speckled SENB sample with DIC setup

Experimental Design

Preliminary process variability testing of the LSAM printed material system showed tensile strength has a strong dependence on time between layer deposition (layer time). Layer time is an indicative of the cooling that takes place from the previous printed layer. As the material cools beyond a point, then adhesion of the next layer is affected. An approach was taken to evaluate the stress intensity value relationship with layer time in a similar way. For this study 2:20, 3:20, 4:20 and 5:20 minute layer times were utilized to print the PTFE tape embedded hexagon structures shown by Figure 34. Both SENB samples and tensile samples were produced from each hexagon to characterize both the Z-direction strength and interlaminar fracture toughness dependence on layer time. Wall 1 is defined by the start / stop seam of which no samples were taken. Wall 2 also was not used for producing samples because the steady state deposition is not reached. Walls 3-5 contain the embedded crack front for SENB samples. Five samples were generated from each wall for 15 total samples per hexagon. Wall 6 was used for four type III ASTM D638 samples to evaluate the Z-direction strength dependence on layer time as well.

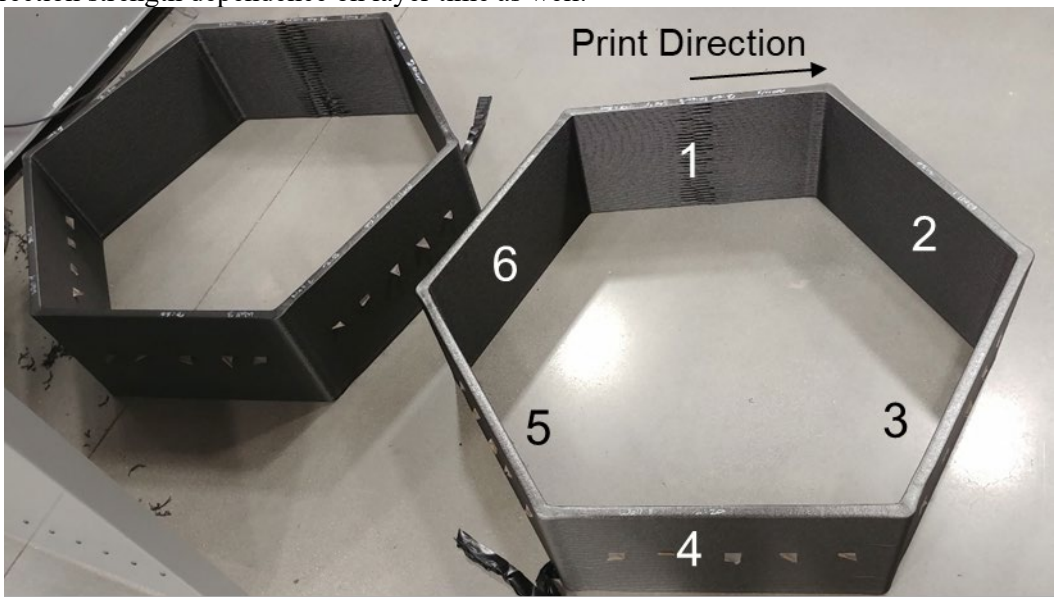

Figure 34 - Layer time print structures for SENB and tensile samples

Tensile Testing Results

As the equations for sliding and opening displacement have tensile modulus as an input into the equation, it was important to have accurate results for tensile modulus. Tensile testing was performed on the different layer times to use as inputs for SENB for the samples printed at the same layer times A type III tensile sample was used to measure the Z-direction strength and modulus at 2:20, 3:20, 4:20 and 5:20 minute layer times. Z-direction modulus was shown to be independent of layer time, Figure 35.

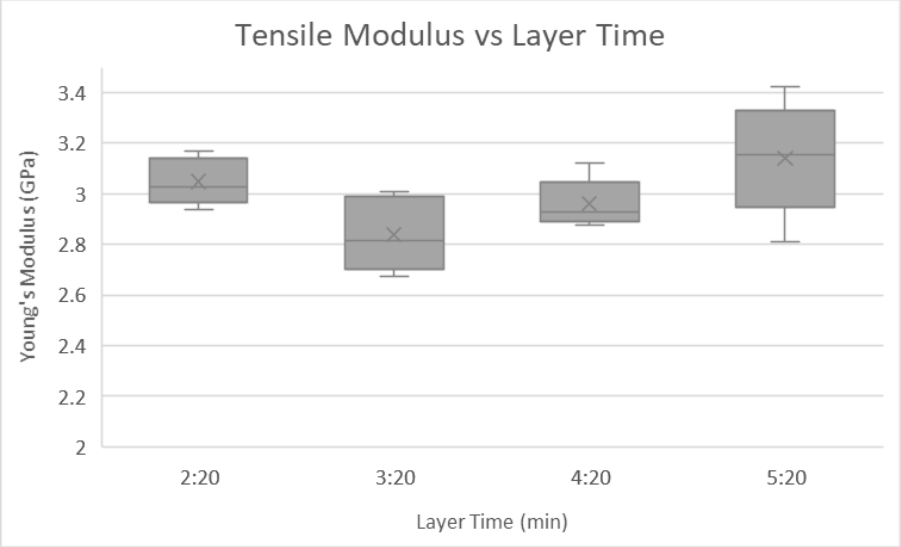

Figure 35 - Z-direction tensile modulus by layer time

Ultimate stress and strain values of 2:20, 3:20, 4:20 and 5:20 minute layer times were shown to be strongly dependent on layer times, Figure 36.

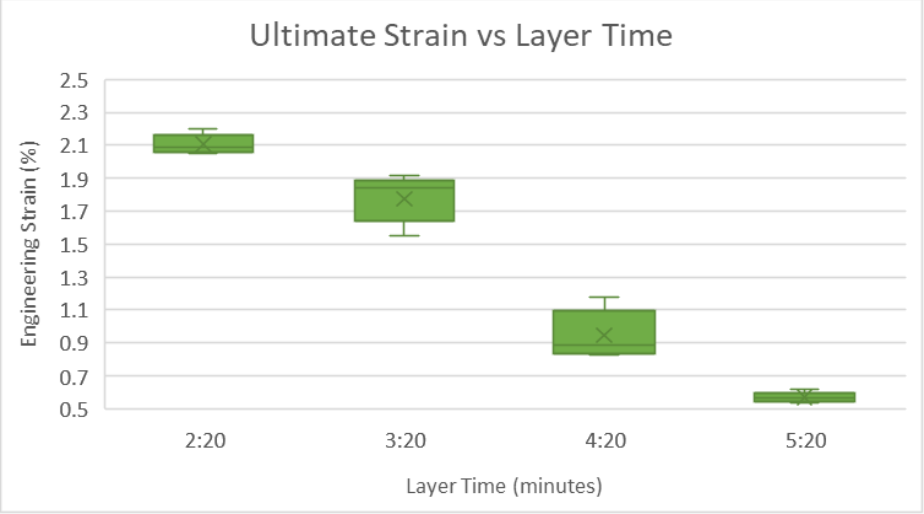

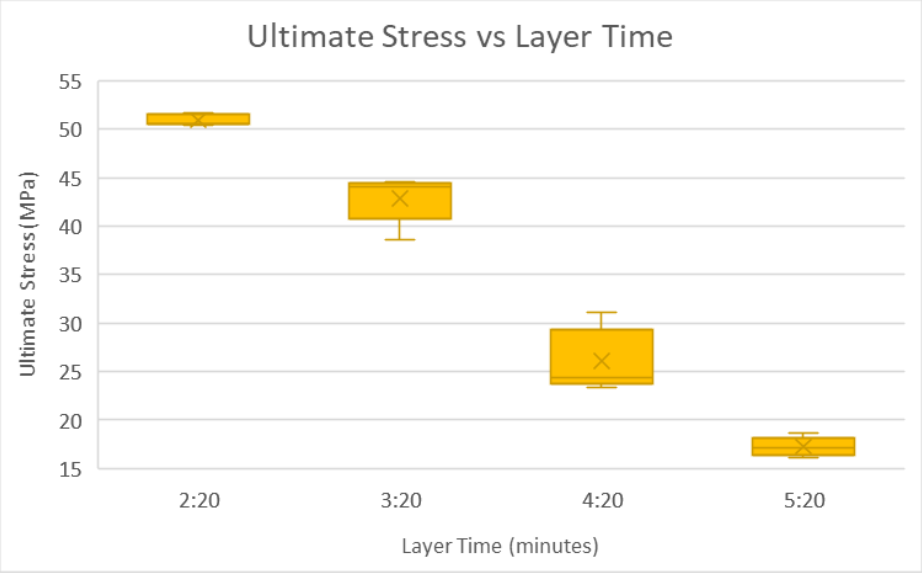

Figure 36 - Ultimate strain and stress with respect to layer times

These results are in strong agreement with previously observed phenomena. Strength properties degrade by over 50% from 2:20 to 5:20 minute layer times. Clearly a strong correlation exists between the tensile strength properties and layer time. The best explanation is that cooling of the previous printed layer is affecting the interface with the next layer deposited. Residual stresses can develop at the interface between layers given a large enough thermal gradient.

Fracture Toughness Results

Traditionally, the stress intensity values of isotropic material systems are easily measured via ASTM D5045. This standard is more difficult to apply towards orthotropic material systems. For this reason, the ASTM D5045 method (Figure 37) was compared against the experimental orthotropic SIF determination method (Figure 38). The results between the two measurement strategies are very agreeable. Both methods produced average SIF results within the standard deviation of each other. The average critical SIF decreased ~40% from 2:20 – 5:20 minute layer times, albeit with relatively higher standard deviations compared to the tensile strength results. Layer time appears to significantly impact the critical stress intensity factors for this LSAM printed material system. It is hypothesized that as layer times increase the thermal gradient between printed layers contributes to higher residual stresses. Higher residual stresses along the interface are contributing to the drop in fracture toughness values with increased layer times.

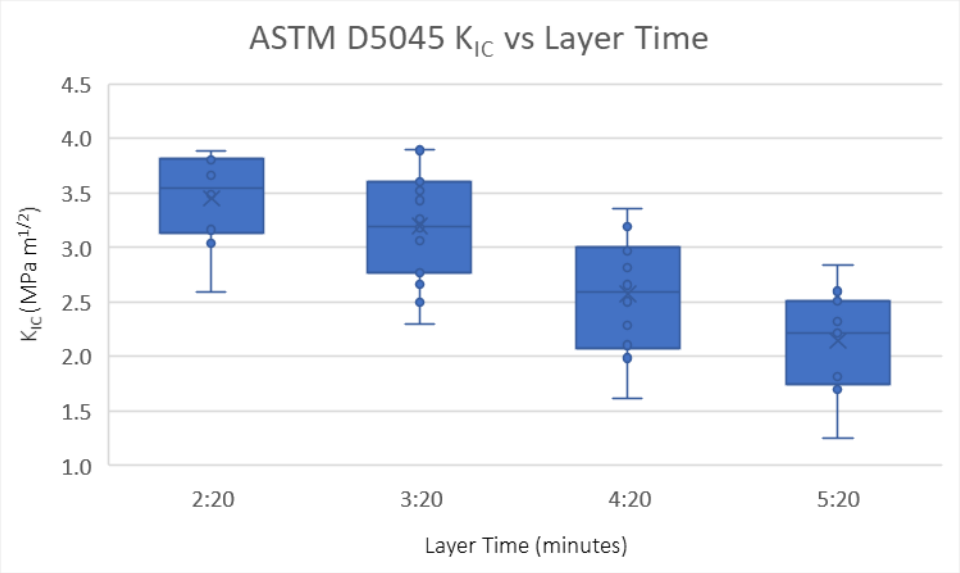

Figure 37 - Critical stress intensity factor values determined via ASTM D5045 method

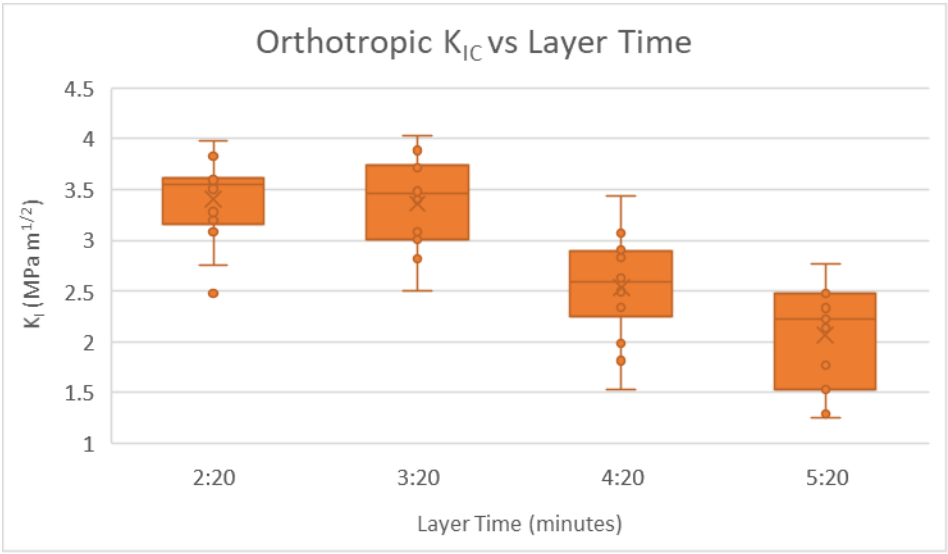

Figure 38 - Critical stress intensity factor values determined via Orthotropic method

The critical interlaminar stress intensity values of this material system should be highly dominated by the resin matrix – polycarbonate. Literature reports the fracture toughness of polycarbonate to be 3.06 MPa $m^{1/2}$ [26]. Additional literature reports the critical SIF to vary between 3.0 and 4.1 MPa $m^{1/2}$ depending on the notch sharpening method. The experimentally determined SIFs from this work are in strong agreement with the literature [27].

Between the isotropic and orthotropic methods of determining stress intensity values for this LSAM printed material it has been shown that both methods produce similar results. When considering the marginal difficulty of evaluating the orthotropic SIF compared to the isotropic SIF, it can be recommended to utilize the isotropic ASTM D5045 method for statistically similar results. Strong agreement between experimental results and literature helps reaffirm both characterization strategies as producing accurate results. SIF degradation over longer layer times is likely due to higher residual stresses generated from thermal gradients between printed layers. Layer times greater than 3:20 should not be exceeded if intending to maintain high fracture toughness of LSAM printed carbon fiber reinforced polycarbonate materials.

Multimaterial Printing

Milestone 3.12.3.2 Demonstrate multi-material printing and produce test article with at least two different materials.

ORNL, in collaboration with Cincinnati Inc., has developed multi-material printing capability on the BAAM system. This enables large scale printing of parts with multiple materials to obtain tailored properties, which may be site specific properties, or functionally graded material (FGM) properties [8], [28]. Modifications to the BAAM to enable multi-material printing include a new extruder design to accommodate a dual feed hopper (Figure 39), a two-dryer system, and a gravimetric blender system for mixing pelletized materials. The dual feed hopper makes it possible to switch between the two materials during the printing process and the blender enables mixing feedstock pellets with varying compositions of fillers, for example, blowing agents for extruding thermoplastic foams.

System Description

The BAAM system can process a variety of thermoplastics and composites including low temperature thermoplastics, composites of high-performance polymers, thermoplastic foams, elastomers, bio-derived materials, recycled composites etc. The combination of materials chosen for a multi-material build depends on the desired properties and functionality for end-use application and must be such that they are melt processable in a similar temperature range. The material transition regions, i.e., portions of the extrudate with mixed composition of the two materials while switching from one material to the other, can either be incorporated into the build for functionally graded properties or purged periodically, depending up on the requirements for the build.

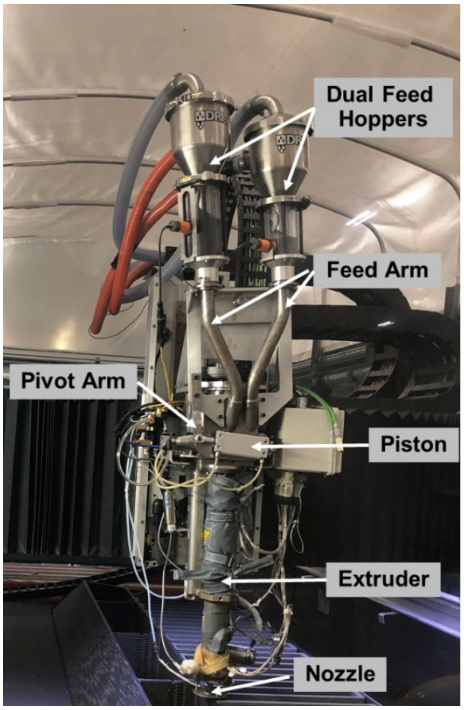

Figure 39 - Dual feed hopper system on the BAAM.

The test part chosen for this demonstration is a crash structure as shown in Figure 40. This design was chosen as it has been utilized in crush scenarios prior to this work and as such information was known on

the failure behavior it would exhibit. This made it easy to implement a multi-material strategy that was probable to have a positive impact.

Sample Geometry

The two materials chosen for this multi-material print were carbon fiber reinforced acrylonitrile butadiene styrene (CF-ABS) procured from Techmer PM, and CF-ABS foam. CF-ABS foam was obtained by blending the CF-ABS pellets with 4% by weight Expancel® microspheres (blowing agents) in the gravimetric blender prior to feeding the pellets to the hopper. Test specimens were printed such that the outer perimeter (or walls) was CF-ABS foam, and the inner perimeter was CF-ABS. For crash structures, this can potentially provide high energy absorption without having a high initial resistance. Crash structures should be designed to avoid a huge initial resistance, specifically a high initial stress peak, followed by low stress in a stress-strain curve. Moreover, a CF-ABS material exhibits a high stiffness. By placing a foam in the outer side and CF-ABS inside the structure, it is expected to avoid a high initial peak, and instead, the structure is expected to deform first and the inner structure (CF-ABS) adds a gradual resistance as the impactor pushes through the structure.

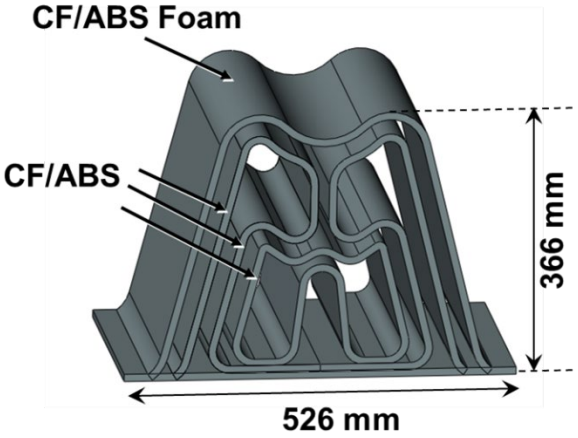

Figure 40 - Crash specimen design.

These crash structures were printed using a 5.08 mm (0.2 in) diameter nozzle and the set temperature in the four zones of the extruder and the nozzle tip were 176 ℃ in zones 1 and 2 and 249 ℃ in zones 3, 4 and the nozzle, and the measured melt temperature between the extruder and the nozzle was 249 ℃. The print bed was heated to 100 ℃. Each build had 121 layers with a layer (or bead) height of 2.54 mm (0.1 in) and were printed continuously as shown in Figure 41a. The parts labelled 1 and 2 in Figure 41a had the two materials deposited at the desired locations in the build and the parts labelled 3 and 4 in Figure 41a incorporated the material transition portions as the hopper switched from CF-ABS to CF-ABS foam and vice versa during the print. Optimal screw speed and gantry speed conditions, accounting for the differences in rheological properties of the two materials, were incorporated into the Slicer settings for the two materials and the transition (mixed material) regions to obtain beads of consistent geometry. In addition to these multi-material parts, controls samples were printed using CF-ABS as shown in Figure 41b with the same layer time as the multi-material build to compare the crash performance.

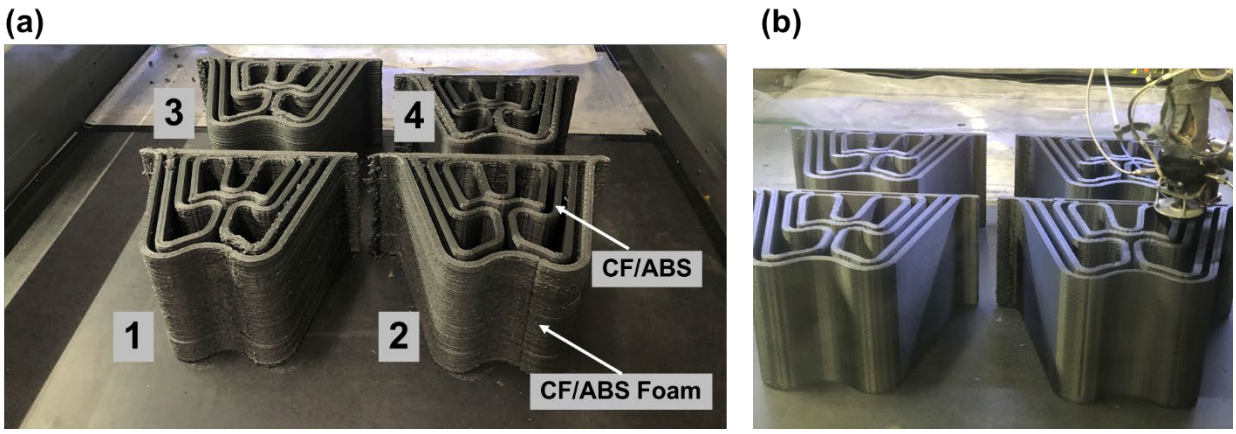

Figure 41 - (a) Continuous printing of multi-material crash structures. Part 1 and 2 are test parts with site-specific material deposition and parts 3 and 4 are parts capturing the material transition sections. (b) Control samples printed using CF-ABS.

Dynamic testing

The printed samples were then transported to Local Motors for dynamic testing. A free fall drop tower was used to evaluate the energy absorption of the multi-material samples and the single material CF-ABS control samples. The primary indicators of performance were the peak force, max stroke, average force, total energy absorbed, and energy absorbed per unit of mass. The test method was made to imitate the structure receiving a large impact, much like if the structure was on the front of a vehicle. To imitate this a sled with a known mass is hoisted a set distance above the specimen. The sled is then released from this height and allowed to accelerate at the rate gravity minus air and system resistance. Accelerometers are mounted on the sled to record the acceleration of the sled. The sled then impacts the specimen which will absorb some energy and disperse the rest to the platen beneath it. The platen beneath the specimen is instrument with load cells to record force received by the platen. Sled mass during testing was 454 kg, with an impact speed of 22.5 km/hr (17734 J of kinetic energy at time of impact). Data recorded includes total force and accelerations at 10 kHz, and two channels of high frame rate (HFR) video at 960 frames per second (FPS). The general test setup is shown in Figure 42.

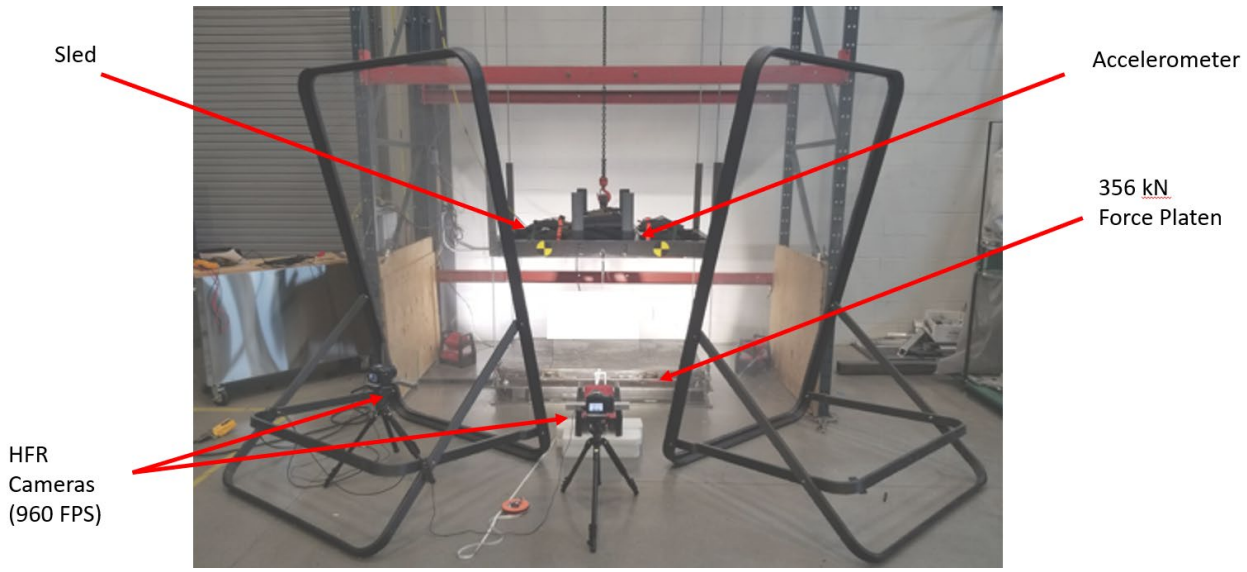

Figure 42 - Image of drop tower test setup

Each test was started by raising the sled to the correct height, 2 meters, to reach the desired impact speed. Once the sled reached the correct height the sample was placed in the center of the platen against a locating stop. A computer running a custom LabView™ program is connected to the sled release mechanism, cameras, accelerometers, and load cells. The computer acts as the activation trigger for the camera and sled release mechanism. It also records the data outputs from the test rig. Once the program has registered the camera connection and a physical safety is released the testing can begin. Once the program is initiated the sled is released and everything starts recording. After the test run is completed, the platen is cleared, and the sled reset so testing of the next sample can begin.

All 6 samples were weighed to determine mass differences between samples, weights can be seen in Table 9. Once the data for the remaining 6 samples had been obtained it was processed to provide the primary indicators of performance mentioned earlier. First the output is trimmed to only include data between the sled initially contacting the sample to the bounce back of the sled. After this most of the processing involves the acceleration curve. Integration is performed on the acceleration data to provide velocity, but this integration creates the need for a constant. This constant is the velocity of the sled when it contacts the samples, which is can be calculated using the free fall equation or high-speed camera footage. For these samples the free fall equation was chosen. High-speed camera footage was not used as the drop height was considered to be low enough that air resistance would play a negligible role in acceleration. Once the constant has been calculated, the data is integrated again to provide stroke. Now that stroke data has obtained, it can now be plotted against the force data. An integration of this data calculates the energy absorbed by the sample, at which point all primary performance indicators are available.

Table 9 - Masses of samples used in dynamic testing

Sample Number	Mass (kg)
1 (Control Sample)	19.25
2 (Control Sample)	18.80
3 (Control Sample)	18.95
4 (Control Sample)	18.60
1 (Multimaterial)	13.45
2 (Multimaterial)	11.95

Figure 43 displays both force versus stroke and energy versus stroke for the samples tested in dynamic testing. It can be seen in both graphs that the curves have similar shapes, meaning they all failed in a comparable manner. The large standout from the group is control sample 2, it had the largest stroke almost 350 mm. There is no obvious reason for this increased stroke in this sample. Multi-material sample 2 also exhibits a much smaller peak force than any other sample, which if replicable in future samples would be a large advantage for multi-material crush structures.

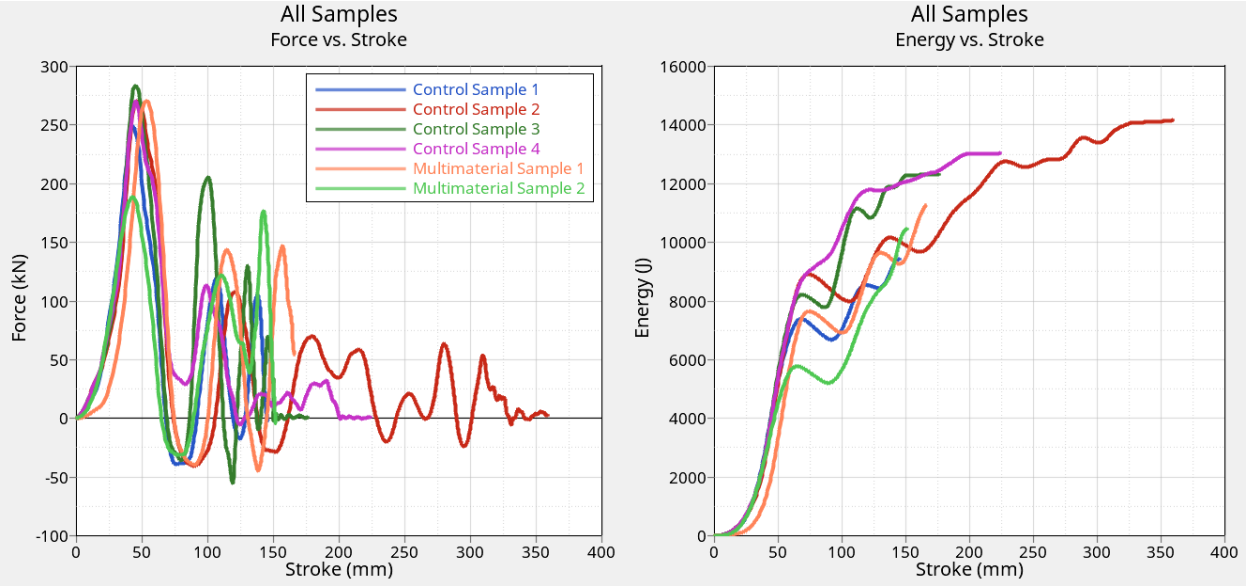

Figure 43 -Results of dynamic testing on control and multimaterial samples.
(left: force generated per millimeter of stroke graph, right: energy absorbed per millimeter of stroke graph)

The graphs above show the results of the dynamic testing; however, it is important to calculate the performance indicators to easily compare the two types of samples. These indicators can be seen in Table 10 below. The peak force of the multi-material samples was lower than the control samples, but the control samples showcase a lower average force. More tests would have to be conducted to determine a possible reason behind this. Control samples showed a much higher maximum stroke than the multi-material samples, however the multi-material samples absorbed much more energy in their shorter stroke. The multi-material samples also absorbed more energy per unit of mass, absorbing 32% more energy per kilogram of material than the control samples. Multi-material samples absorb more energy in a given span, but they also weigh less as well. These are both important qualities especially in size and weight constrained environments. It should be noted that two samples, does likely not provide the clearest representation of the multi material samples. More of each sample would allow for more confidence in the data given this study's small sample size. Iterating the design of the crush samples to optimize for the performance indicators below would also allow the multi-material samples to show their flexibility and further exemplify the advantages of a multi-material approach. These are possible starting points for future studies on LSED process.

Table 10 - Summary of dynamic testing results

	Control Samples (Avg)	Multimaterial Samples (Avg)
Peak Force (kN)	268	229
Max Stroke (mm)	226	158
Average Force (kN)	34	69
Total Energy Absorbed (J)	12200	10800
Mass (kg)	18.9	12.7
Energy Absorbed / Mass (J/kg)	648	856

Energy Absorbed / Stroke (J/mm)	54.0	68.4

Nondestructive Evaluation

Milestone 3.12.2.1 Determine the effectiveness of available NDE technology to inspect large scale extrusion deposition structures and identify defects 2mm in size or larger

The goal of this project was to develop an NDE method to identify inter-bead defects in 3D printed samples by monitoring thermal energy changes in the part during cooling or monitoring thermal energy changes after apply applying heat to the part. 3D printed test samples without obvious defects and test samples with known defects of different sizes and location were provided for NDE testing to verify the success of the NDE methods that were developed. Local Motors provided two printed test samples shown in Figure 44 that the Vanderbilt team could use for initial NDE experiments. Both samples were printed on the same 3D printer using the same type of material. Print sample 1 had overlapping layers in the center of sample that increased the thickness (see Figure 44a) and print sample 2 has no overlapping layers (see Figure 44b). Since there is no non-destructive method to identify inter-bead defects, there was no way to verify if there were existing inter-bead defects in these first two test samples.

(a) (b)

Figure 44 - a) Printed sample 1 and b) printed sample 2

Heat Unit Per Area Approach

Printed sample 1 and printed sample 2 were each heat soaked for 24 hours in an oven at 60 C. Each of the test samples was removed from the oven and full field temperature data was recorded using a FLIR A8303sc IR camera for 4 hours as each test sample cooled in the open air in the lab which was at 22 °C (72 °F). The temperature data was used to estimate cumulative heat energy loss at each pixel in the IR images collected on each of the test samples. Heat per unit area (q) lost through the surface of each sample at a particular pixel through convection (at sample *i*) was defined by equation 14 where *h* is the convection coefficient.

$$q_{pix}^{i} = h\left(T_{pix}^{i} - T_{env}\right) \tag{14}$$

Total energy lost to the environment from a pixel location was calculated by integrating heat loss over time as shown in equitation 15.

$$E_{pix}^{i} = E_{pix}^{i-1} + \frac{1}{2}\Delta t(q_{pix}^{i} + q_{pix}^{i-1}) \tag{15}$$

Next, an outlier detection algorithm was applied to locate potential flaws in test samples. Surface temperature distribution data was extracted from the IR video every 10 seconds and the cumulative energy

loss values were calculated. Pixels with an energy loss value outside 3 standard deviations (3σ) from the mean energy loss of all pixels were identified as outliers for that particular frame as illustrated in plot in Figure 45. An outlier score was calculated for each pixel after each frame. The outlier score was equal to the percentage of frames in which a pixel was an outlier. A higher outlier score indicates a higher flaw potential at that location.

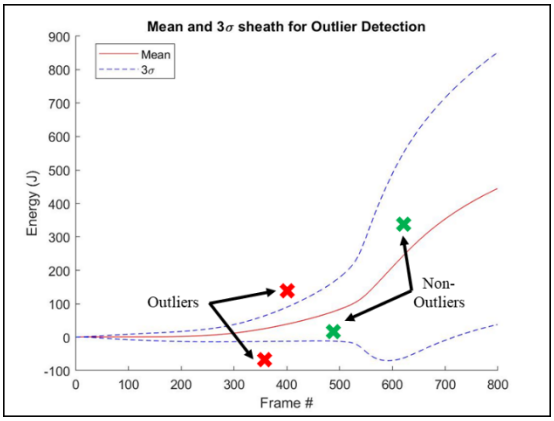

Figure 45 - Plot showing pixels with an energy loss value outside 3 standard deviations (3σ) from the mean energy loss of all pixels identified as outliers for that particular IR frame

The outlier detection algorithm was applied to the IR temperature data collected on each of the printed samples to locate potential flaws. Figure 46 shows the surface energy loss and outlier scores for printed sample 1. The thickness change in printed sample 1 cooled at a slower rate than the rest of the part that resulted in a false positive in the outlier score. Figure 47 shows the surface energy loss and outlier scores for printed sample 2. The outlier score for printed sample 2 indicates that there could be a potential flaw in upper left corner of the test sample. However, there was no NDE method available to verify that there was an inter-bead defect in printed sample 2.

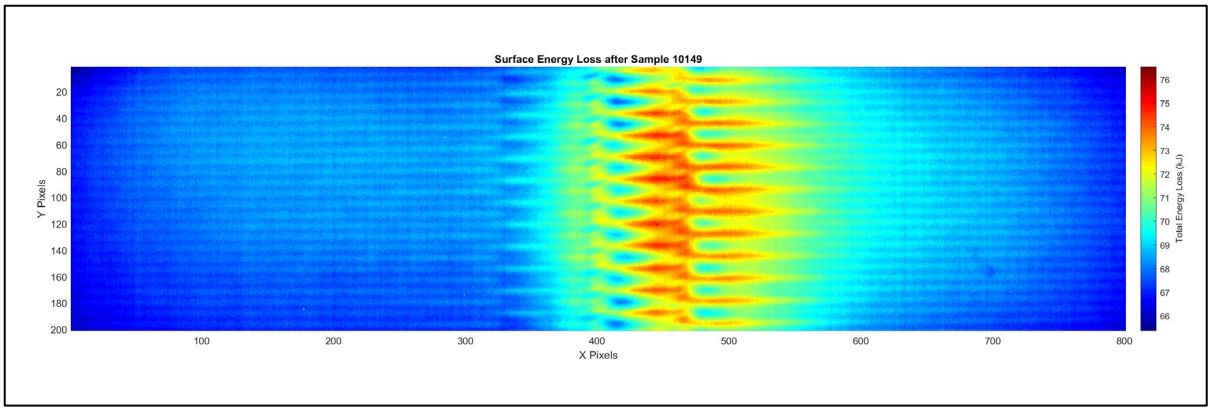

(a)

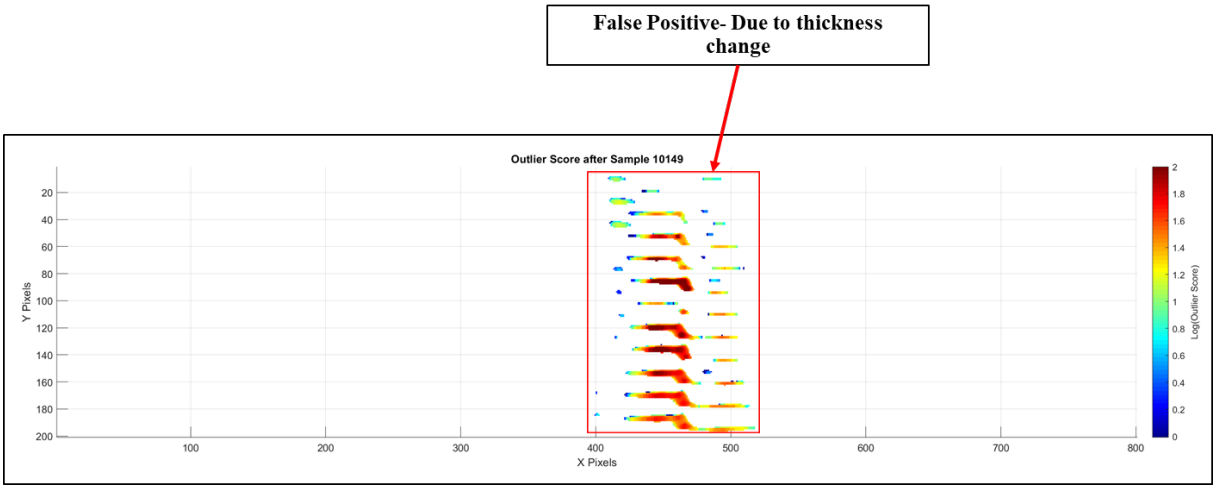

(b)

Figure 46 - a) Surface energy loss and b) outlier score for printed sample 1

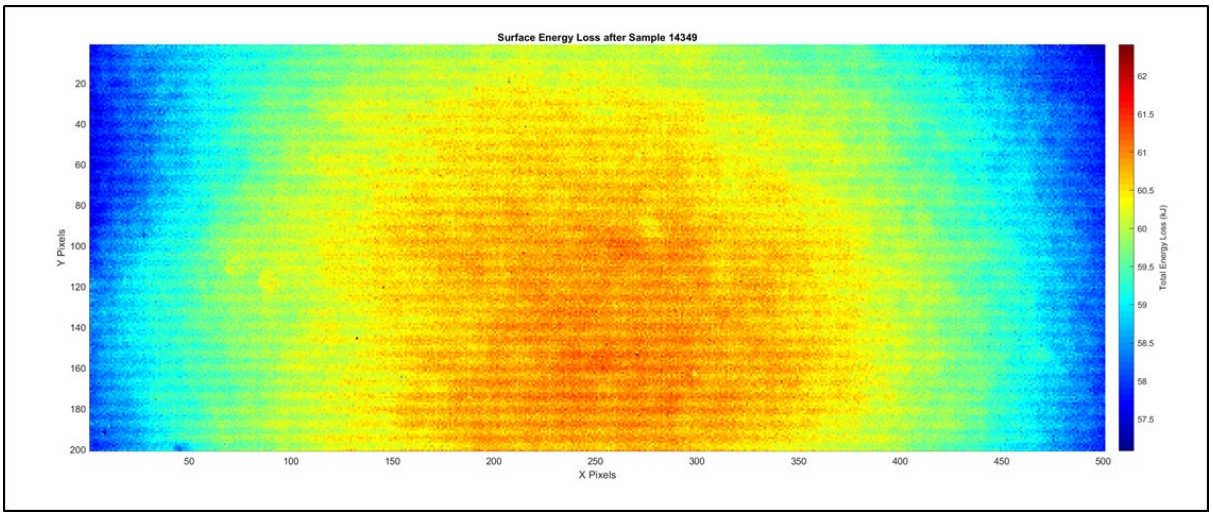

(a)

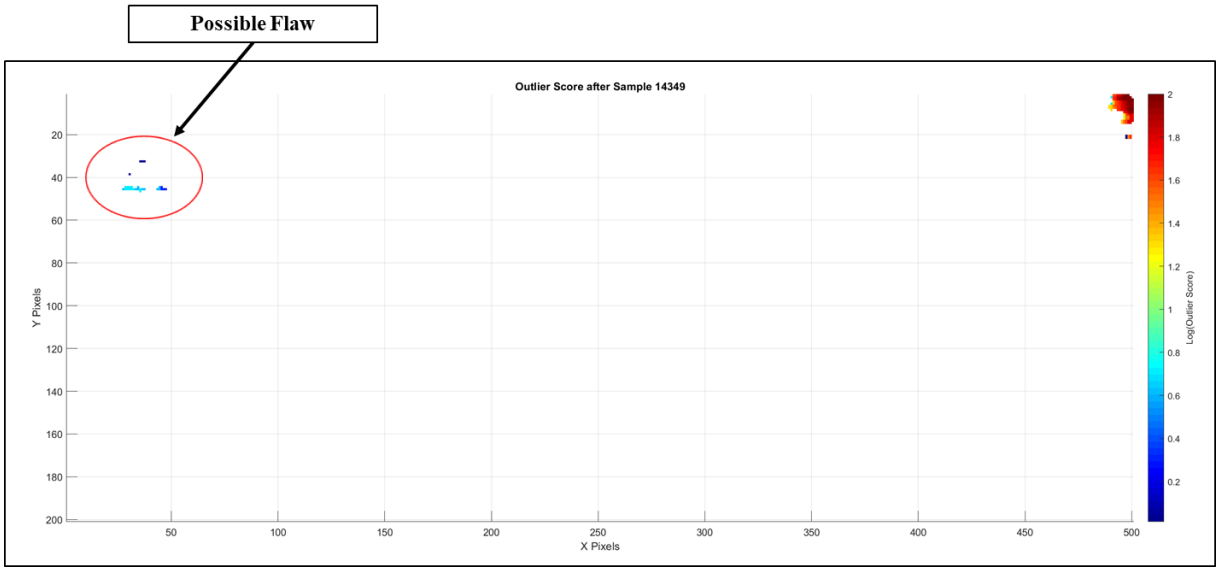

(b)

Figure 47 - a) Surface energy loss and b) outlier score for printed sample 2

Forced Air Approach

A thin slot was cut between print layers at the edge of the printed sample 2 using a slit saw to simulate an inter-bead defect. The defect size was 0.51 mm (.020 in.) thick x 76.2 mm (3 in.) wide. An air nozzle was placed behind the defect to apply high velocity shop air at the defect location in the test setup shown in the Figure 48. The shop air passes through a dryer that cools and dries the air so the air coming out of the nozzle is much cooler that that the ambient temperature in the lab. Temperature data was collected on the surface of the printed sample 2 using a FLIR A8303sc infrared (IR) camera with the shop air off and the shop air on.

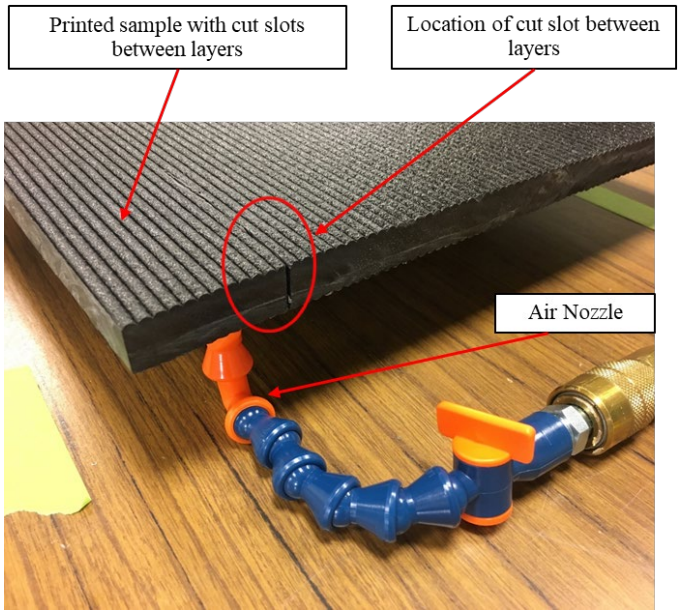

Figure 48 - NDE test setup for 3D printed test sample with high velocity shop air applied at the defect location

Figure 49 shows an IR image of printed test sample 2 at room temperature with the air flow off. The temperature of the material at the location of inter-bead defect was similar to the temperature of the surrounding material but the defect could still be observed visually. However, small defects may be more difficult to detect.

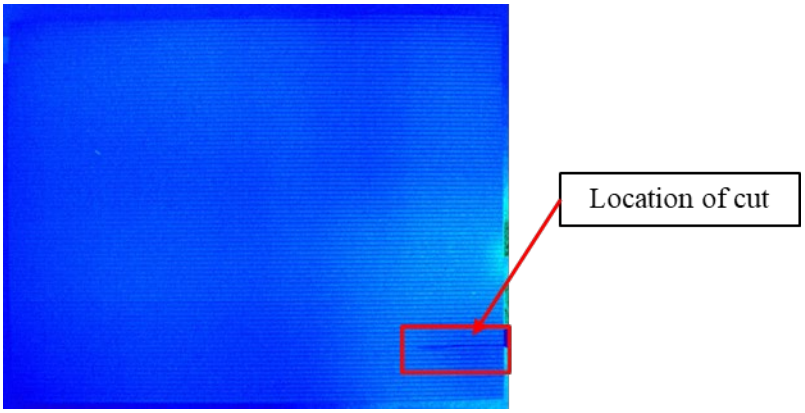

Figure 49 - IR image of a 3D printed sample with a slot cut between bead layers with air flow off

With the air flow turned on, the inter-bead defect was clearly observable in the IR image shown in Figure 50. The temperature of the high velocity air flowing through the inter-bead defect was lower compared to the surrounding material which made it much easier to observe the inter-bead defect in the IR image of printed sample 2.

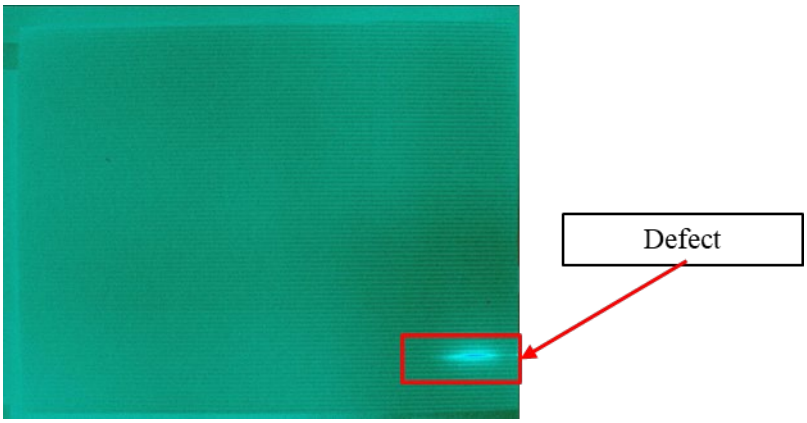

Figure 50 - IR image of a 3D printed sample with a slot cut between bead layers with shop air flow on

Local Motors provided four (4) additional printed test samples with a shim located between print layers in each test sample to further evaluate this NDE method:

- Sample 1: Shim dimension- 0.127 mm (.005 in.) thick x 28.6 mm (1.125 in.) wide
- Sample 2: Shim dimension- 0.127 mm (.005 in.) thick x 6.4 mm (0.25 in.) wide
- Sample 3: Shim dimension- 0.254 mm (.010 in.) thick x 12.7 mm (0.50 in.) wide
- Sample 4: Shim dimension- 0.127 mm (.005 in.) thick x 1.6 mm (.062 in.) wide

The shims were removed by Local Motors personnel after the prints were completed to create known inter-bead defects in each of the test samples. The location of the inter-bead defects in each of the four (4) printed test samples is shown in Figure 51.

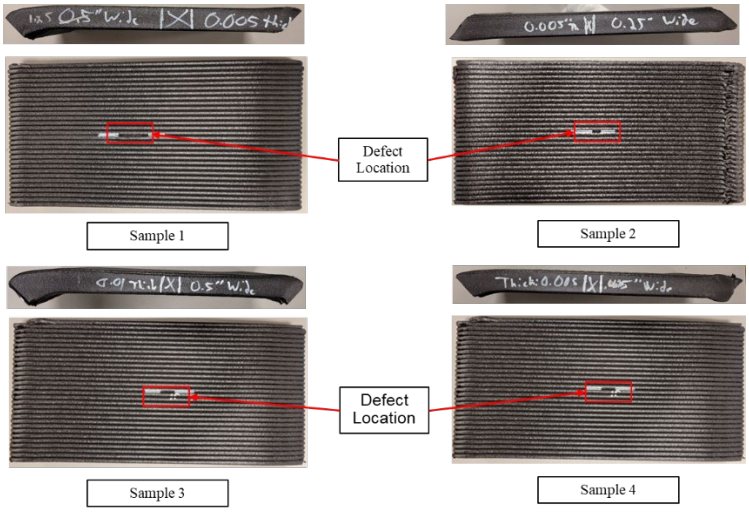

Figure 51 - Images of each of the four (4) printed test samples showing the location of defects

IR temperature data was collected on the surface of each of the (4) printed test samples with the shop air turned off and the shop air turned on. Figures 52 thru 55 show IR images of each the four (4) test samples with the shop air flow on and shop air flow off. With the shop air flow off, the defect cannot be observed visually in the IR images. When the shop air flow is turned on, the inter-bead defect can be observed in each of the four printed samples.

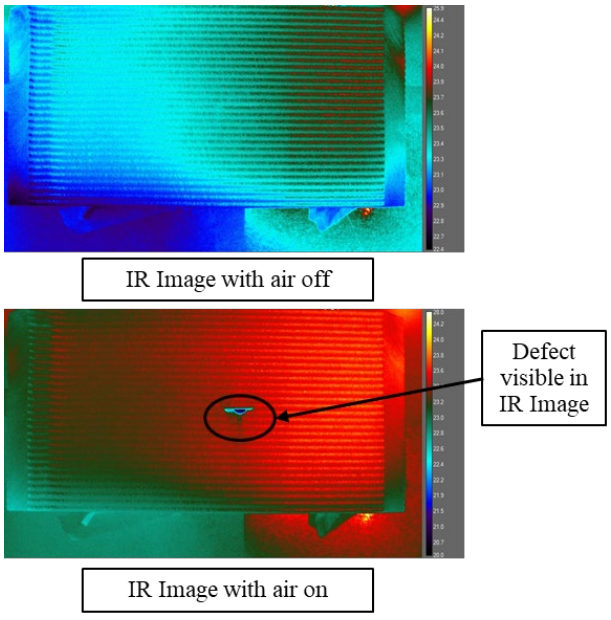

Figure 52 - IR image of a 3D printed sample 1 with shop air flow off and on

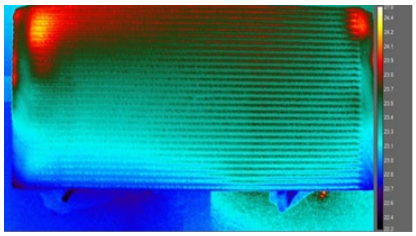

IR Image with air off

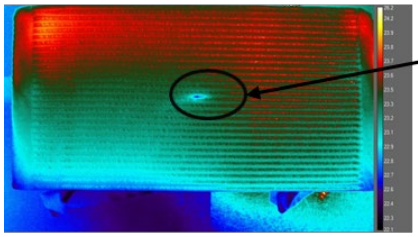

IR Image with air on

Figure 53 - IR image of a 3D printed sample 2 with shop air flow off and on

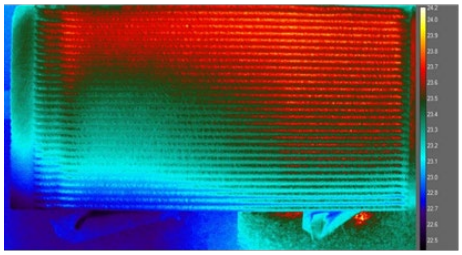

IR Image with air off

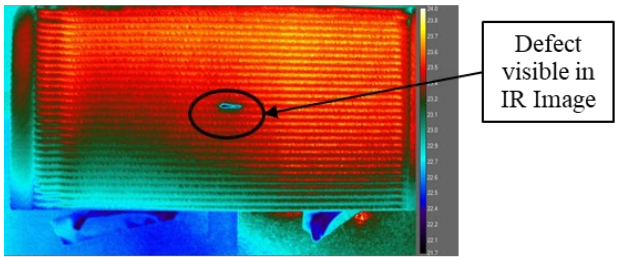

IR Image with air on

Figure 54 - IR image of a 3D printed sample 3 with shop air flow off and on

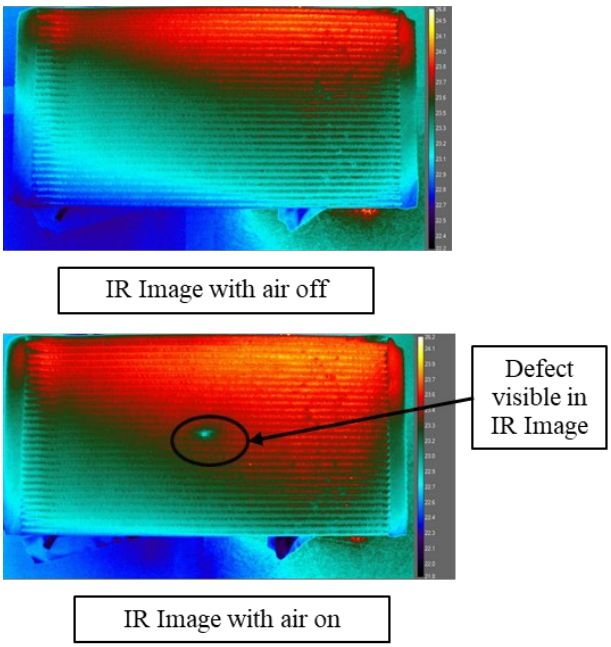

Figure 55 - IR image of a 3D printed sample 4 with shop air flow off and on

For the initial NDE testing, the air nozzle was placed directly over the defect to collect temperature data with the IR camera. The nozzle was then moved to different locations around the defect to determine how changing the location of the shop air flow effected the observability of the defect. Figures 56 thru 60 show IR images of 3D printed samples with the shop air flow on and the nozzle place at different locations around the inter-bead defect.

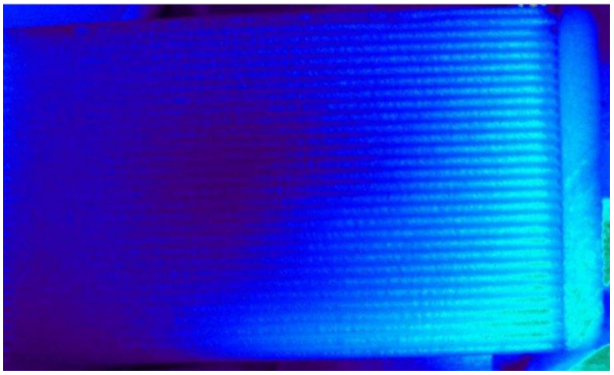

Figure 56 - IR image of 3D printed sample 3 with the nozzle located 25 mm to left of the defect and the shop air flow on (defect is not visible)

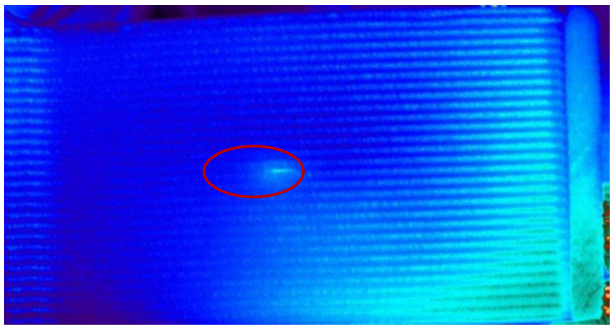

Figure 57 - IR image of 3D printed sample 3 with the nozzle located 3 mm to the left of the defect and the shop air on (defect circled in red)

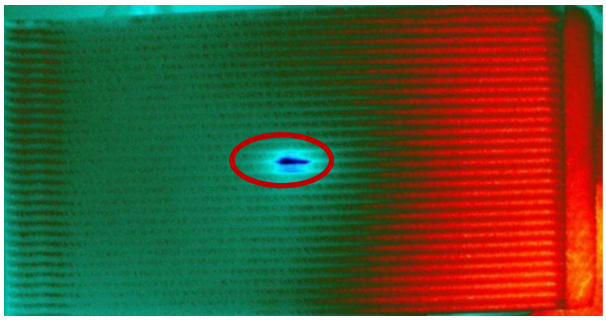

Figure 58 - IR image of 3D printed sample 3 with the nozzle located 6 mm below the defect and the shop air flow on (defect circled in red)

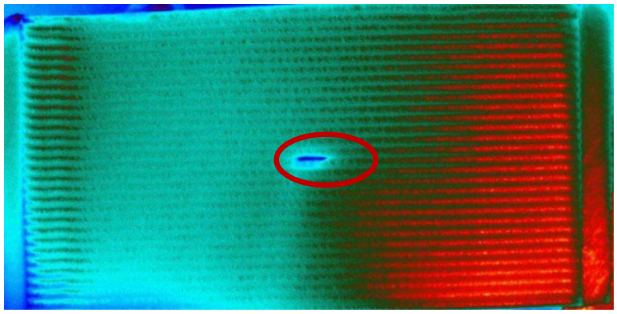

Figure 59 - IR image of 3D printed sample 3 with the nozzle located 20 mm below the defect and the shop air flow on (defect circled in red)

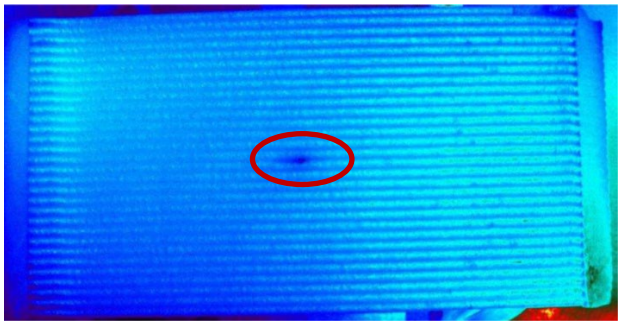

Figure 60 - IR image of 3D printed sample 3 with the nozzle located 25 mm below the defect and the shop air flow on (defect circled in red)

The inter-bead defects can be observed in the IR images of the printed test samples when the nozzle was as much a 25 mm below the defect. However, the nozzle needed to be very close to the defect when it was located to the left of the defect.

Based on the NDE results shown in the previous section, an air nozzle could be moved over the back side of a finished 3D printed part, from the top of the part to the bottom or from the bottom of the part to top, while collecting IR temperature data. Inter-bead defects that are present in the part are likely to be observable in the resulting IR images when the air flow is positioned above, below, or directly over the inter-bead defect. Data analytics could be developed to automate the detection and location of inter-bead

defects in 3D printed parts using this thermal excitation method.

This same method could also be applied as a process monitoring tool to identify inter-bead defects that occur during the 3D printing process. An air nozzle could be mounted to the deposition head of a large 3D printer, such as the Cincinnati Inc. BAAM, to apply air to the print surface. IR temperature data collected on a part during printing could potentially be processed in real-time using data analytics to automatically detect and locate inter-bead defects.

Conclusions

- An NDE system was developed that applied high velocity air to back side of 3D printed test samples near or directly over an inter-bead defect and utilized an IR camera to collect temperature data on the front surface the printed test samples to identify inter-bead defects
- Adding a passive thermal source that locally cooled the test sample greatly improved the observability of the inter-bead defects and significantly reduced the time to perform the NDE test.
- Inter-bead defects were observed in five (5) 3D printed test samples using this NDE method and the size of the smallest inter-bead defect identified was 0.127 mm x 1.6 mm.
- Based on the NDE data collected on the five (5) printed test samples with known defects in this section, milestones 3.12.1 and 3.12.2.1 were met.

In-process Monitoring

Milestone 3.12.3.1 Demonstrate in-process monitoring through the application of machine vision systems that detect bead width variation to within 5%.

The flow of the material from the extruder head in a 3D printer is controlled by process parameters such as the pump pressure and the temperature within the different zones in the extruder head, and it is parameters such as these that dictate the bead profile. There are other process parameters that provide a measure of the bead geometry as well during the deposition process. For this project, bead profile data was collected using a laser profilometer and other data available internally to the BAAM such as temperatures, pressures, pump motor torque, pump motor RPM, etc. was collected as well. The process measurement parameters were compared with bead width and bead height estimated from the laser profilometer data that was collected during each part print.

Experimental Setup and Sample Geometry

A Keyence LJ-V7200 laser profilometer, shown in Figure 61, was mounted at an offset from the print nozzle on the BAAM machine at Cincinnati, Inc.

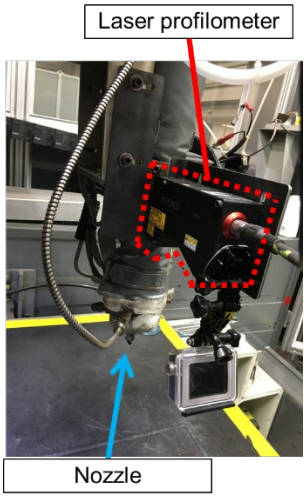

Figure 61 - Profilometer mounted on the print nozzle of the BAAM

The laser profilometer has 600 evenly spaced laser beams located across the head in the horizontal direction are projected onto the BAAM table, as shown in Figure 62e, that proved a measurement resolution of 0.1 mm in the horizontal direction (i.e., across the bead). Each of the 600 laser beams measures the vertical distance to the measurement surface with a continuous resolution that can measure as low as to 0.001 mm in the vertical direction (i.e., bead height). Depending on the print direction, the line of beams projected by the profilometer were either behind, in front of, or adjacent to the bead being printed as show in Figures 62 a, b, c and d). The profilometer was always oriented in the same direction regardless of the print direction.

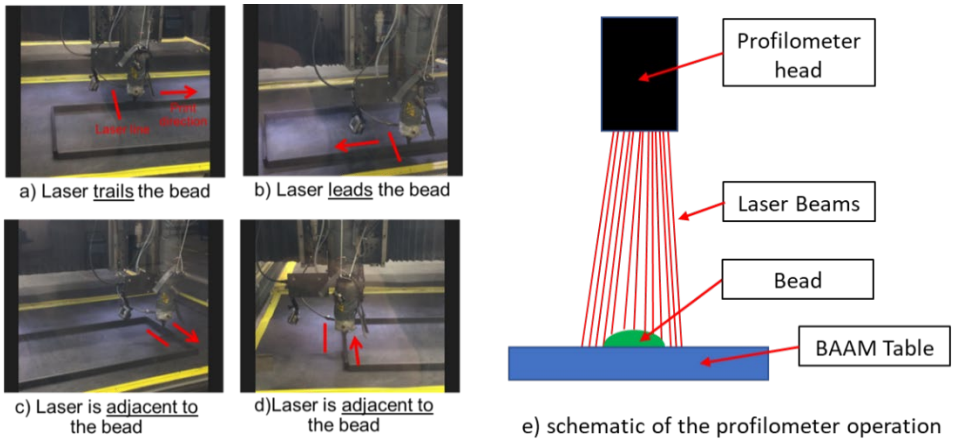

Figure 62 - Profilometer was located either a) behind, b) in front of, or c) and d) adjacent to the bead being printed (no profile data collected)

Figures 63 and 64 show the two types of parts that were printed on the BAAM for testing: Rectangular and Zigzag

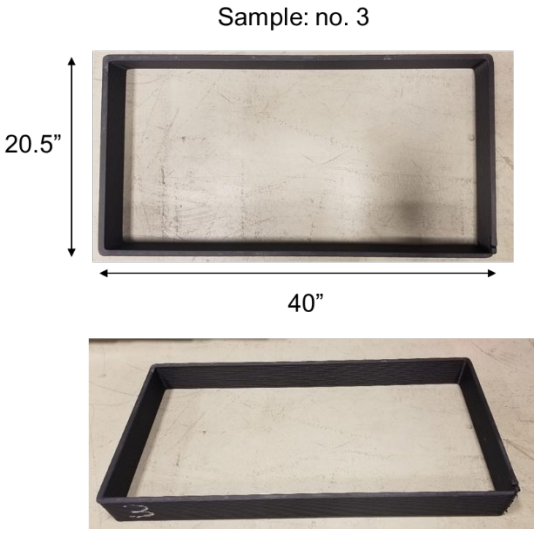

Figure 63 - Rectangular printed part

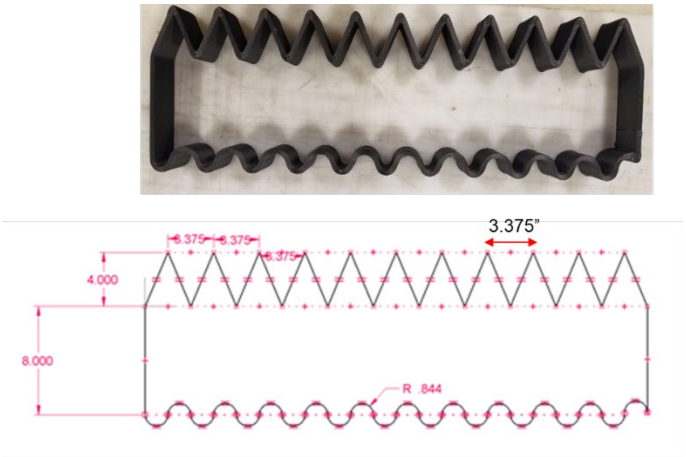

Figure 64 - Zigzag printed part

The rectangular parts had a programmed print size of 508 mm x 1016 mm (20”x40”) with 19 print layers. The zigzag parts had a programmed print size of 326.2 mm x 943 mm (12.84”x 37.13”) with 20 print layers. For each print layer, two sets of data were acquired as illustrated in Figure 65: “Real-time” data and “One-layer delay” data

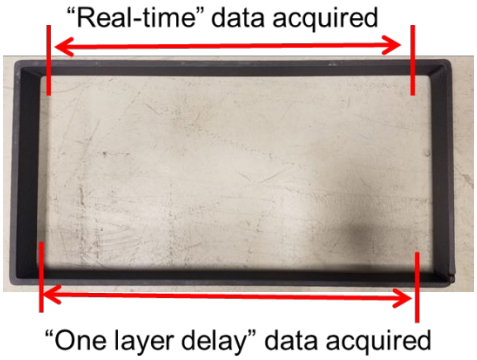

Figure 65 - Two sets of data were acquired for each print layer: “Real-time” data and “One-layer delay” data

For each data set 50 or 100 profiles were acquired every second. The number of profiles per data set depended on the feed rate, given in inches per minute (IPM), and 18-20 data sets were acquired per print. In all cases, 19 or 20 layers were printed, but in some cases memory limitations prevented data acquisition from the final few layers.

During the straight-line prints, data was acquired for two test cases for the rectangular parts:

- 5.1 mm (0.2”) layer height using a 10.2 mm (0.4”) nozzle with a bead width ~12.7 mm (0.5”)
- 3.8 mm (0.15”) layer height using a 7.6 mm (0.3”) nozzle with a bead width ~ 10.2 mm (0.4”)

For each test case, seven rectangular parts were printed with each part having different feed rates (IPM) and extruder rotation speeds, rotations per minute (RPM). The feed rate (IPM) and the extruder rotation speed (RPM) were scaled by the following seven parameter scales for testing: 16%, 30%, 43%, 64%, 100%, 133% and 150%. By scaling the magnitude of feed rate (IPM) and extruder rotation speed (RPM) values used the 100 % parameter scale equally, it was anticipated that the bead width would remain constant for each bead printed for a specific part shape and nozzle size combination. The parameter scale percentages were chosen to span the operating range of the BAAM printer and the 100% parameter scale was considered to be normal operating conditions for the BAAM. The print variables used for the BAAM to 3D print the box and zigzag shaped parts for testing are shown in Table 11.

Table 11 - Print variables used for the BAAM to 3D print the box and zigzag shaped parts for testing

Part Shape	Nozzle Size (mm)	Estimated Layer height (mm)	Estimated Layer Width (mm)	Paramter Scale (%)	Extruder Rotation Speed (RPM)	Material Feed Rate (IPM)
Box	10.2	5.1	12.7	16	40.8	46.8
Box	10.2	5.1	12.7	30	76.5	87.8
Box	10.2	5.1	12.7	43	109.7	125.8
Box	10.2	5.1	12.7	64	163.2	187.2
Box	10.2	5.1	12.7	100	255.0	292.5
Box	10.2	5.1	12.7	133	339.2	389.0
Box	10.2	5.1	12.7	150	382.5	438.8
Box	7.6	3.8	10.2	16	38.4	78.4
Box	7.6	3.8	10.2	30	72.0	147.0
Box	7.6	3.8	10.2	43	103.2	210.7
Box	7.6	3.8	10.2	64	153.6	313.6
Box	7.6	3.8	10.2	100	240.0	490.0
Box	7.6	3.8	10.2	133	319.2	651.7
Box	7.6	3.8	10.2	150	360.0	735.0
Zigzag	7.6	3.8	9.5	16	38.4	78.4
Zigzag	7.6	3.8	9.5	43	72.0	147.0
Zigzag	7.6	3.8	9.5	100	240.0	490.0

During the zig zag prints, data was acquired for a single test case:

- 3.8 mm (0.15”) layer height using a 7.6 mm (0.3”) nozzle with a bead width ~ 9.5 mm (0.375”)

Like for the rectangular prints, a series of zig zag prints were made using different IPM and RPM parameter values. Only three parameter scales were used to print three zig zag parts: 16%, 43%, 100%. A print using a parameter scale of 150% percent was aborted due to chatter in the print head as it printed the curved edge of the parts. The print variables used to 3D print the zigzag parts for testing are shown in Table 11.

In addition to profilometer data, process parameters from the printer were synchronously recorded including print head position (x, y, and z); table position; temperature measurements along the barrel, near the tip, at the motor, at the inlet, and at the table surface; feed rate; head speed; and extruder speed, pressure, and torque. Position parameters were used in the bead width and height analysis. As described later, temperature, pressure, and torque measurements were analyzed to determine effect, if any, on bead height and width estimates.

Rectangular Prints

The profilometer acquires the profiles of the bead at the chosen sampling rate as shown in Figure 66. The profilometer projects 600 laser beams across approximately 63.5 mm (2.5”). Regardless of the distance from the profilometer, profiles are always recorded with an equal resolution of 100 µm (0.004”).

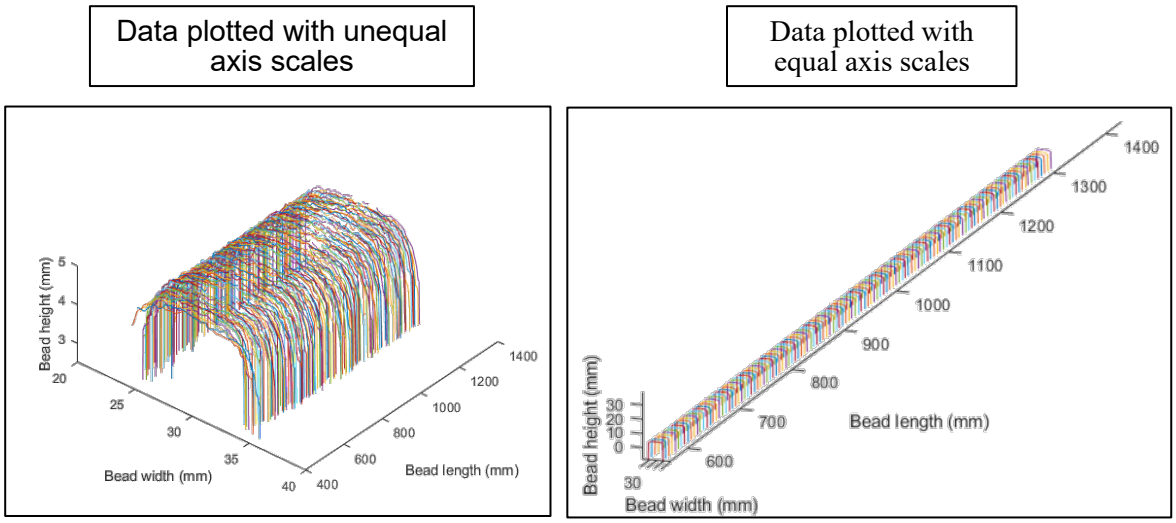

Figure 66 - Plots of profilometer the profiles of the bead at the chosen sampling rate

Figure 67 shows a plots of an individual bead profile. The edges of the bead were taken as the first and last points whose y values (i.e., bead height) were greater than 2mm. The 2 mm threshold was effective in choosing points just before significant drop-off as shown in each layer.

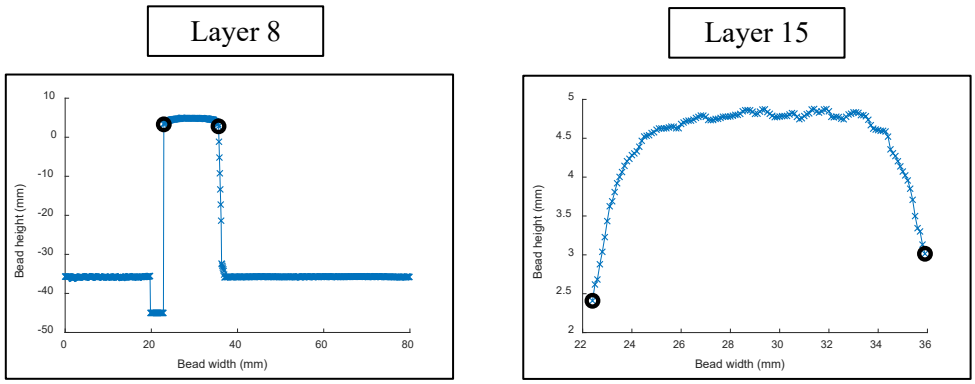

(a) *(b)*

Figure 67 - Plots of individual bead profiles at a) layer 8 and b) layer 15

The profilometer was always the same distance above the print nozzle and the table was farther away from the profilometer for each successive layer. Figure 68 shows the bead widths for each profile identified for each layer. After layer 21, the table drops outside of the measurement range of the laser.

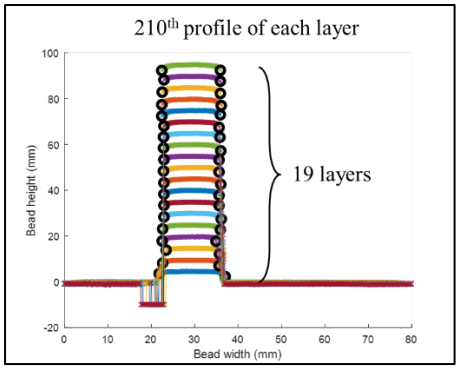

The bead heights were manually adjusted to show the heights relative to the table surface.

Figure 68 - Bead widths of each profile for each layer that were identified

The profilometer was mounted off-center relative to the center line of the print nozzle (see Figure 69). This alignment caused a "dead zone" or a blind spot in the profile data. This occurs when a portion of the line of lasers is blocked by the target as illustrated in Figure 70.

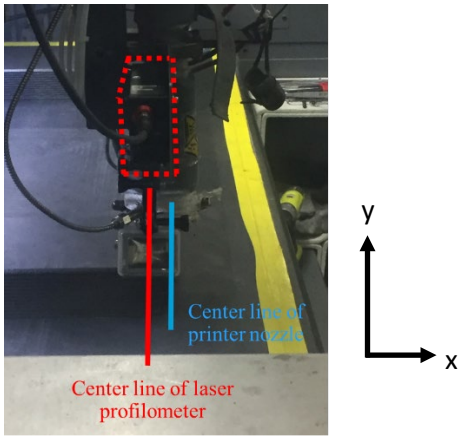

Figure 69 - Profilometer mounted off-center relative to the center line of the print nozzle on the BAAM

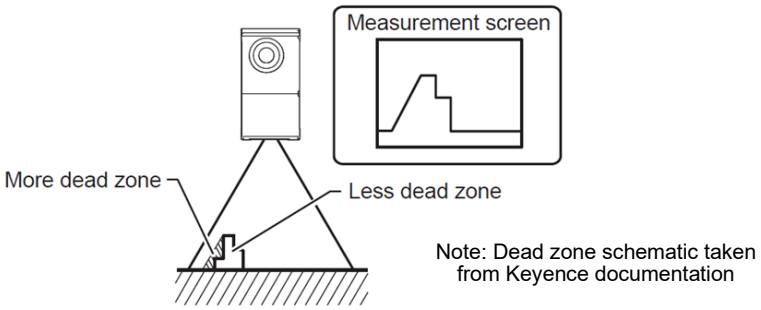

Figure 70 - "Dead zone" or a blind spot in the profile data occurs when a portion of the line of lasers is blocked by the target

The dead zone is smallest near the center of the x-axis of the measurement range. The distance between each laser measurement point is 100 µm (~.004 in). The data collected suggests that dead zones points correlated to points along the edge of the bead, so the dead zones did not significantly affect the bead width measurement.

A statistical analysis of the bead width estimates was performed to see if there were any trends in the layers

of each part printed using the parameter scales described in the experimental setup and sample geometry section. Box and whisker plots were calculated for the bead width estimate distributions for each of the rectangular parts and will be displayed as follows:

- Red line: median
- Top of box: 75th percentile
- Bottom of box: 25th percentile
- Whiskers extend to ~2.7 σ
- "+": Outliers

Approximately 99% of the profile data collected was non-outlier data. Figures 71 thru 77 show box and whisker plots of estimated bead width vs. print layer for all 7 of the parameter scales for the printed rectangular parts using the 10.2 mm (0.4") nozzle.

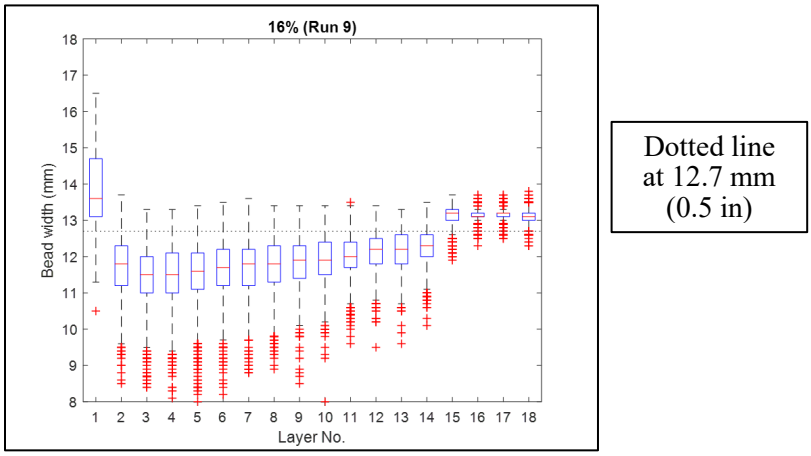

Figure 71 - Estimated bead width vs. print layer for the 16% parameter scale for a printed rectangular part using the 10.2 mm (0.4") nozzle

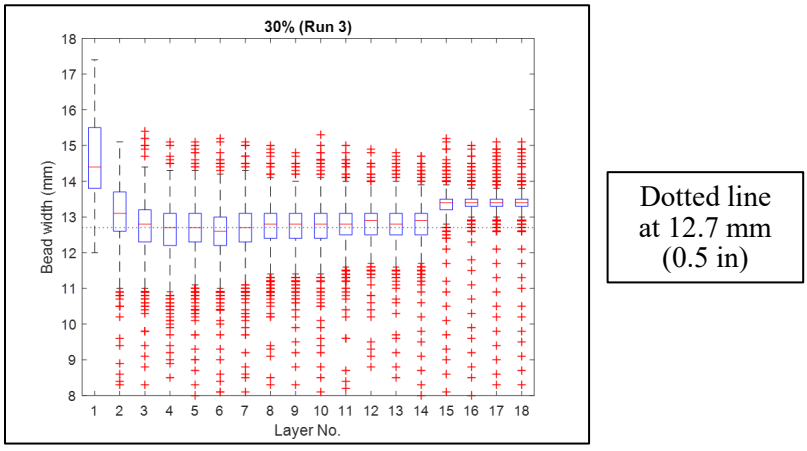

Figure 72 - Estimated bead width vs. print layer for the 30% parameter scale for a printed rectangular part using the 10.2 mm (0.4") nozzle

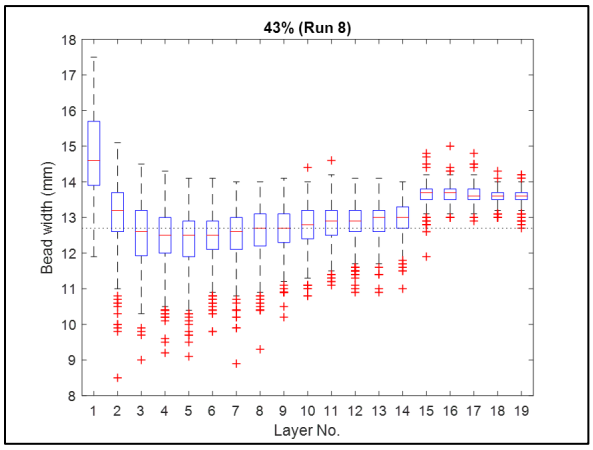

Figure 73 - Estimated bead width vs. print layer for the 43% parameter scale for the printed rectangular parts using the 10.2 mm (0.4") nozzle

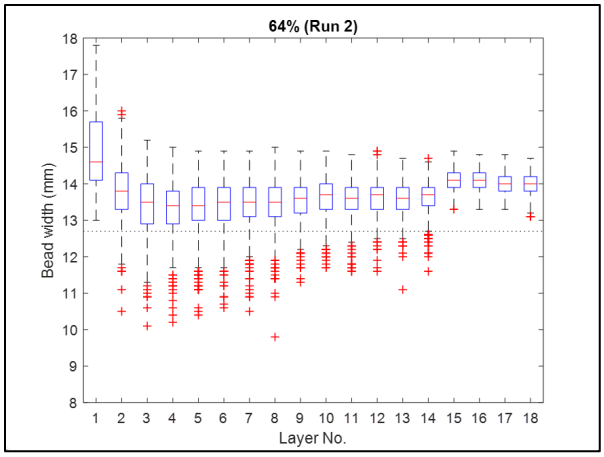

Figure 74 - Estimated bead width vs. print layer for the 64% parameter scale for a printed rectangular part using the 10.2 mm (0.4") nozzle

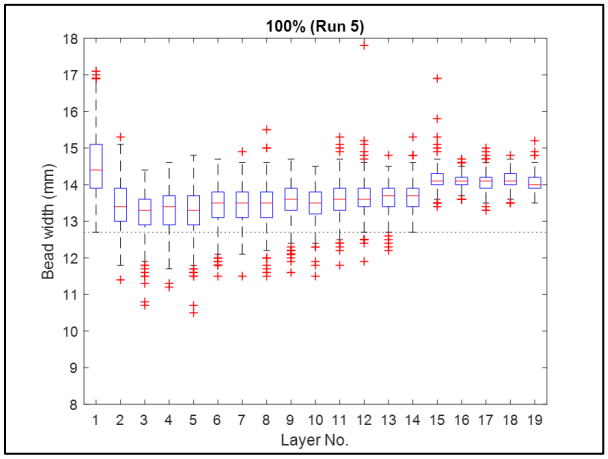

Figure 75 - Estimated bead width vs. print layer for the 100% parameter scale for a printed rectangular part using the 10.2 mm (0.4") nozzle

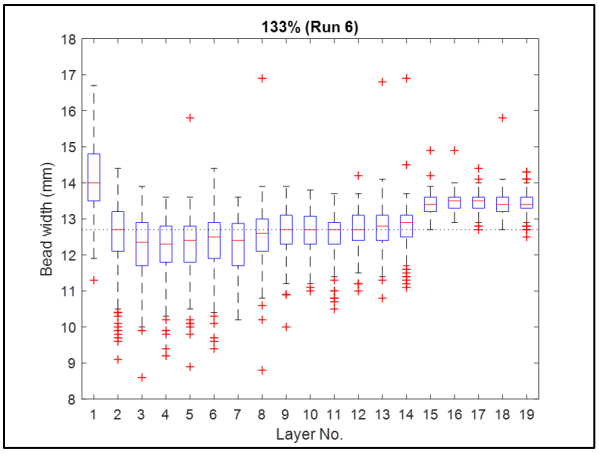

Figure 76 - Estimated bead width vs. print layer for the 133% parameter scale for a printed rectangular part using the 10.2 mm (0.4") nozzle

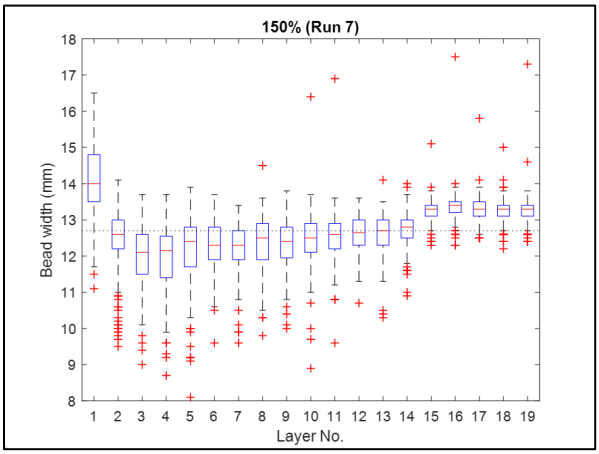

Figure 77 - Estimated bead width vs. print layer for the 150% parameter scale for a printed rectangular part using the 10.2 mm (0.4") nozzle

Figures 78 thru 84 are box and whisker plots of estimated bead width vs. print layer for all 7 parameter scales discussed above for printed rectangular parts using the 7.6 mm (0.3") nozzle.

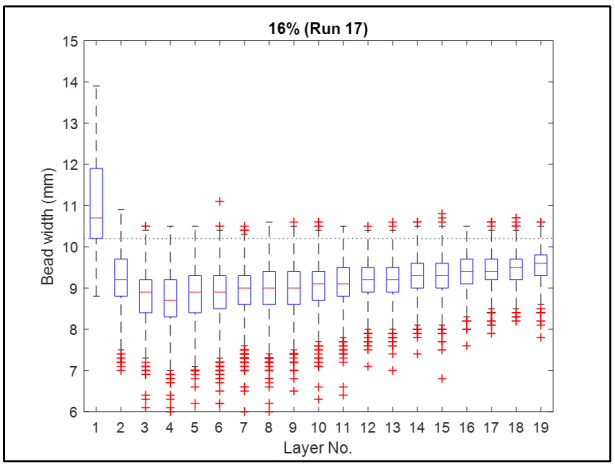

Figure 78 - Estimated bead width vs. print layer for the 16% parameter scale for a printed rectangular part using the 7.6 mm

(0.3") nozzle

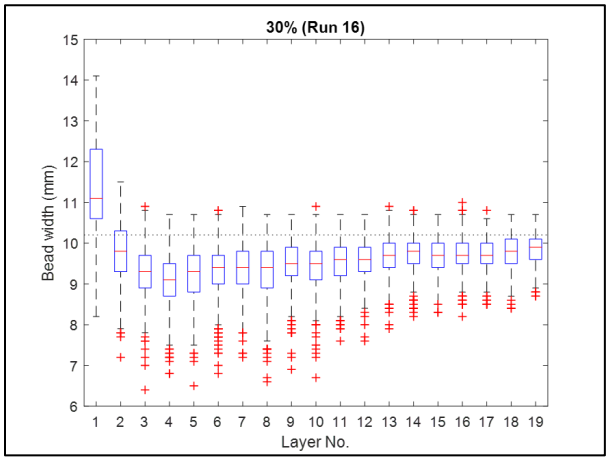

Figure 79 - Estimated bead width vs. print layer for the 30% parameter scale for a printed rectangular part using the 7.6 mm (0.3") nozzle

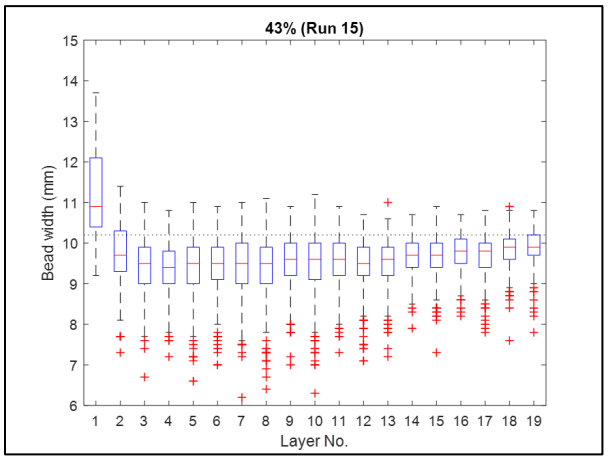

Figure 80 - Estimated bead width vs. print layer for the 43% parameter scale for a printed rectangular part using the 7.6 mm (0.3") nozzle

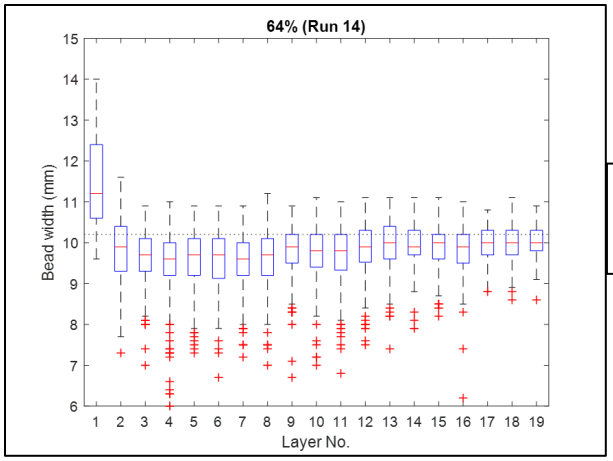

Figure 81 - Estimated bead width vs. print layer for the 64% parameter scale for a printed rectangular part using the 7.6 mm (0.3") nozzle

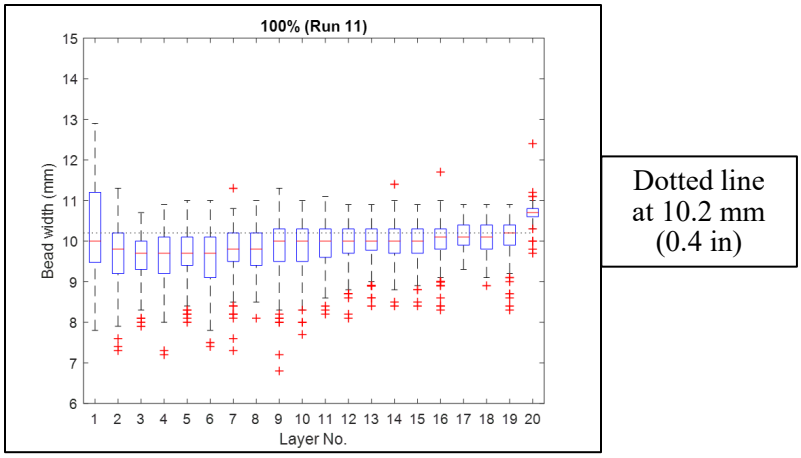

Figure 82 - Estimated bead width vs. print layer for the 100% parameter scale for a printed rectangular part using the 7.6 mm (0.3") nozzle

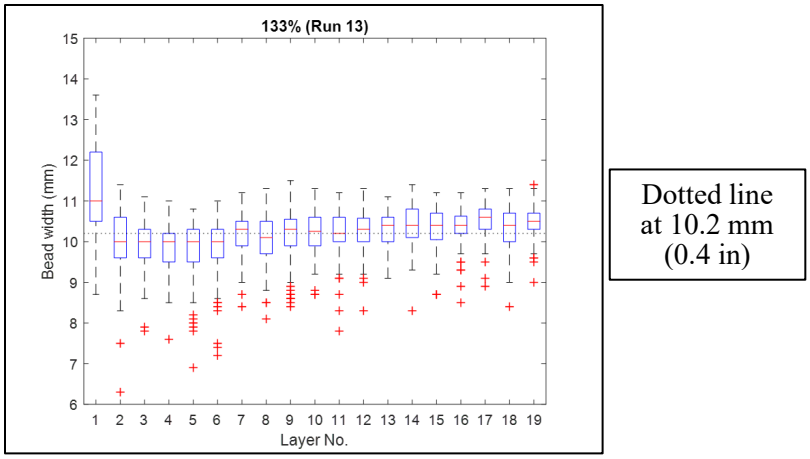

Figure 83 - Estimated bead width vs. print layer for the 133% parameter scale for a printed rectangular part using the 7.6 mm (0.3") nozzle

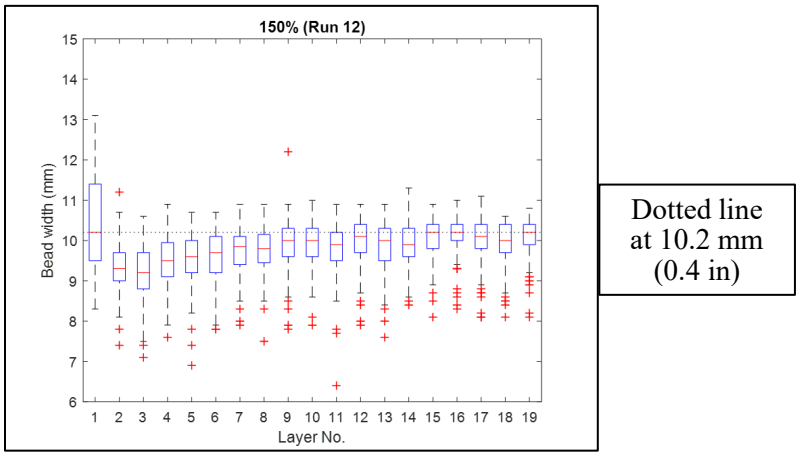

Figure 84 - Estimated bead width vs. print layer for the 150% parameter scale for a printed rectangular part using the 7.6 mm (0.3") nozzle

The first layer showed a consistently higher median and a larger spread for the rectangular part for both

nozzles. The last few layers (after table drops out of measurement range) consistently showed a higher median and smaller spread as well.

A statistical analysis of all of the bead width results was performed for each of the seven rectangular parts printed with the 10.2 mm (0.4") nozzle. For each print, all estimated widths from all layers were combined. The number of data points analyzed for each parameter scale is shown in Table 12.

Table 12: Number of bead width points at each parameter scale used for statistical analysis

Data Set	# of data points	
16%	40,103	Data acquired at 100 Hz
30%*	45,000	
43%	15,860	Data acquired at 50 Hz
64%	19,762	
100%	6,752	
133%	5,057	
150%	4,446	

Figure 85 shows the results of statistical analysis performed on of all of the bead widths for each of the rectangular parts for the seven parameter scales using box and whisker plots.

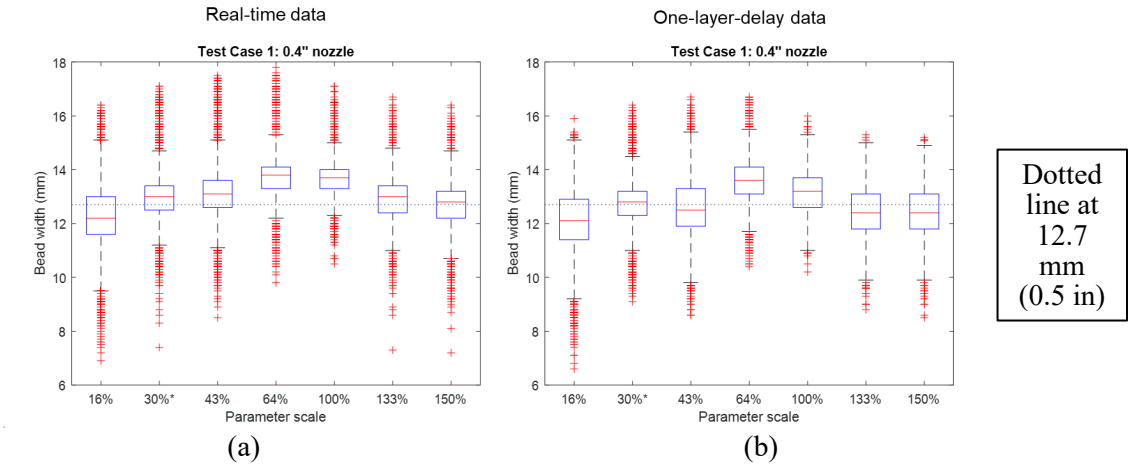

Figure 85 - All of the bead widths combined vs the seven parameter scales for the a) real-time data and b) one-layer delay data

A statistical analysis was performed using all of bead width results in each rectangular part printed with the 7.6 mm (0.3") nozzle at each of the seven parameters. The number of data points analyzed for each parameter scale is shown in Table 13.

Table 13 - Number of bead width points at each parameter scale used for statistical analysis

Data Set	**# Of data points**
16%	25,470

30%	13,374
43%	9,342
64%	6,213
100%	4,133
133%	2,861
150%	2,700

All data acquired at 50 Hz

Figure 86 shows box and whisker plots of all of the estimated bead widths in the rectangular part printed with the 7.6 mm (0.3") nozzle for each of the seven parameter scales.

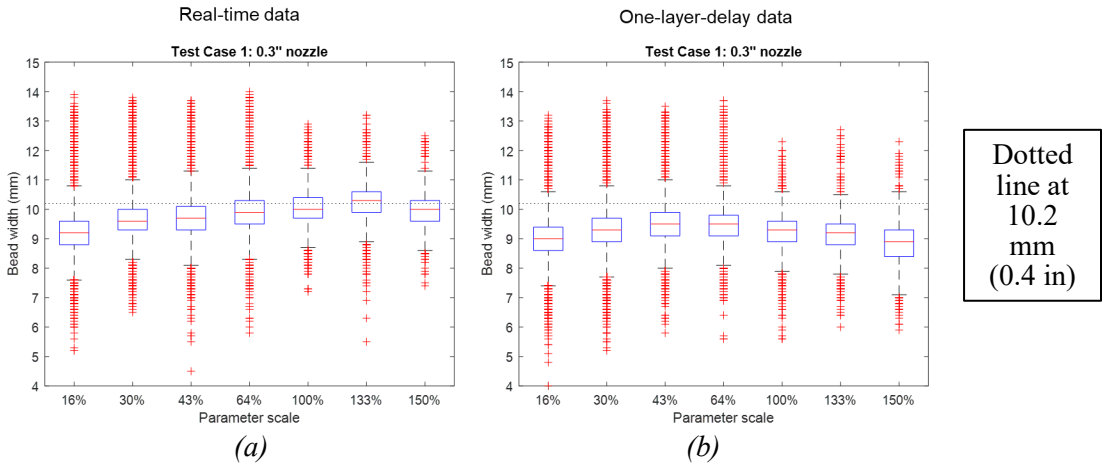

Figure 86 - Estimated bead width in the printed rectangular parts vs the seven parameter scales for the a) real-time data and b) one-layer delay data

The bead width of the first layer was consistently wider likely due to the material spreading as it adhered to the table. In Figures 87 and 88, the data for the first layer was removed and the box and whiskers plots were recalculated to provide a better estimate of the mean and standard deviation of the bead width.

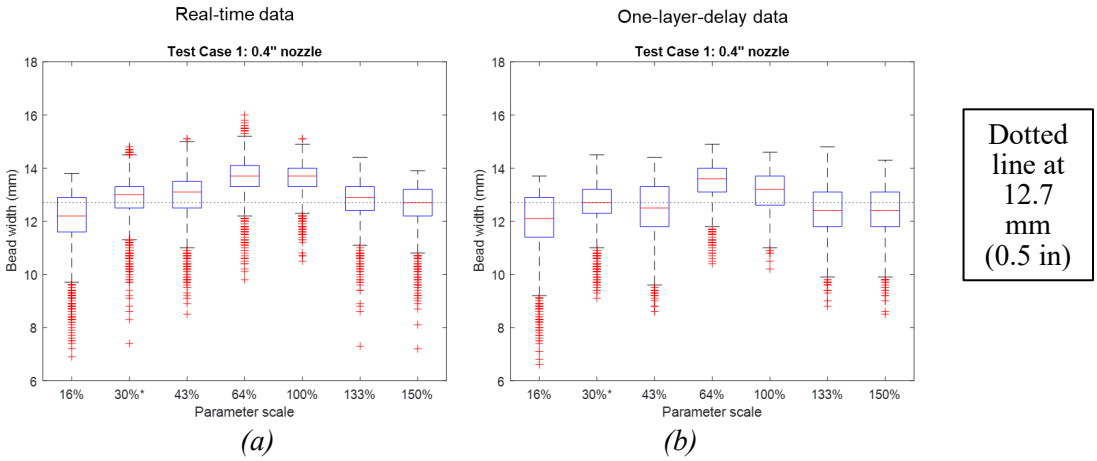

Figure 87 - Estimated bead widths in the printed rectangular parts vs the seven parameter scales with the data for the first layer removed for the a) real-time data and b) one-layer delay data

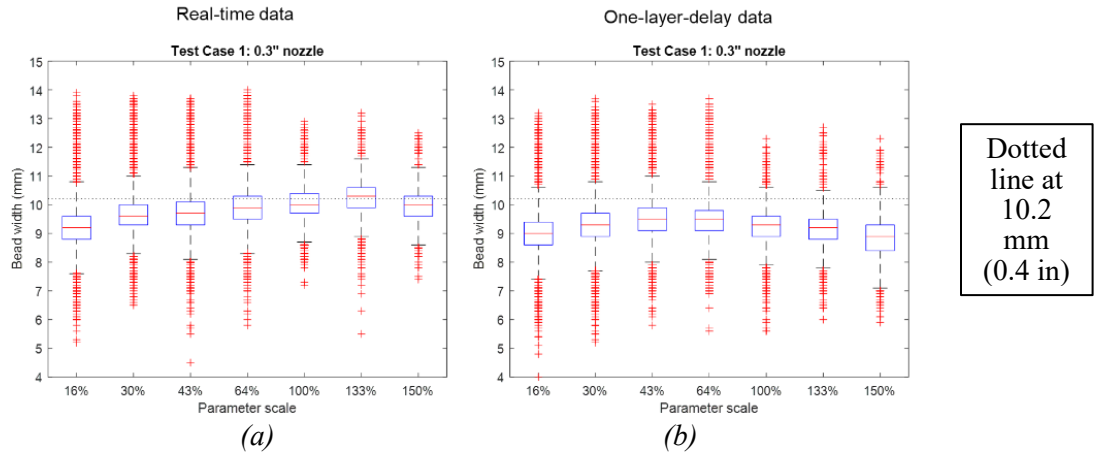

Figure 88 - Estimated bead widths in the printed rectangular parts vs the seven parameter scales with the data for the first layer removed for the a) real-time data and b) one-layer delay data

Table 14 summarizes the mean bead width of the real-time and one-layer delay data.

Table 14 - Summary the mean bead width of the real-time and one-layer delay data

		Bead width (mm)		
	Parameter scale (%)	Real-time	One-layer-delay	% change
0.4" nozzle	16	12.2	12.1	-0.8
	30	13.0	12.7	-2.3
	43	13.1	12.5	-4.6
	64	13.7	13.6	-0.7
	100	13.7	13.2	-3.6
	133	12.9	12.4	-3.9
	150	12.7	12.4	-2.4
0.3" nozzle	16	9.2	9.0	-2.2
	30	9.6	9.3	-3.1
	43	9.6	9.5	-1.0
	64	9.9	9.5	-4.0
	100	10.0	9.3	-7.0
	133	10.3	9.2	-10.7
	150	10.0	8.9	-11.0

Most of the outliers show in Figure 71 occurred below the median. Many of the outliers are the type of "unusual" profile measurements shown in Figure 89.

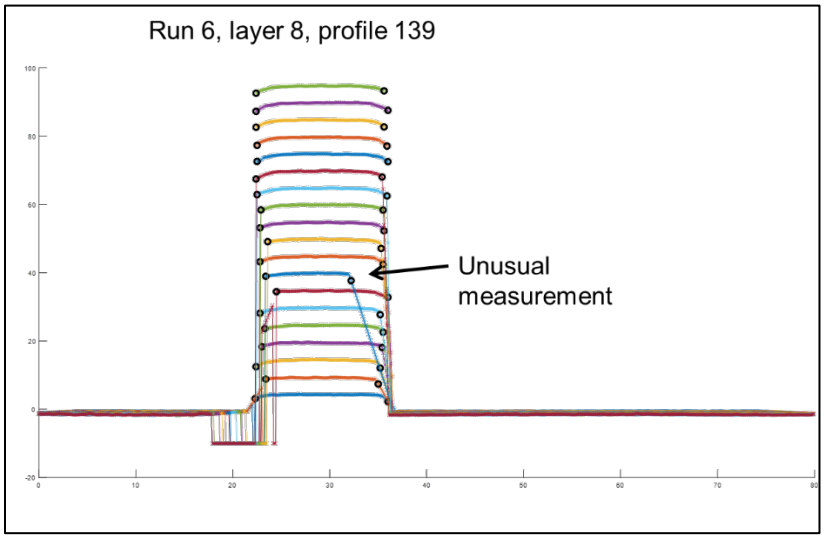

Figure 89 - Plot showing an "unusual" profile measurement

Bead Width Conclusions

- With the profilometer system in the print environment, the profilometer moving with the deposition head and vibration was present, the profilometer system was capable of capturing the bead width variation along the length of the bead and from layer to layer during a print.
- The bead width for the one-layer delay data was always less than the real-time data. This was expected because the bead had cooled and contracted by the time the measurement was made.
- The bead width varies based on the parameter scale used for printing the part

- Knowing the variation in the mean bead width and the variation in the bead width around the mean for a broad range of print variables, adjustments could be made to the slicing software to create a print model that would reduce part variation and minimize the probability of a gaps occurring between beads printed next to each other during the printing.

Bead height results

Figure 90 shows the raw profiles for 19 material layers and shows the table surface of the BAAM as well.

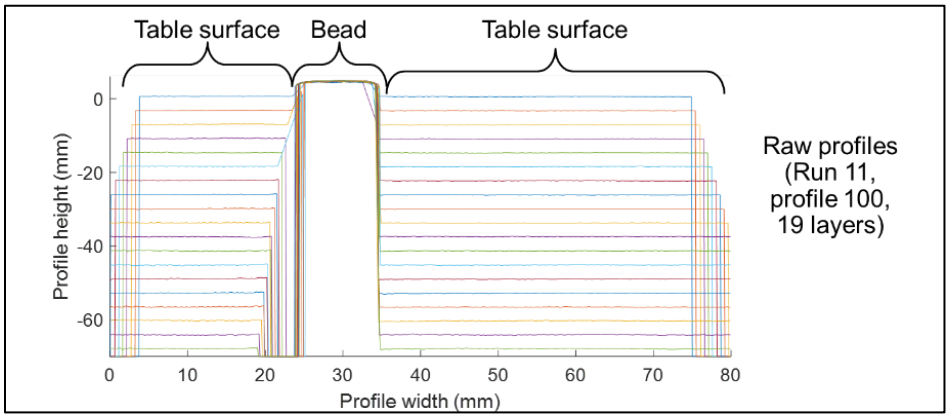

Figure 90 - Raw profiles for 19 material layers that includes the beads and the table surface of the BAAM

The profile height, h, shown in Figure 91a was measured relative to the laser profilometer's internally defined axes and h=0 is at the center (vertically) of the measurement volume. The measured profile height in the bead region must be converted to bead height, as shown in Figure 91b. Deposition head location data was accessed from the BAAM which allowed us to track of the location of the sampled profiles in each print layer. Knowing the position of the profiles in each layer, we were able to use the table profile and profiles of previous layers to account for the variability in each layer when we estimated the current bead height for each profile to get to the "true" bead height variability. After each layer is printed, the table surface always moves down the same distance. If the previous bead was shorter/taller than expected the distance from the laser to the print surface will be different than the distance the table moved. Therefore, the height of previous layers must be taken into account when estimating the height of the current layer. To estimate the actual bead height, the measured profile height in the bead region was identified first. To accomplish this, the largest 50 points in a bead profile were identified as shown in Figure 91. Profile height was estimated using the mean of the top 50 points. If there were only N (N<50) points within 3mm of the peak, only N points were used to find the mean.

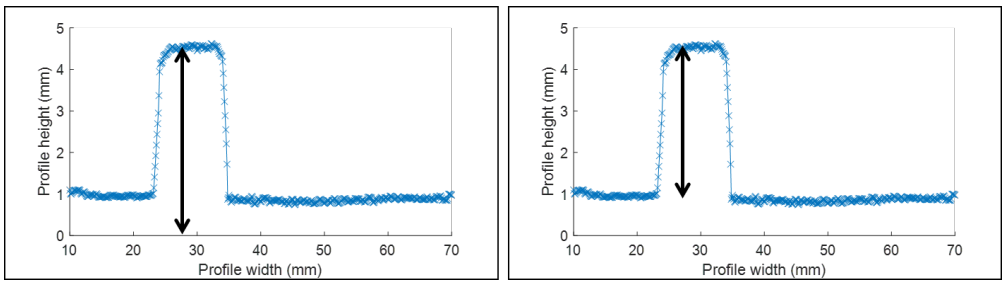

(a) (b)

Figure 91 - a) bead profile height and b) bead height

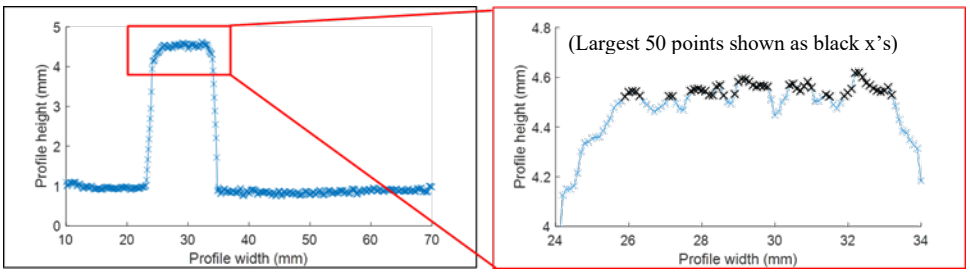

Figure 92 - Largest 50 points in a bead profile identified

The process to convert the measured bead profile height to actual bead height is illustrated in Figure 93. h_M is the average measured height and h_{TABLE} is the average height of the table surface estimated from the measured data. If the table surface is outside the measurement volume, the table position is taken from the data collected internally on the BAAM during the print. The total part height is found by subtracting hTABLE from h_M (hM – hTABLE) and then the height(s) of the previous layer(s) are subtracted off.

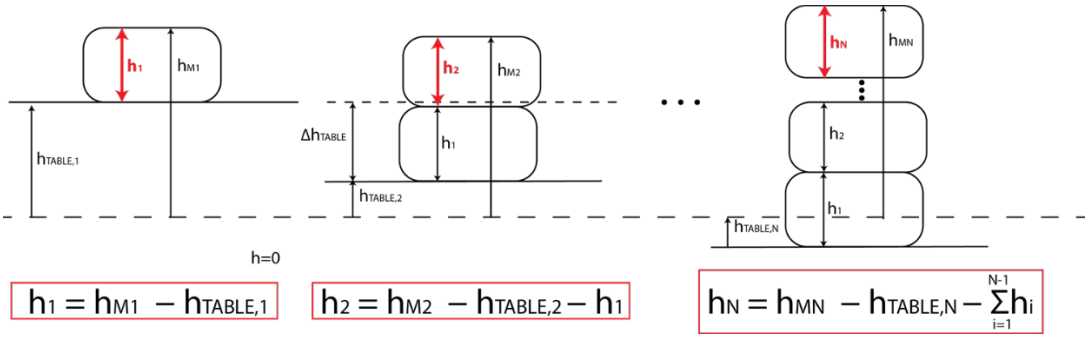

Figure 93 - Bead profile height was then converted to bead height

Figures 94 and 95 show a statistical analysis of the estimated bead heights for 19 layers using the 10.2 mm (0.4") nozzle for the 100% and 43 %parameter scales respectively. In each case, the first layer was shorter than the next few. Recall that the first layer was also wider than subsequent layers. In most cases, layers 3 and 4 are taller than expected which is likely compensation for the shorter than expected layers 1 and 2. In all cases, the spread in the data was greatest for the first layer.

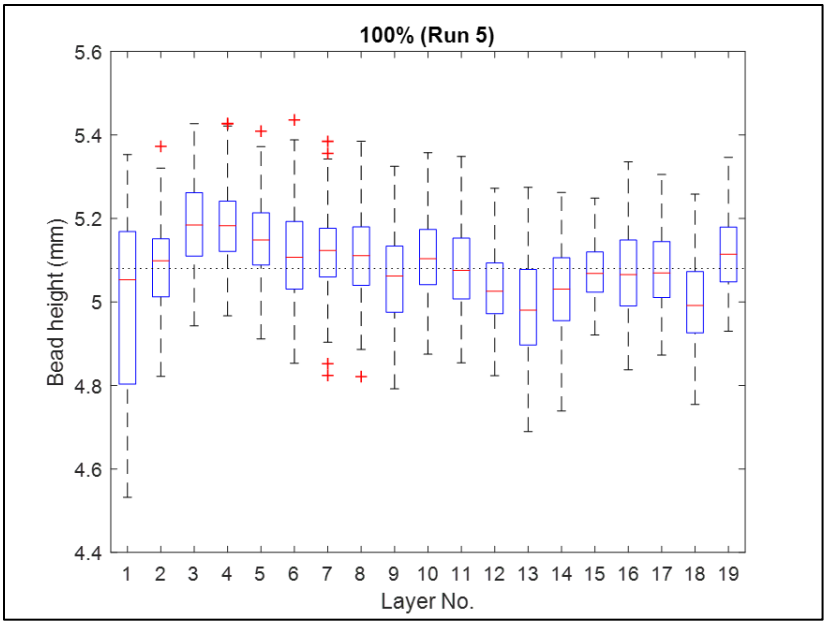

Note: After layer 14, estimated table height was used because table was outside the measurement range of the lasers

Figure 94 - Statistical analysis of the estimated bead heights for 19 layers of a rectangular part for the 100% parameter scale

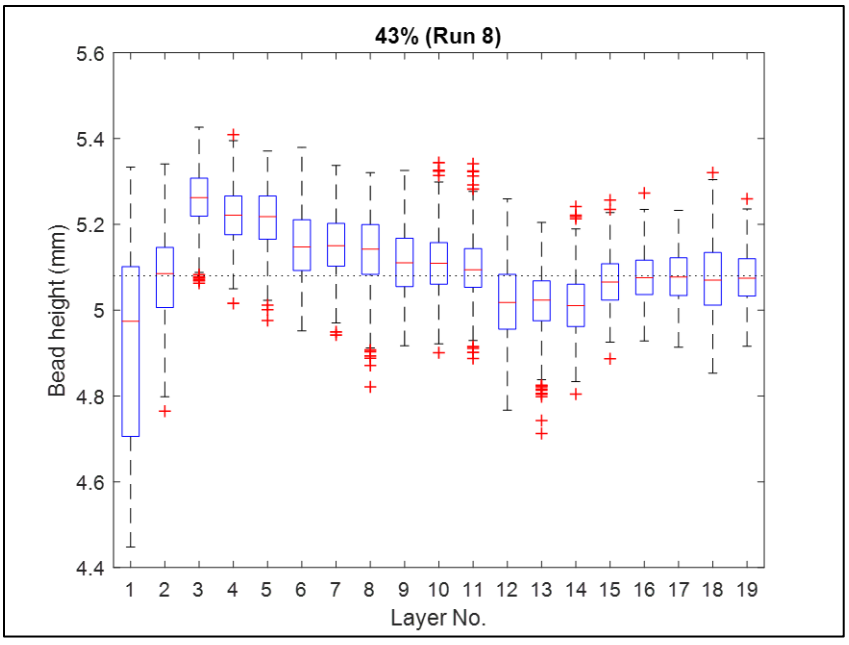

Figure 95 - Statistical analysis of the estimated bead heights for 19 layers of a rectangular part for the 43% parameter scale

A similar trend was evident in the 7.6 mm (0.3") nozzle bead height data for the 100% and 43% parameter scales shown in Figures 96 and 97 respectively. The first layer was generally shorter than the next few and the second and/or third layers tended to compensate for the height of the first layer. The first layer had the greatest spread in the data. The measured table height was available for all layers.

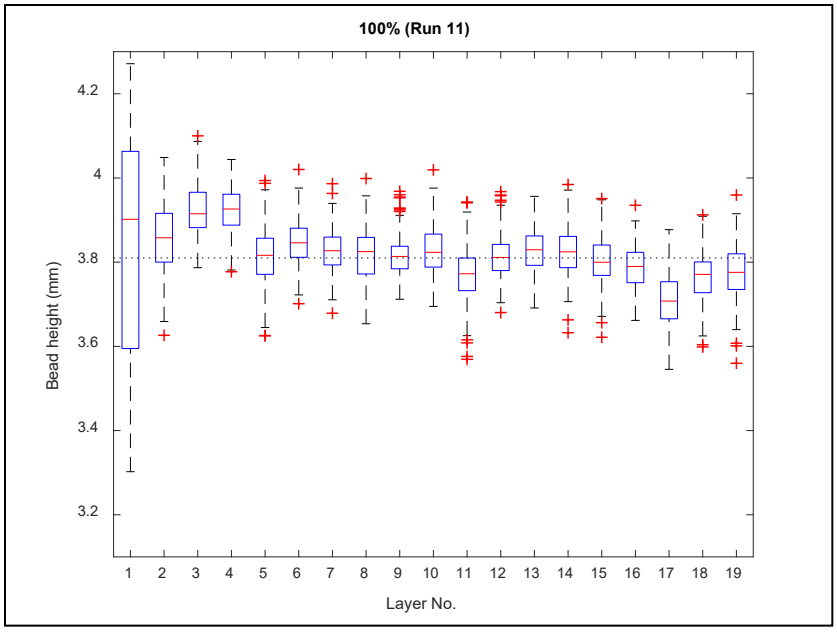

Figure 96 - Statistical analysis of the estimated bead heights for 19 layers of a rectangular part for the 100% parameter scale

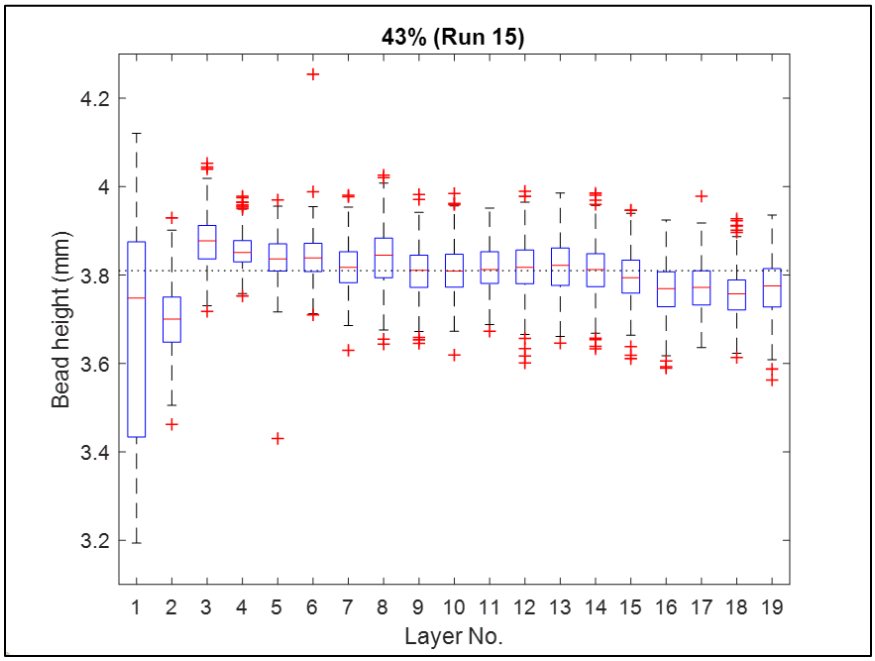

Figure 97 - Statistical analysis of the estimated bead heights for 19 layers of a rectangular part for the 43% parameter scale

The cumulative results in Figures 98 and 99 showed a consistent the bead height across the different test conditions for the 10.2 mm (0.4") and 7.6 mm (0.3") nozzle data.

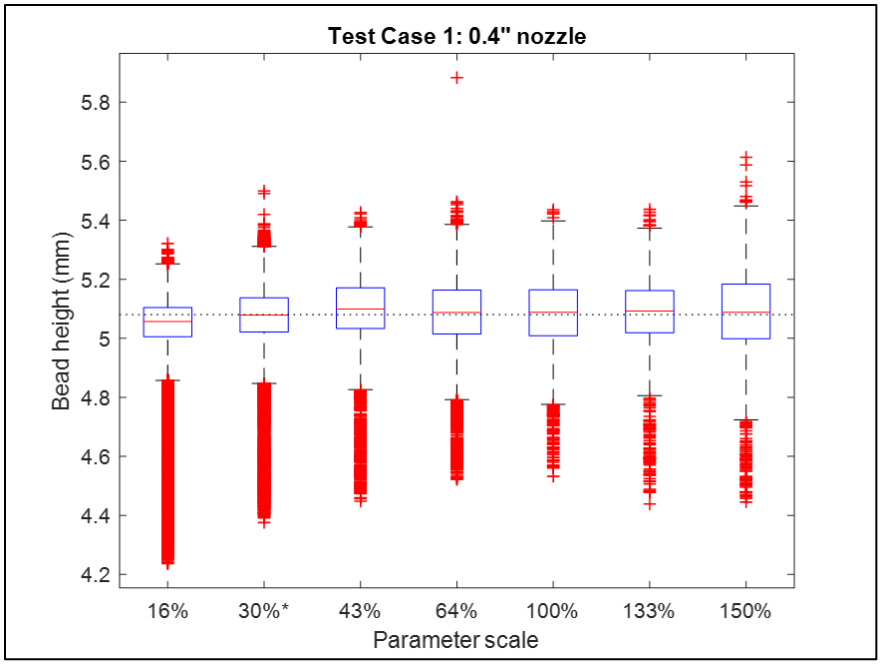

0.4" nozzle: 5.08mm expected bead height

Figure 98 - Cumulative bead height vs parameter scale for the 10.2 mm (0.4") nozzle data

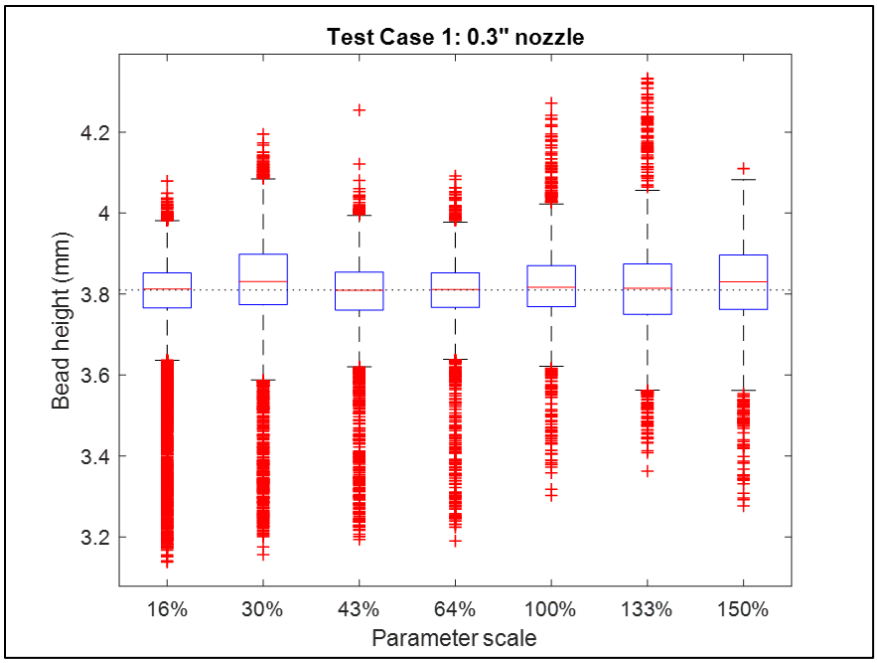

0.3" nozzle: 3.81mm expected bead height

Figure 99 - Cumulative bead height vs parameter scale for the 7.6 mm (0.3") nozzle data

The one-layer-delay results for the 10.2 mm (0.4") and 7.6 mm (0.3") nozzle data shown in Figure 100 showed similar trends as the real-time data shown in Figures 93 and 94.

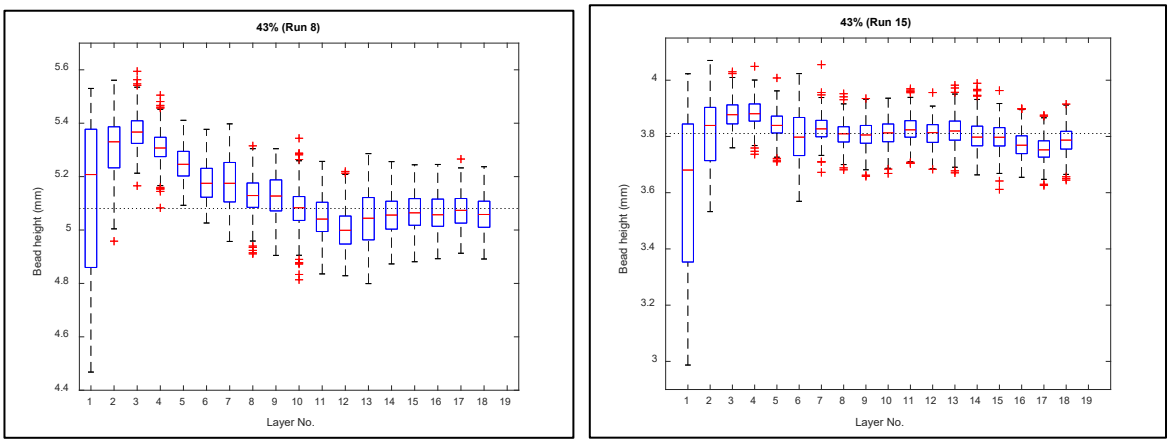

(a) **(b)**

Figure 100: One-layer-delay results at the 43% parameter scale for a) the 10.2 mm (0.4") nozzle with an expected bead height of 5.08 mm and b) the 7.6 mm (0.3") nozzle with an expected bead height of 3.81 mm

The cumulative estimated bead height data for the one-layer-delay results for the 10.2 mm (0.4") and 7.6 mm (0.3") nozzle data shown in Figure 101 were generally consistent across the different test conditions.

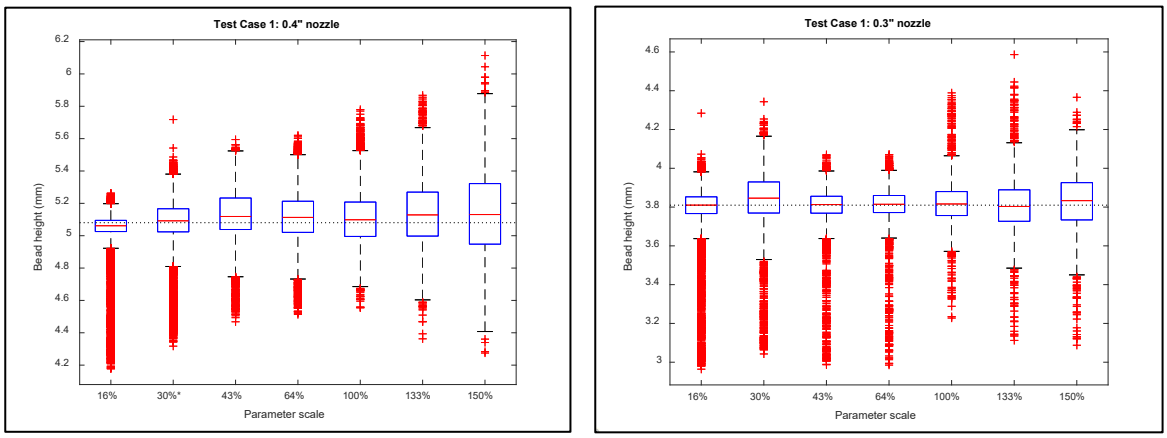

(a) **(b)**

Figure 101: The cumulative estimated bead height for the one-layer-delay results for the a) 10.2 mm (0.4") nozzle with an expected bead height of 5.08mm and b) 7.6 mm (0.3") nozzle with an expected bead height of 3.81 mm

The profilometer data showed that the table surface was not level (assuming the plane the print head moves on is level). Figure 102 shows a plot of the measured table height as the profilometer moved along the top edge of the part. The 19 lines in the plot corresponds to the 19 layers in the print. The height was normalized by the first measured value. Figure 103 shows a plot of the measured table height as the profilometer moved along the bottom edge of the part.

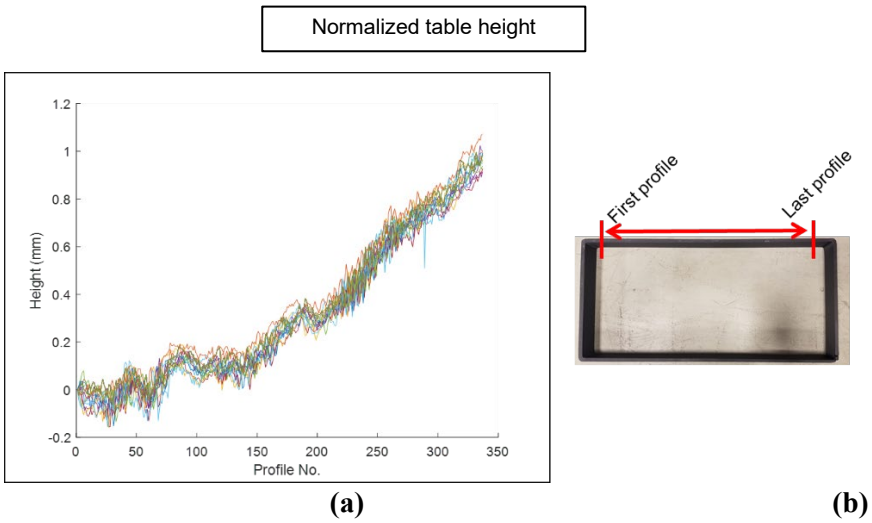

Figure 102 - a) Plot of the measured table height as the profilometer moved along b) the top edge of the part

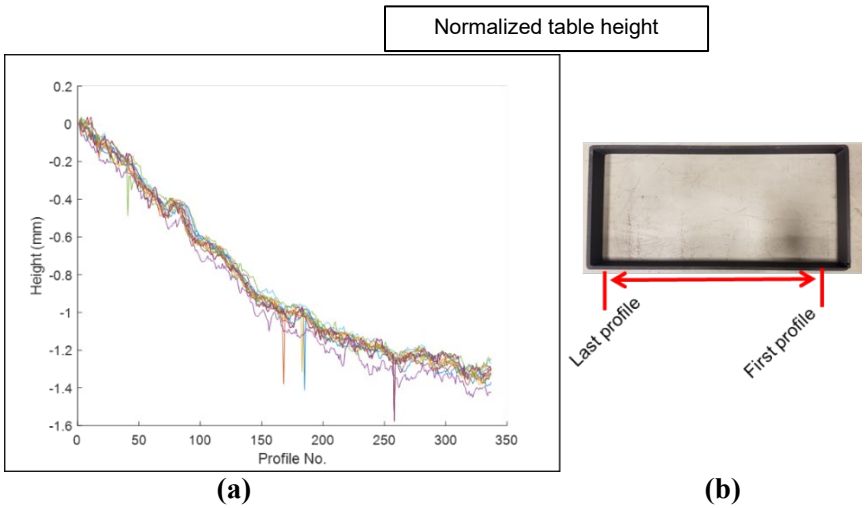

Figure 103 - a) Plot of the measured table height as the profilometer moved along b) the bottom edge of the part

Figure 104 shows the table surface height and the bead height of the first four (4) print layers. The bead height of the first few layers was affected by the uneven table height. By the third layer the bead height was no longer affected.

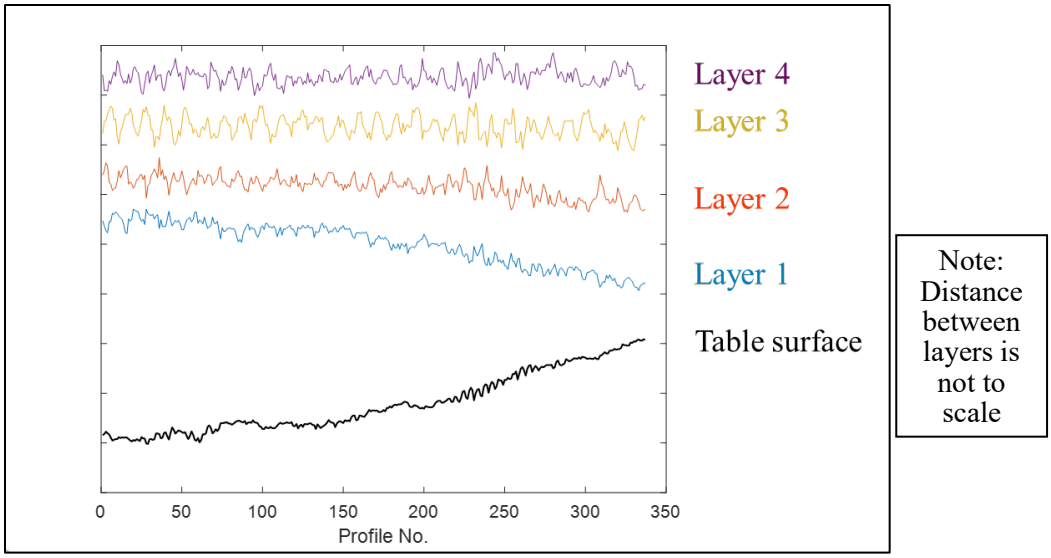

Figure 104 - Shows the table surface height and the bead height of the first four (4) print layers

We measured the overall height of two finished printed parts using a set of calipers

- Part 1: 0.4" nozzle using the 30% parameter scale (see Table 11)
- Part 2: 0.3" nozzle, 100% of nominal parameters (See Table 11)

The height of the parts estimated using the profile data was always higher compared to the height measured with the calibers and the difference was a near constant offset.

For part 1 the mean difference in the estimated height using the profile data was:

- + 2.0 mm using the the real-time profile data
- + 1.7 mm using the one-layer delayed profile data

For part 2 the mean difference in the estimated height using the profile data was:

- + 0.9 mm using the the real-time profile data
- + 0.4 mm using the one-layer delayed profile data

The mean difference using the one-layer data was smaller compared to the real-time data for both parts so this difference may be due to the part shrinking as the it cooled.

The raw bead profiles show position-related trends. Figure 105a shows the estimated bead widths along the bead for each layer for a rectangular part printed at the 100% parameter scale. The results of a frequency analysis performed on this data is shown in Figure 105b. There are two peaks in the frequency spectra at 1 time and 2 times the extruder rotational speed, so the extruder rotation effects the bead width.

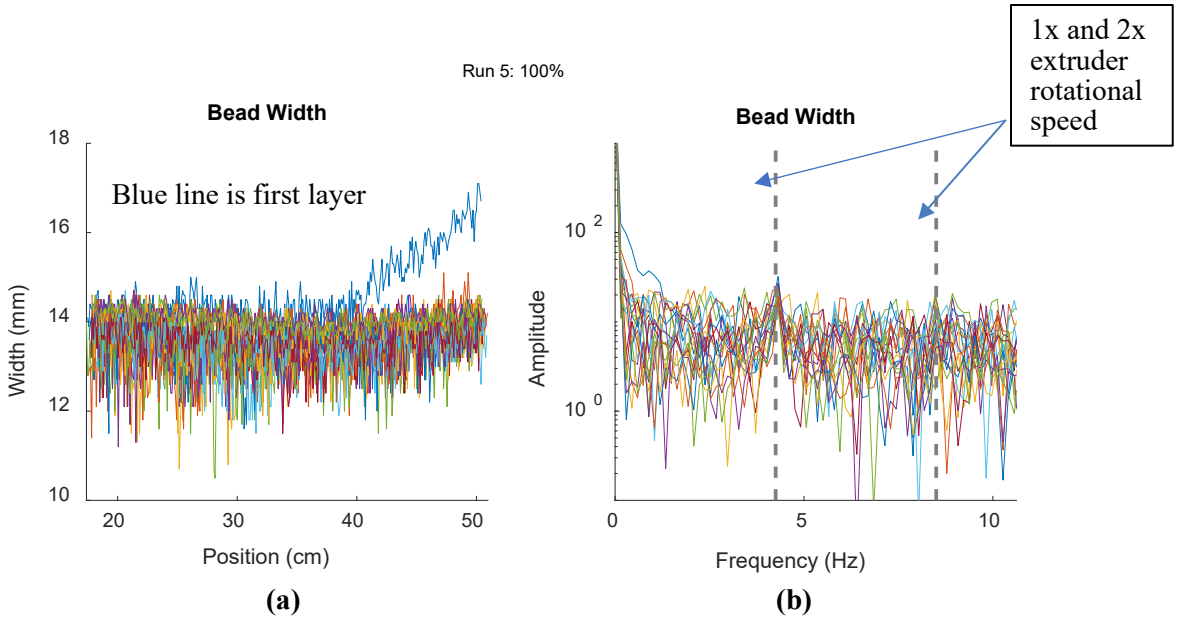

Figure 105 - a) estimated bead widths along the bead for each layer for the 100% parameter scale and b) frequency analysis performed on the bead width data along the bead

Zigzag Prints

The image in Figure 106 shows how the data was collected with the profilometer on curved sections of the zigzag printed parts. The image in Figure 107 illustrates the preferred method for collecting data with the profilometer on curved sections of the zigzag printed parts.

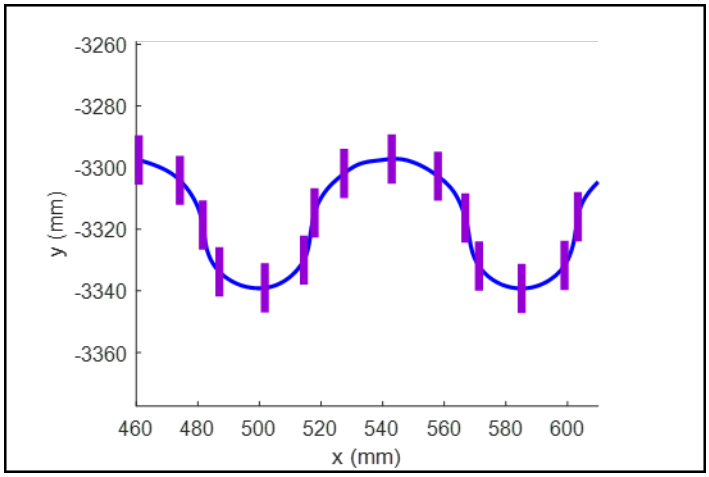

Figure 106 - Orientation of profilometer measurements on curved sections of the zigzag printed parts

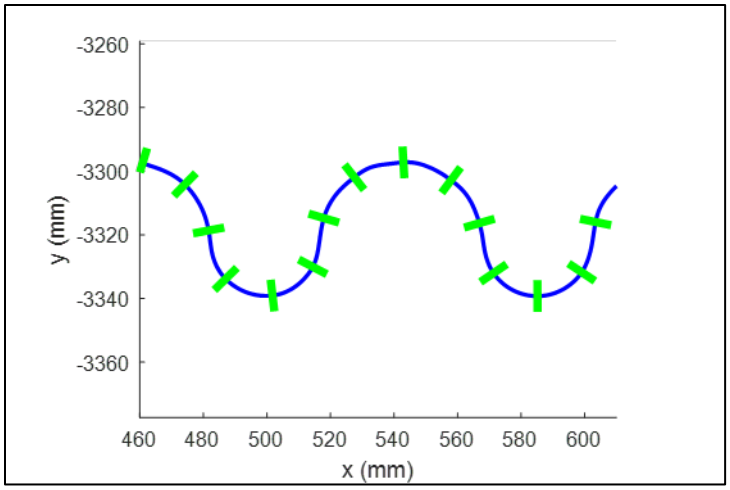

Figure 107 - Preferred orientation of profilometer measurements on curved sections of the zigzag printed parts

Geometric transformations were used to estimate measurements perpendicular to the print path, regardless of the orientation of the profilometer relative to the direction of the print. Using all of the profile data collected on the zigzag part, the desired line of measurement, which is oriented perpendicular to the print path, was identified and the bead width and height were estimated using the measurements along this measurement line, as shown in Figure 108. Figure 109 shows the measured profiles and the estimated perpendicular profiles along the print path of the sawtooth sections of a zigzag part.

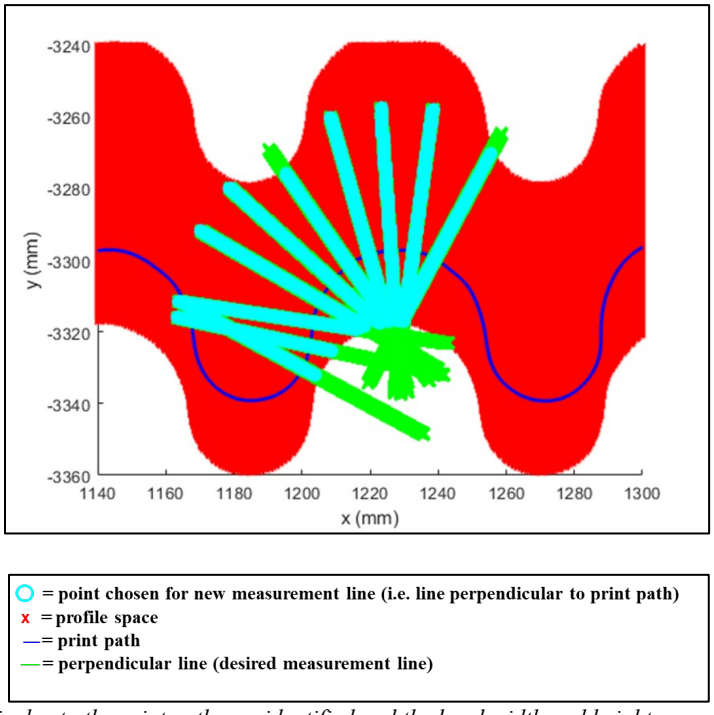

Figure 108 - The perpendicular to the print path was identified and the bead width and height were estimated perpendicular to the print path using all of the profile data collected on the zigzag part

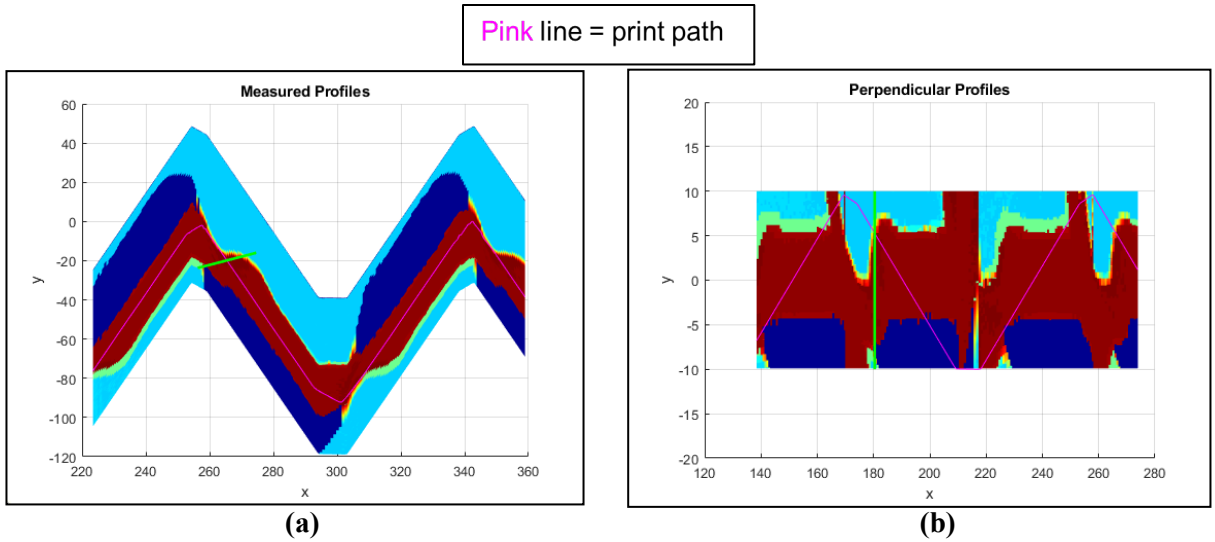

Figure 109: Plots showing a) measured profiles and b) estimated perpendicular profiles along the print path of the saw tooth sections of a zigzag part (dimensions in mm)

There was more invalid data than expected in profile data collected on the zigzag parts and dead zone data occurred mainly when the table was in range as shown in Figure 110.

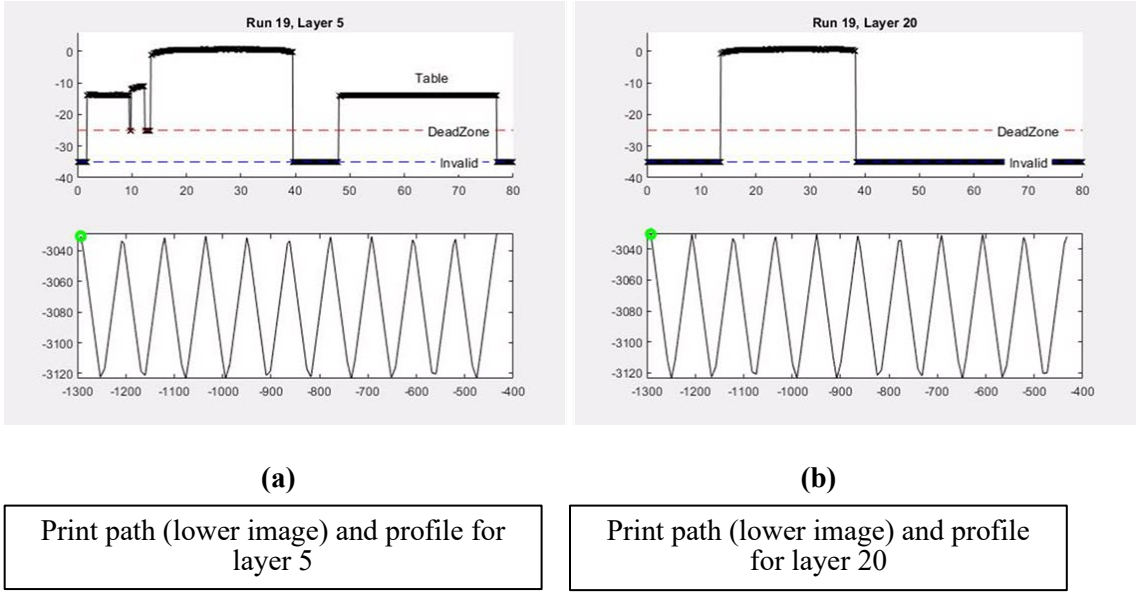

Figure 110 - Profile data collected on the sawtooth sections of the zigzag parts showing a) invalid data and b) dead zone data that occurred mainly when the table was in range (dimensions in mm)

Figure 111 shows measured profiles and the estimated perpendicular profiles along the print path of the curved sections of a zigzag part.

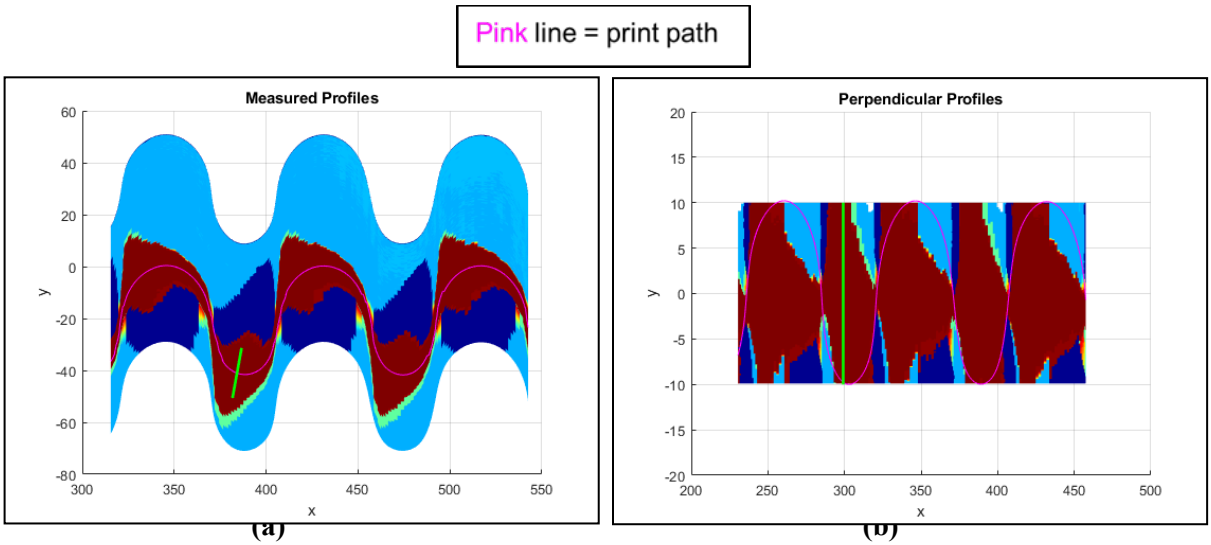

Figure 111: Plots showing a) measured profiles and b) estimated perpendicular profiles along the print path of the curved sections of a zigzag part (dimensions in mm)

Again, there was more invalid data than expected in profile data collected on the zigzag parts and dead zone data occurred mainly when the table was in range as shown in Figure 112. Most issues we discovered (monitoring in all print directions, minimizing dead zones, etc.) could likely be resolved or minimized by using multiple profilometers.

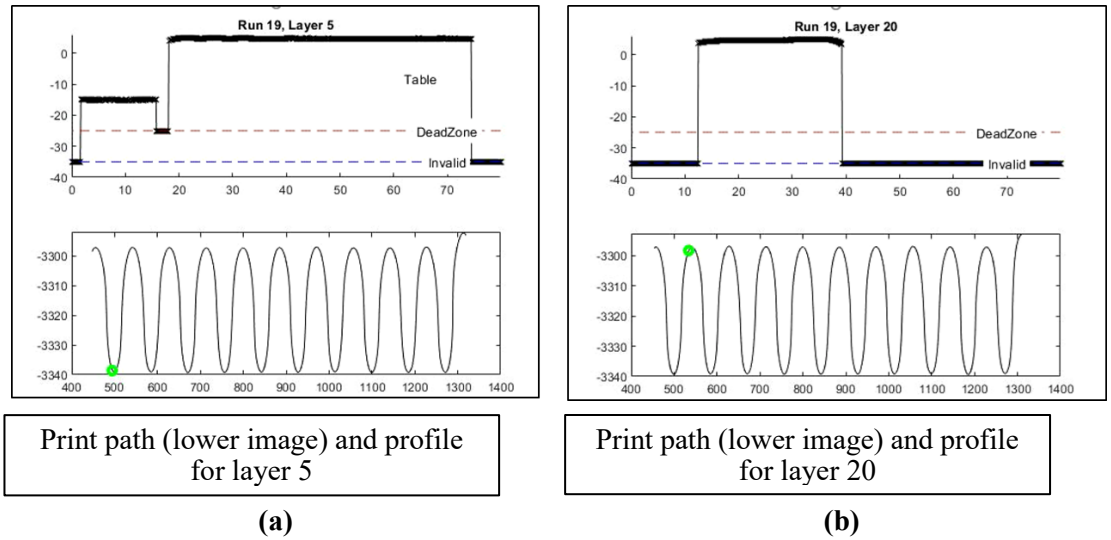

Figure 112: Profile data collected on the curved sections of the zigzag parts showing a) invalid data and b) dead zone data that occurred mainly when table was in range (dimensions in mm)

Additional Findings

The table surface shape (relative to the plane of the print head) shown in Figure 113 indicates that the table was not perfectly level.

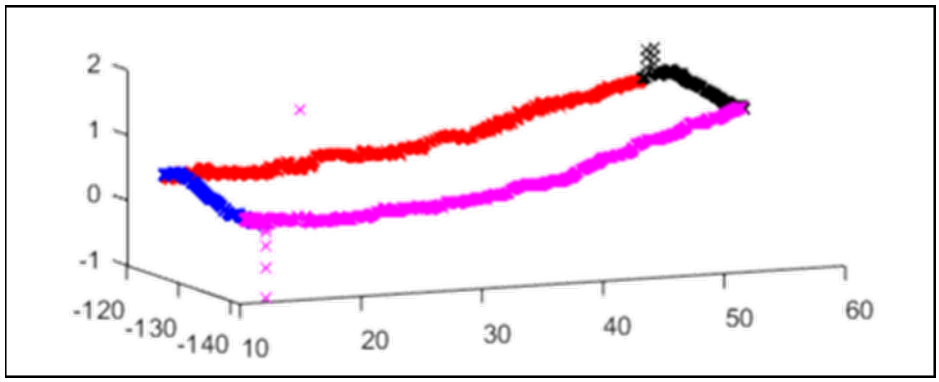

Figure 113 - View of the table a) along the long edge and b) along the short edge (dimensions in mm)

The view of the table along the long edge in Figure 114a showed that the table was close to level from front to back. The view of the table along the short edge in Figure 114b shows that the table was not level from side to side by approximately 1 mm.

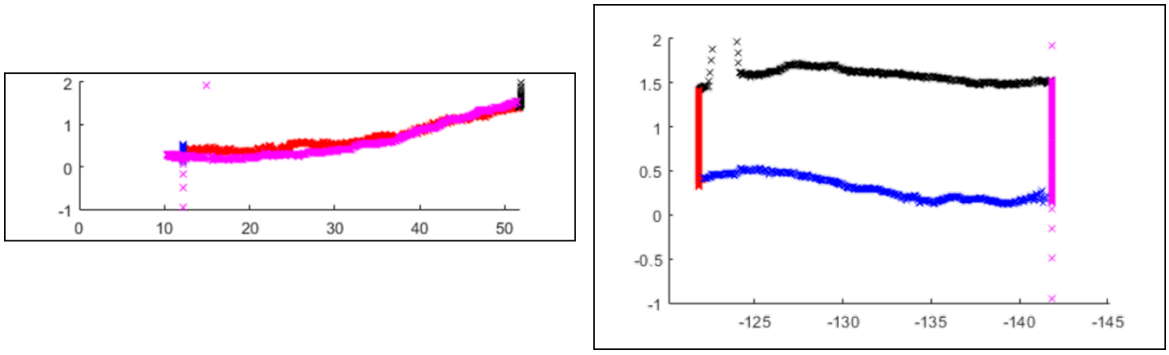

(a) **(b)**

Figure 114 - View of the table a) along the long edge and b) along the short edge (dimensions in mm)

Processing parameters acquired from the BAAM including temperature, pressure, and torque measurements were analyzed to determine if there was a correlation between bead width and/or height and each parameter. Because the temperature changes occurred slowly relative to the profilometer sampling rate (50 or 100 Hz), no temperature correlations were found. No consistent trends in the extruder pressure and torque measurements were found. The correlation analysis performed was cursory in nature in that we were looking for obvious trends in the pressure and torque data that correlated well with the trends in the bead height and width data. It is possible that a more thorough analysis could establish a link between the process parameters and the bead and height and width measurements. Figure 115 is an image of a rectangular part printed on the BAAM showing an example of bead variation and Figure 116 shows the bead width variation measured with the profilometer.

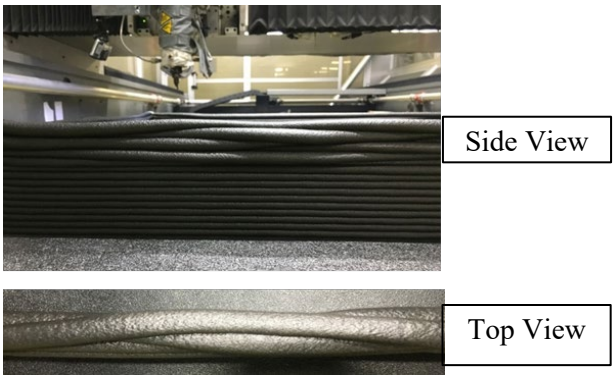

Figure 115 - Example of bead variation in a part printed on the BAAM

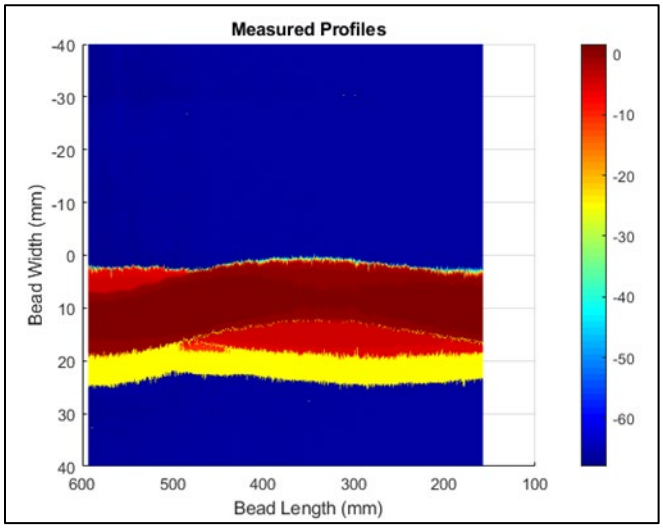

Figure 116 -Bead width variation measured with the profilometer in a part printed on the BAAM

For milestone 3.12.3.1, we were to demonstrate in-process monitoring through the application of machine vision systems that detects bead width variation to within 5%. The expected bead width for this printed part was 10 mm so 5% of expected bead width is 0.5 mm. The resolution of profilometer measurements across the bead width is 0.1 mm. The measured bead profiles in Figure 117 shows that the bead width variation was 0.4 mm. Therefore, a bead width variation of 0.5 mm was detected. Based on these results, milestone 3.12.3.1 has been met.

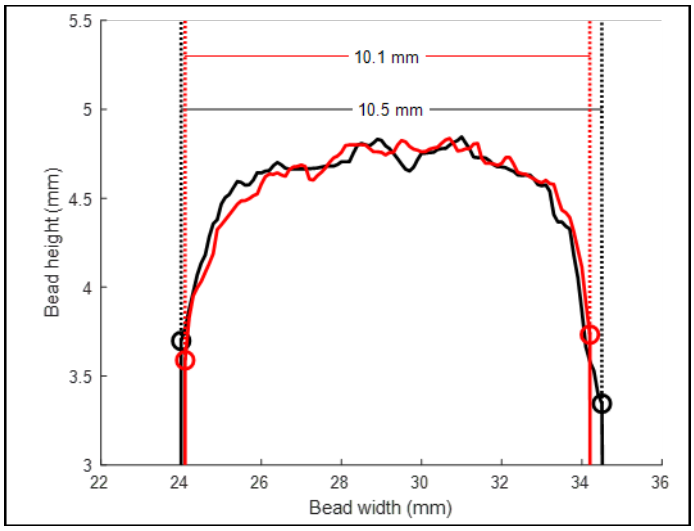

Figure 117 - Plot showing bead width variation is 0.4 mm

Bead height conclusions

- With the profilometer system in the print environment, the profilometer moving with the deposition head and vibration was present, the profilometer system was capable of capturing the bead height variation along the length of the bead and from layer to layer during a print.
- The bead height for the one-layer delay data was very similar to the real-time data.
- The bead height varies based on the parameter scale used for printing the part.
- Knowing the variation in the mean bead height and the variation in the bead height around the mean for a broad range of print variables prior to designing a part, adjustments could be made to the slicing software to create a print model that would reduce height part variation during the printing.

Impacts & Conclusions

Realtime in situ monitoring of the printing process using profilometry could be integrated into the control system of a large-scale deposition printer to better control the overall dimensions of the finished 3D printed part. This could help to reduce or eliminate manufacturing defects such as gaps between beads printed next to each other that could result in a significant reduction in the strength of a printed part.

Overall, we have successfully demonstrated the potential of using profilometry to perform in situ monitoring of the printing process to estimate bead width and bead height. Most issues discovered (monitoring in all print directions, minimizing dead zones, etc.) during the testing could likely be resolved or minimized by using multiple profilometers. By having the precise location of the profilometer(s) from the printer's data, geometric transformations can be used to estimate perpendicular measurements regardless of the direction of the print. A bead width variation of 0.5 mm was detected. Based on these results, milestone 3.12.3.1 was met.

Critical Manufacturing Variables

Final Milestone 3.12.2 Identify critical variables affecting manufacturing quality and z-direction tensile strength and create a mitigation plan with set target ranges for the identified variables to achieve the highest possible quality part**.**

From the material property investigation, the variable that has the largest effect on Z-direction tensile

strength is layer time, as seen in Figure 9. The parameter with the second largest effect was nozzle size as discussed in the material property investigation, data can be seen in Figure 16. The other variables are not considered critical, so long as an aspect ratio of 3 combined with a bead-to-nozzle ratio of 0.77 is avoided as this caused a sharp decline in X-direction strength. For this report manufacturing quality will be defined as minimizing porosity, consistent bead width and consistent bead height in a part. Porosity was primarily impacted by bead-to-nozzle ratio and printing speed. The ideal bead-to-nozzle ratio and aspect ratio for reducing porosity is 0.97 and 3 respectively. If this value cannot be used, then it is better to use a bead-to-nozzle ratio of 0.77 than 0.97. Increasing print speed decreases porosity, the mitigation plan would be to print as fast as possible without causing bead collapse. Bead width and height, at least when printed on the BAAM, did not seem to have a nozzle size or the combination of feed rate and screw speed as a critical variable from the obtained data. For printing on BAAM, bead width and height are likely something that should have feed rate and screw speed dialed in independently while simultaneously considering layer time.

Variation in Properties of Interest in LSED Process

Final Milestone 3.12.3 For demonstration of the plan to be successful, the measured bulk porosity, z-direction tensile strength, and the extruded bead width must be accurate within 10% of the set target values agreed by team in the gated final milestone 3.12.1 review or earlier.

In a manufacturing environment, especially one that has to do with structures that are critical to a person's safety, it is important to understand the variance of parts created by a process. If parts created by a process have a large variance, it means that the design process must consider this variance when doing structural modeling, tolerancing and assembly. For structures critical to a person's safety the worst-case scenario must be designed around, a large variance makes this even more complex and can cause significantly more material to be needed to meet a defined safety criteria or factor of safety. As the nature of this project is involved with using LSED in structural applications, it is important for the variation of the process to be determined. Milestone 3.12.3 dictated measured bulk porosity, z-direction tensile strength, and the extruded bead width to be within 10% of set target values to be successful. These values are a porosity of 6.0%, Z-direction modulus of 2500 MPa, Z-direction strength of 22 MPa and a bead width of 0.8 inches.

Porosity was already discussed in the material properties section. As there are so many parameters that were investigated and each of them affecting porosity differently it is important to determine which set is being compared to the target value. The data set chosen was B3 as printing speed was one of the critical variables for porosity, porosity data can be seen in Figures 7 and 8. Printing speed is also easily adjustable in the print. The statistics for this data set were an average of 5.9% porosity and standard deviation of 0.5%. These results are within the 10% dictated by the milestone.

Instead of using simple test geometries Local Motors chose to take tensile samples and bead measurements from Olli prints as this demonstrates utilizing LSED for structural applications. Tensile samples were taken from the wheel wells which are cut out of every Olli, a depiction of which can be seen in Figure 118. The samples span various layers of the Olli, which represent a more complex thermal history than hexagon print geometries used for tensile samples earlier. 44 samples were tested from Olli diagonally opposite wheel wells, 12 samples each from 4 different vehicles. 4 samples were unable to be tested accurately and were not included the data. The average Z-direction modulus for these samples was 2700 MPa with a standard deviation of 265 MPa and the average Z-direction strength was 22.48 MPa with a standard deviation of 1.93 MP. These results were also within the 10% expected.

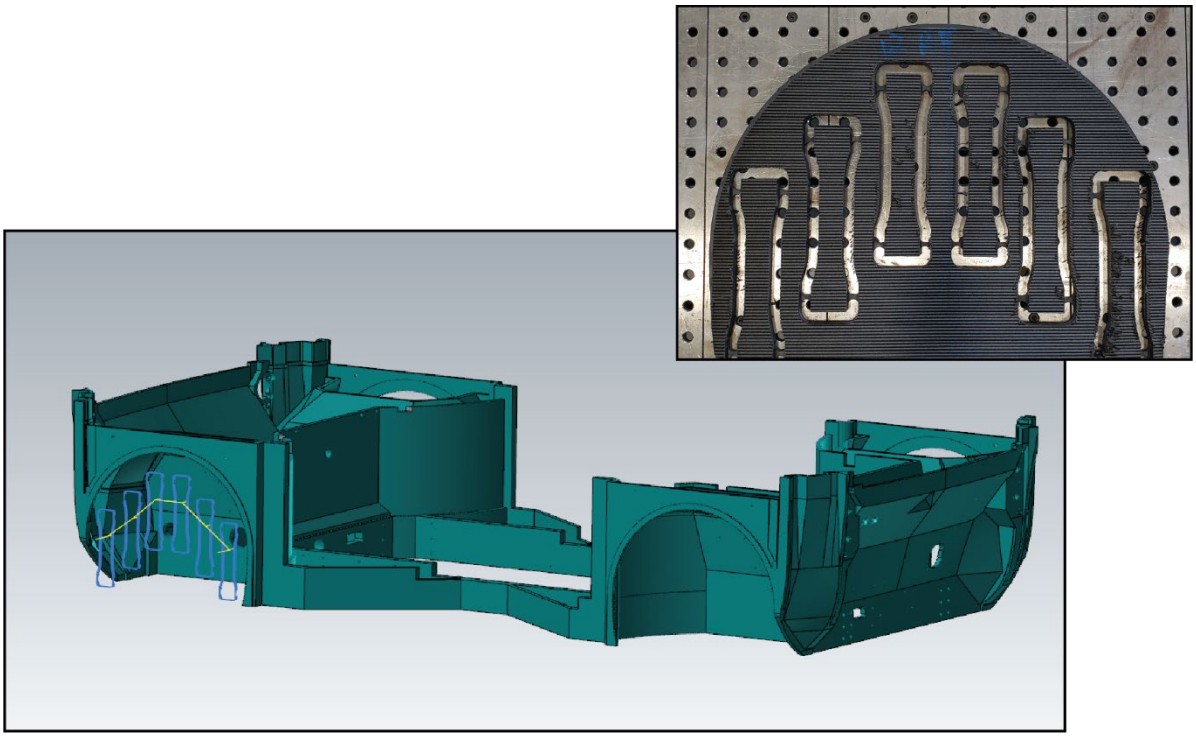

Figure 118 - Image showcasing location of the samples for the process variation study in reference to the Olli

The final process variable described in the milestone was the bead width. There were two approaches taken, bead width within the layer and bead width across multiple layers. All measurements were taken by hand with a pair of calipers from the process variable prints discussed earlier. The graphs for the two approaches can be seen below in Figures 119 and 120. Measurements for bead width within a layer were taken at various areas in the top layer, while the bead width across layers were taken at same the X and Y locations for the measured layers. Bead width within a layer was very consistent with no outliers, producing an average of 0.798 inches with a standard deviation of 0.004 inches. The bead width across layers produced only one outlier in layer 2, there was no apparent reason for this increased bead with that the current PI is aware of. Otherwise, the data is consistent and in total provides an average of 0.826 inches and a standard deviation of 0.006 inches.

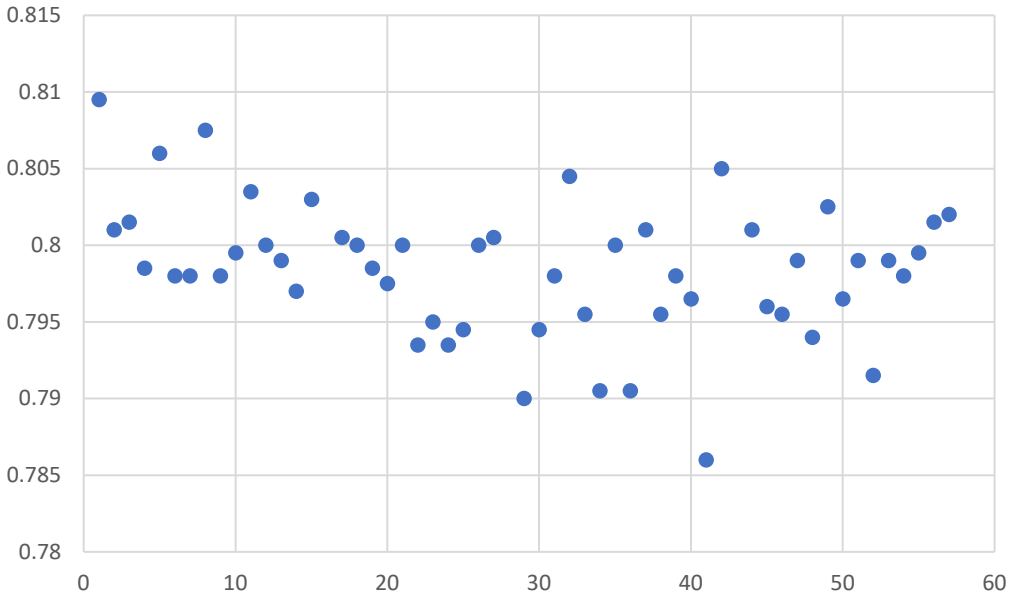

Figure 119 - Graph of bead width measurements take within a single layer at various locations

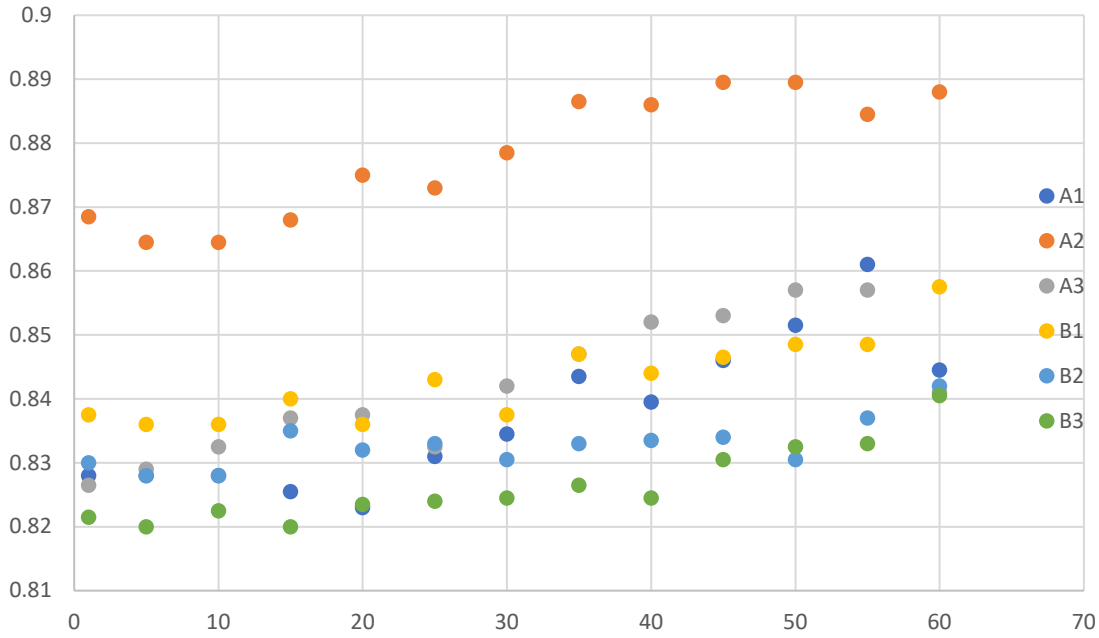

Figure 120 - Graph of bead width measurements taken across multiple layers at the same X and Y locations.

Part Deformation Simulation

Milestone 3.12.4.2 Simulation of LSED process to predict part deformations has been demonstrated and verified to be accurate within 10% by part scanning.

The Extrusion deposition additive manufacturing (EDAM) process involves multiple phenomena including heat transfer, shrinkage, polymer crystallization, fusion bonding, and thermoviscoelasticity which develops at different time and length scales. A comprehensive physics-based simulation framework (ADDITIVE3D©) developed at Purdue University captures the relevant phenomena occurring in the EDAM process with fiber reinforced polymers [5], [30]–[32]. ADDITIVE3D© allows for simulating the EDAM process as well as to perform analyses of the as manufactured part, thereby capturing the effects of manufacturing such as residual stresses, local orientation etc. Figure 121 shows the simulation workflow in ADDITIVE3D©. To simulate the EDAM process, an AM system card and a digital material card which are unique to an EDAM system, and a material system are required. A digital material card was generated during this program for polycarbonate (PC) reinforced with 20% by weight of carbon fiber (CF-PC).

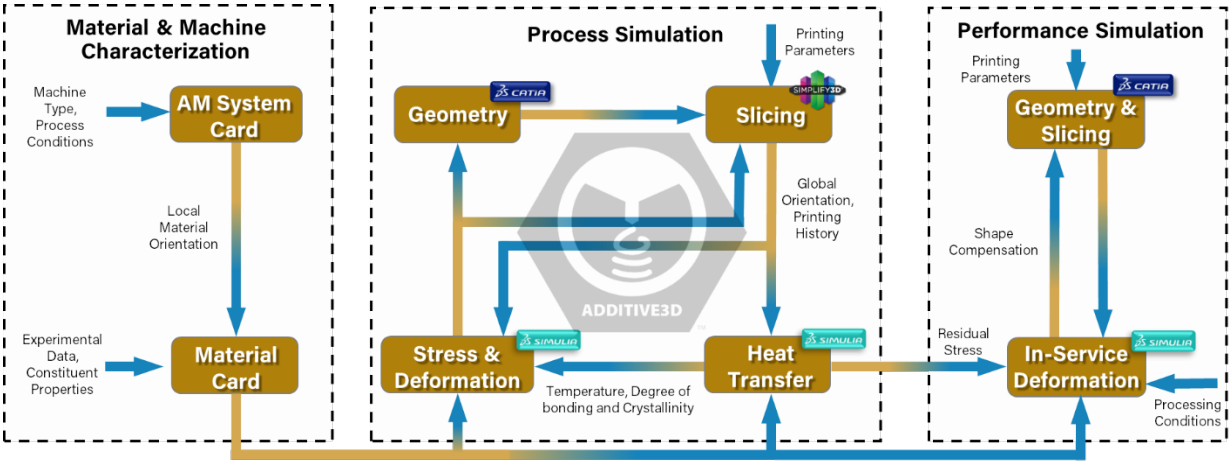

Figure 121 – Physics-based simulation workflow in ADDITIVE3D©

The generation of a digital material card involves extensive experimental and virtual characterization of the printed material for a set of fixed printing conditions, namely nozzle dimensions, bead-to-nozzle area ratio, and bead aspect ratio. Further, the EDAM involves phenomena that develop at different time and length scales. Figure 122 shows the different length scales involved in EDAM (molecular scale omitted in the figure) starting at the microstructural level and followed by the bead and meso-scale level. To generate a digital material card, effective material properties (homogenized) are characterized at the level of the printed bead, thereby allowing to capture interactions developed at larger length scales.

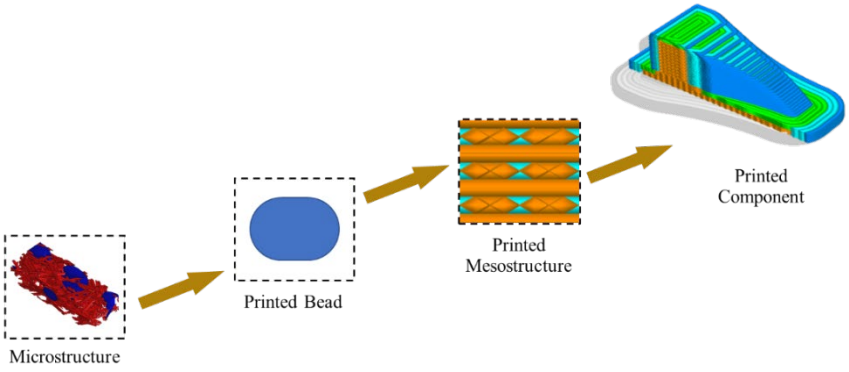

Figure 122 - Material properties are characterized at the scale of the printed bead

Table 15 lists the material descriptors and material properties required for generating a digital material card along with relevant standards followed for the characterization of the material properties. The glass transition temperature T_g, and the coefficient of thermal expansion in the three principal directions were characterized by the University of Tennessee using DMA, and TMA, respectively. The tensile properties along the 1 and 3 directions and Poison's ratio ν_{13} were experimentally measured by Local Motors from dog-bone shaped specimens extracted from printed panels. The other six elastic properties required to describe an orthotropic material system, namely $E_2, G_{12}, G_{13}, G_{23}, \nu_{12}, \nu_{23}$ were predicted using micromechanics as described below. The fiber orientation as well as the elastic properties of the polymeric matrix were obtained via reverse engineering. The viscoelastic behavior of the printed material was characterized by the Purdue team via stress relaxation experiments performed at temperatures from the ambient temperature and past T_g. Measurements of the thermophysical properties, namely density, thermal conductivity, and heat capacity, was outsourced by Local Motors to Thermophysical Laboratory located in West Lafayette, Indiana.

Table 15 Summary of material properties and descriptors required for generating digital material card for a fiber reinforced amorphous polymer.

Material Property/Descriptor	Relevant Standard
Tg - DMA	ASTM D7028
Fiber Orientation Tensor	-
Tensile Properties (3 Directions)	ASTM D638/D3039
Shear Properties	ASTM D5379
Coefficient of Thermal Expansion (3 Directions)	ASTM E831
Thermoviscoelastic Behavior	ASTM D5023
Thermal Conductivity (3 Directions) & Heat capacity	ASTM E1461 &ASTM E1269

Digital Material Card of CF-PC for ADDITIVE3D©

This section summarizes the material behavior characterized for the CF-PC to generate a digital material card. The effective (homogenized) material behavior was characterized at the level of the printed bead and is described according to the orientation convention shown in Figure 1.

The tensile properties in the 1 and 3 directions and Poison's ratio ν_{13} were experimentally measured by Local Motors from dog-bone shaped specimens extracted from printed panels. These results can be seen in the material property testing section. When this data was supplied some experimentation had not been completed and the other six elastic properties required to describe an orthotropic material system, namely $E_2, G_{12}, G_{13}, G_{23}, \nu_{12}, \nu_{23}$ were predicted using the virtual characterization method.

Virtual Material Characterization

To complement the experimental mechanical characterization of the printed material, micromechanics-based methods were used to fully characterize the mechanical properties of the composite. However, the micromechanics models require inputs which include the elastic modulus and poisons ratio of the polymer, and the orientation tensor of the short fiber system. To that end, this section presents a method to calculate, virtually, the orientation of the fiber and the in-situ properties of the polymer. The problem is posed as a 'reverse' engineering or inverse problem where some macroscopic properties of the composite are measured, and the properties of the constituents and microstructural characteristics are estimated.

The reverse engineering problem at hand is ubiquitous in literature and is more commonly referred to as inverse problems or model calibration problems. To proceed with the mathematical formulation, let $\boldsymbol{y \in R^m}$ be a set of experiments conducted to infer the model parameters. Physical systems are mathematically represented using a set of model parameters, $\boldsymbol{x \in R^d}$ and a suitable model $\boldsymbol{f(x) : R^d \rightarrow R^m}$. The reverse engineering problem can now be defined as shown in Equation 16.

$$\boldsymbol{x^* = arg\ \min_x\ l(f(x), y)} \tag{16}$$

where $l(\cdot,\cdot)$ is a suitable error metric. A two-step homogenization method implemented in Digimat© is the model and the parameters are the matrix modulus (E_m), matrix Poisson's ratio (ν_m), and the two terms of the orientation tensor $(a_{11},\ a_{22})$. This enables the third component of the orientation tensor to be calculate by, $a_{33} = 1 - a_{11} - a_{22}$. The micromechanics model predicts the 9 independent constants necessary for the orthotropic material description. However, only 5 of the 9 constants are experimentally determined namely - E_1, E_2, E_3, ν_{12}, and ν_{13}. Although some of the shear moduli are measured with experiments, they are not used in the reverse engineering process since the compliance of the interfaces between beads is not considered in the mean-field homogenization micromechanics model, thus leading to erroneous reverse engineered properties. With this limited information, a squared error loss metric as shown in Equation 17 is proposed.

$$l(f(\boldsymbol{x}), \boldsymbol{y}) = \sum_{i=1}^{5} \left(\frac{f_i(x)}{y_i} - 1 \right)^2 \tag{17}$$

where $f_i(\boldsymbol{x})$ is the model prediction for experiment y_i. Note that Equation 17 is essentially the square of the Euclidian norm of the normalized error between the model predictions and the experimental measurements. Response surface approximation is a methodology that approximates an engineering system to optimize some or all of it parameters. In this study, we approximate the loss metric shown in Equation (2) using this methodology. That is, we need to find a function, $l'(w, b)$, that satisfies $l'(w, b) \approx l(f(\boldsymbol{x}), \boldsymbol{y})$. Approximating the loss metric enables the use of complex and computationally expensive micromechanics models but keeping the reverse engineering simple and computationally inexpensive. The method samples the input space at specific locations and evaluates the loss metric at these locations. Once this data is synthesized a suitable map between the input parameters, x, and the loss metric, y', is created which is used for the optimization process. To that end, the support vector regression (SVR) method is used in this study to create the map.

To create the data set for the SVR fitting, we sample the inputs using the Latin Hypercube design. Once the inputs have been sampled, the loss metric as shown in Equation 17 is used at these input points to create

the data set. Using this data set the response surface is created and the reverse engineering is performed using the sequential least squares programming method. The method used can be summarized using the flow-chart illustration shown in Figure 123.

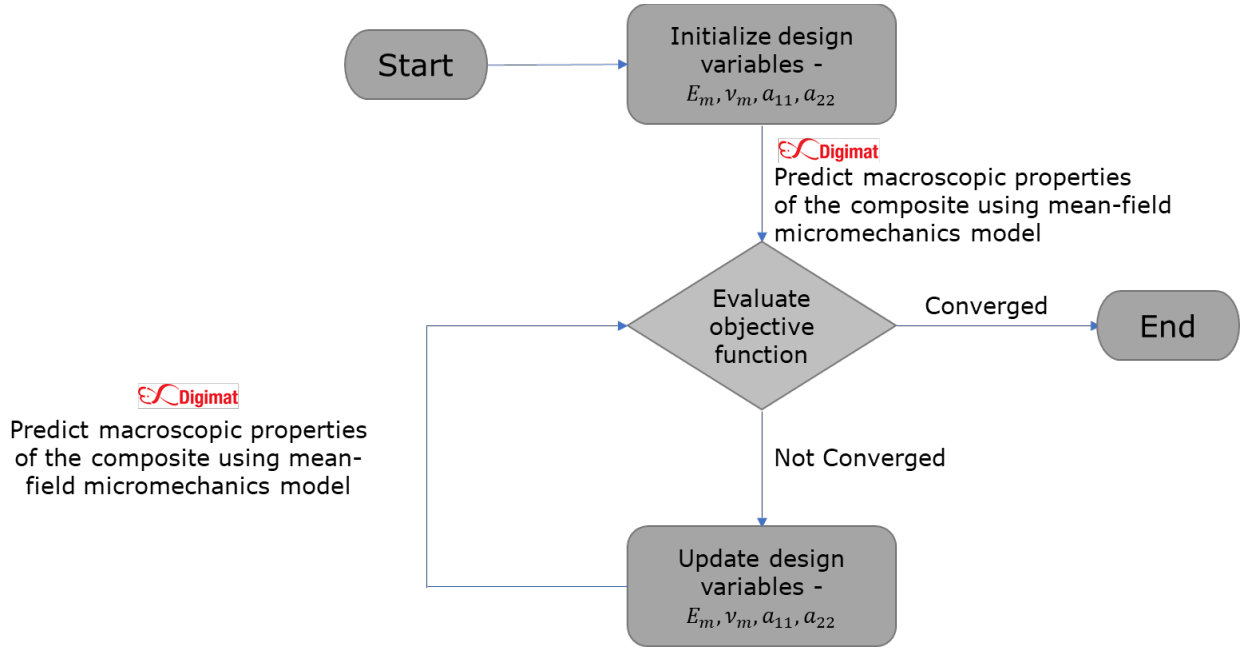

Figure 123 - Flow chart illustrating the reverse engineering methodology

Note that in Figure 123 there is no mention about the response surface approximation and is only meant for an understanding of the reverse engineering procedure at a higher level. Once the properties E_m, ν_m, a_{11}, and a_{22} are determined, the micromechanics model can be used to find the mechanical properties that are not measured experimentally.

The mechanical properties measured experimentally by Local Motors were used to reverse engineered the effective elastic modulus of the matrix used in the CF-PC ($E_m = 1.83\ GPa$), the Poisson's ratio of the matrix ($\nu_m = 0.34$), and the diagonal components of the second order fiber orientation tensor ($A_{11} = 0.64$, $A_{22} = 0.29, A_{33} = 0.07$). Table 16 list the elastic properties of the CF-PC measured experimentally and virtually.

Table 16 - Summary of elastic properties characterized experimentally and virtually.

Composite Property	Experimental	Reverse Engineered
$E_1\ (GPa)$	10.12	9.85
$E_2\ (GPa)$	NA	4.78
$E_3\ (GPa)$	2.87	2.95

ν_{12}	0.31	0.39
ν_{13}	0.36	0.34
ν_{32}	0.30	0.25
$G_{12}\ (GPa)$	NA	2.42
$G_{13}\ (GPa)$	NA	1.31
$G_{23}\ (GPa)$	NA	1.16

Experimental Validation of Additive Process Simulations with ADDITIVE3D©

Simulation predictions for temperature history and deformation were validated against experimental measurements for two geometries printed in the LSAM system, a plate printed with an antisymmetric print orientation ($[0_2/90_2]$) and a curvilinear shape referred to as "racetrack". Both geometries were printed on top of a sheet of acrylonitrile butadiene styrene (ABS) held with vacuum to the build plate (build sheet).

The plate with antisymmetric print orientation was designed to develop significant out-of-plane deformation due to stresses induced by the anisotropy of the printed material and by the temperature gradients developed during the printing process. The plate develops a hyperbolic paraboloid upon removal from the build sheet. Geometries with flat and smooth surfaces are preferred since these are less susceptible to error in the laser measurement of deformation. In other words, the scalloped surface introduced with the rounded ends of the printed beads can obscure the measurements of deformation, which is circumvented by using a simple flat plate. Figure 124 shows the CAD geometry and the finite element mesh generated with ADDITIVE3D© for simulating the printing process.

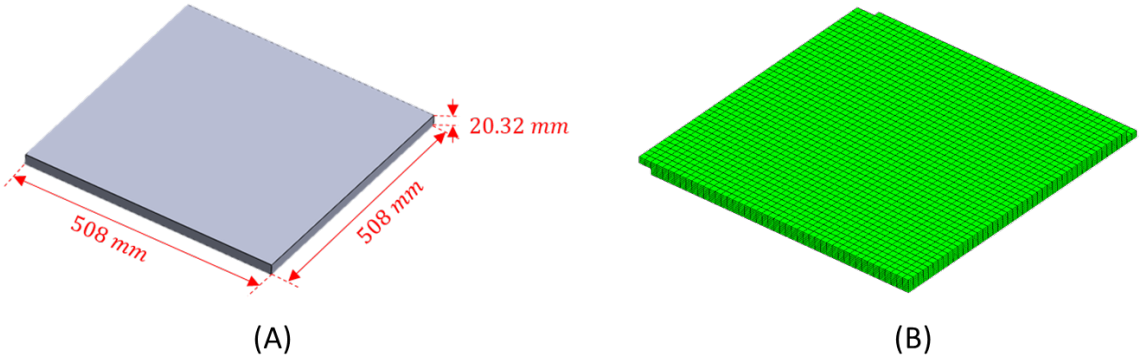

Figure 124 - A) CAD geometry of plate with antisymmetric print orientation. B) Finite element mesh of plate

The racetrack was designed to promote in-plane deformation and to provide a vertical wall for extracting time temperature histories at multiple layers. Figure 125 shows the geometry of the racetrack and the finite element analysis (FEA) mesh used in the process simulations. The in-plane deformation developed in the racetrack is primarily caused by the difference in CTE between the radial and hoop directions in the curved regions of the geometry [33]. A distribution of internal stresses in both the hoop and radial directions develops in curved regions printed with anisotropic materials as the material cools from the melt to the ambient temperature. Further, the adhesion of the printed material to the build plate constrains the deformation, thereby giving rise to internal stresses. As a result, the part springs in while the internal stresses re-equilibrate upon its removal from the build plate. To magnify the spring-in deformation in the racetrack,

straight segments are connected to the ends of the curved regions. In addition to providing for measurements of the in-plane deformation, the racetrack provides vertical walls that are used to extract time-temperature history at different layers, which serve for validating the simulation predictions.

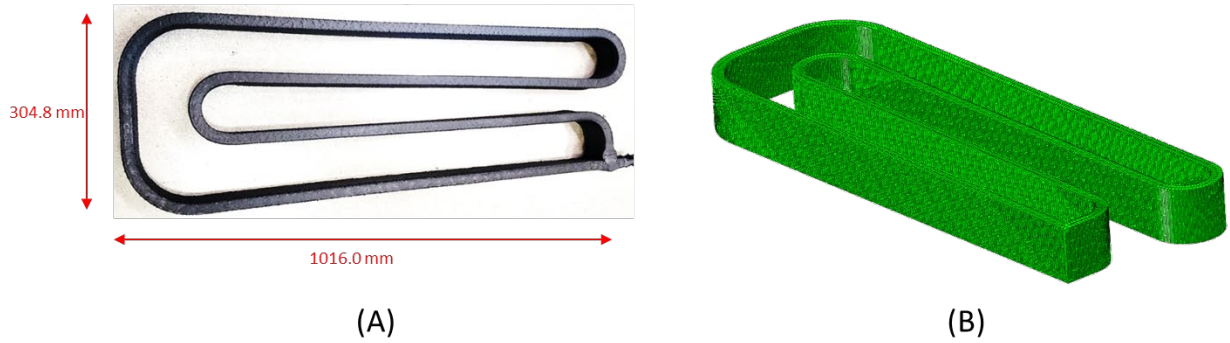

Figure 125 - A) Geometry of the racetrack. B) Finite element mesh of the racetrack

Validation Experiments

Experimental validation of the simulation predictions is of paramount importance to provide confidence on the simulation results and to verify the material card. Therefore, experimental validation of the temperature fields, time-time history, and deformation was carried out for the two geometries investigated in this program.

Plate with antisymmetric print orientation

Figure 126 shows a qualitative comparison between the temperature fields captured with the thermal camera (top row) and the temperature field predicted in the process simulations (bottom row) after printing the second, third and fourth layers while attached to the build plate. The temperature fields in both the experimental and simulation fields are plotted on the same scale. Overall, temperature fields characterized experimentally and predicted through the EDAM process simulations are in good agreement.

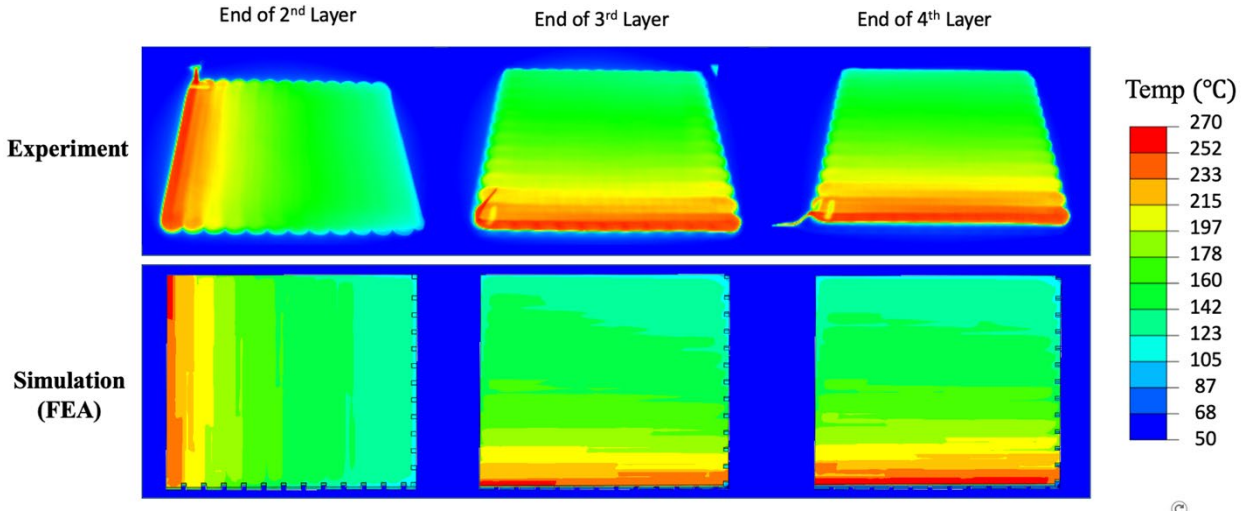

Figure 126 - Comparison of temperature fields measured experimentally and predicted with process simulation at different instants of the printing process of the plate

To provide a quantitative comparison of the temperature fields shown in Figure 126, temperature was extracted along profiles drawn along the width of the plate. Figure 127 shows a quantitative comparison of

the temperature profile developed along the width of the printed plate (orange marks) with the predictions in the process simulations (blue marks). The temperature was extracted along the white dashed line at the end of printing process of the third and fourth layers. In general, temperature profiles characterized experimentally and predicted through the EDAM process simulations are in good agreement and within $\pm 10\,°C$. A slightly higher variation between the predictions and the measurements is observed in the warmest region of the plate.

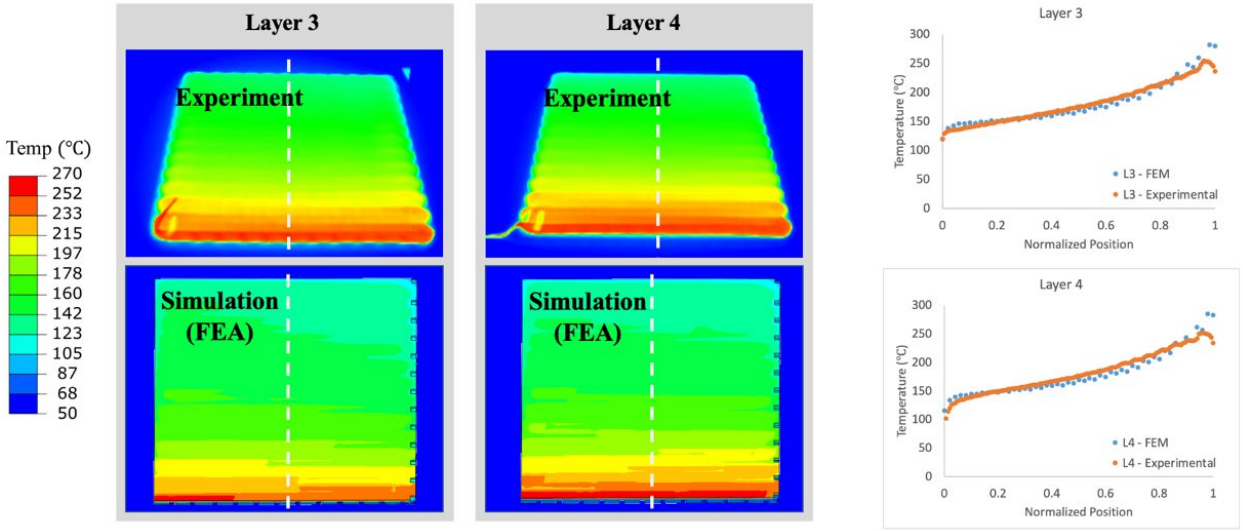

Figure 127 - Comparison of temperature profile across the plate measured experimentally and predicted with process simulation after third- and fourth-layer completion

After validating the temperature predictions, validation of the deformation predictions was carried out for the plate. Figure 128 shows the displacement in the layer stacking direction (3-direction) developed at the end of the printing process (A), after cooling of the printed plate for 30 minutes on the build plate (B), and after the plate was removed from the build plate (C). A hyperbolic paraboloid with different radii of curvature was observed. The hyperbolic paraboloid developed by the printed plate shows a significantly different radius of curvature along the X-direction than the Y-direction. Such a difference in the radii of curvature is caused by two mechanisms. First, the thermal residual stresses developed during the printing process. Second, the initiation of debonding of the plate from the build sheet at the edges of the part oriented parallel to the global X-direction. Debonding at the edges parallel to the global X-direction allowed the part to curve up along the Y-direction, thereby increasing the bending stiffness of the plate in the opposite direction (X-direction). Once the plate was released from the substrate, the plate continued to deform as it cools to the ambient temperature as shown in Figure 128.

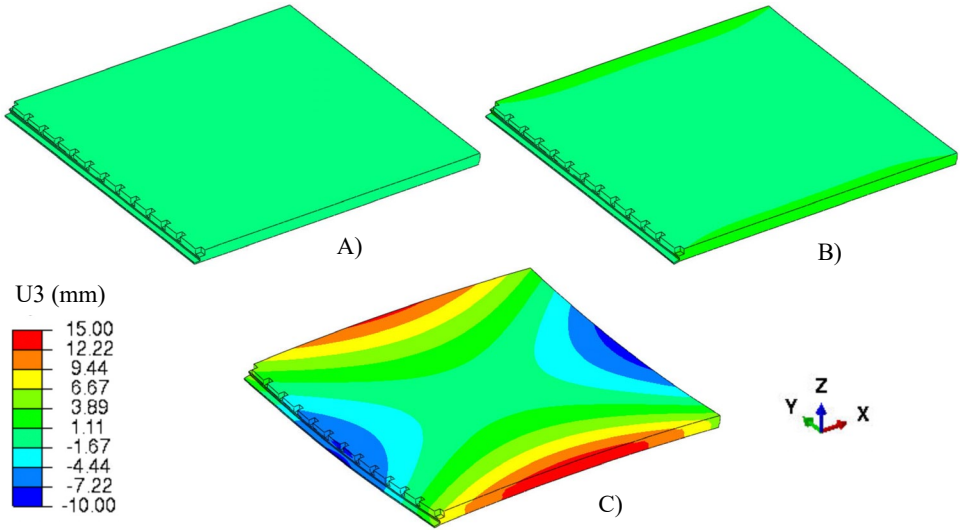

Figure 128 - Displacement in the layer stacking direction (3-direction) predicted for plate printed with CF-PC. A) At the end of the printing process. B) After cooling for 30 minutes on the build plate. C) After releasing from the build plate

A deviation analysis of the deformation predicted with ADDITIVE3D© against the deformation measured experimentally was carried out. The deformation predicted with ADDITIVE3D© was extracted at the nodal locations of the finite element mesh and translated into a point cloud data file. A Faro® laser scanner was used to characterize the deformation at the top surface of the printed plate after removal from the build sheet. The software Geomagic Wrap© was then used first to best fit align the point clouds of the simulation predictions with the experimental measurements and then to perform a deviation analysis. The deviation represents the normal distance between each data point extracted from the simulations and a surface generated from the data points characterized with the laser scanner. Figure 129 shows the deviation of the shape predicted through the process simulation with respect to the experimental measurement. The deviations between the two shapes are within ±1.0 mm which represents around 6.7% of the maximum out of plane deformation (deformation in the 3-direction shown in Figure 129).

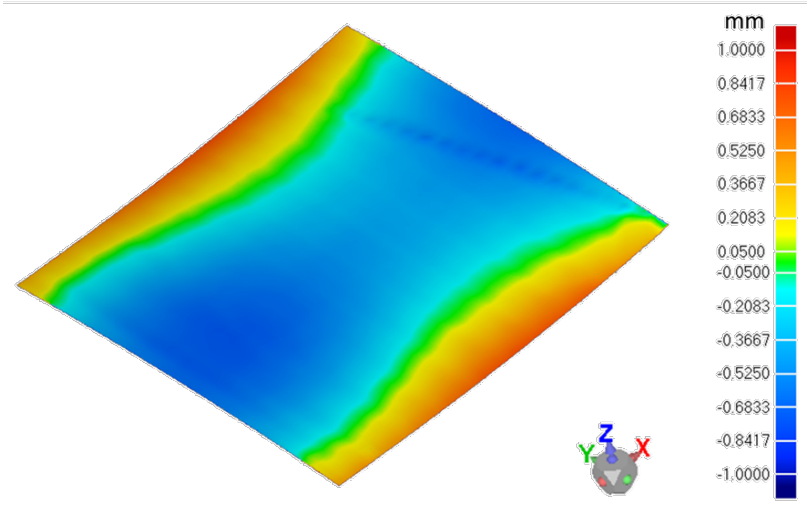

Figure 129 - Deviation of the shape predicted through the process simulation with respect to the experimental measurement for CF-PC.

Racetrack

Figure 130 shows a qualitative comparison between the temperature field captured with a thermal camera and the temperature field predicted in the process simulations (FEA) after the deposition of 5 layers, 15

layers, and 20 layers. The scales in both temperature fields are kept the same to compare side-by-side the experimental and predicted temperature fields. Overall, there is a good correspondence between the experimentally and predicted temperature fields.

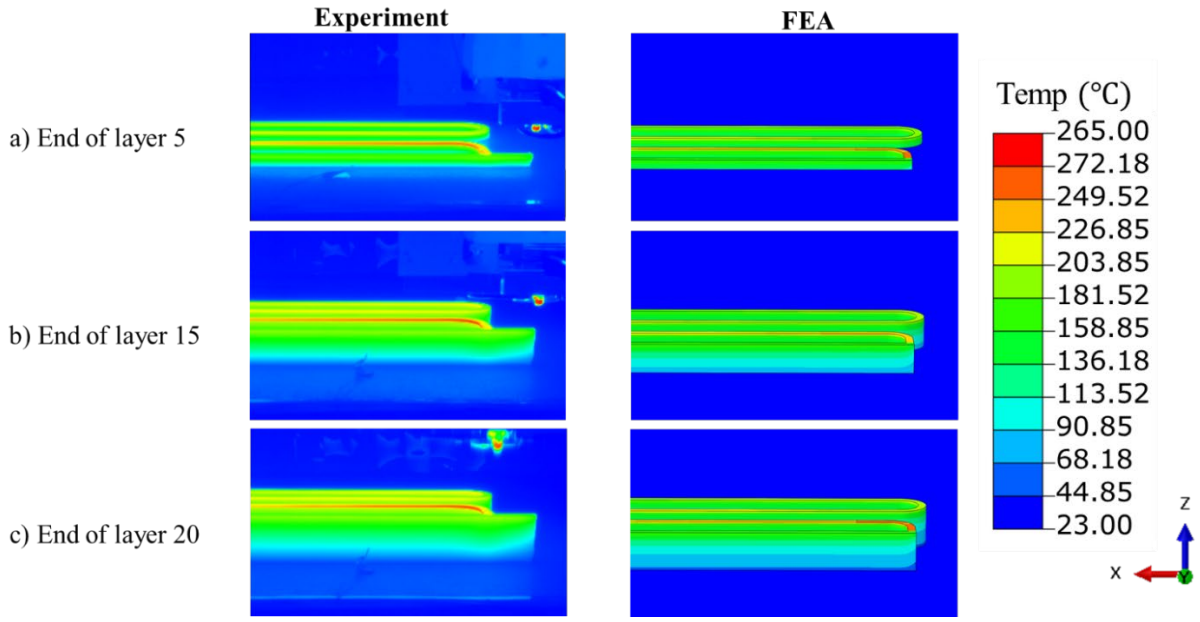

Figure 130 - Validation of temperature fields characterized experimentally (left) and predicted (right) in the EDAM process simulation. A) Temperature field at layer 5. B) Temperature field at layer 15. C) Temperature field at layer 20

A quantitative validation of the temperature predictions was also carried out. Time-temperature history was extracted at five different layer locations starting at layer 4 and increasing in an interval of four layers until layer 20. The locations of data extraction for both the simulations and experiments are shown in Figure 131. The temperature was extracted at the top of each bead represented in the simulation and the same was carried out for the experimental measurements.

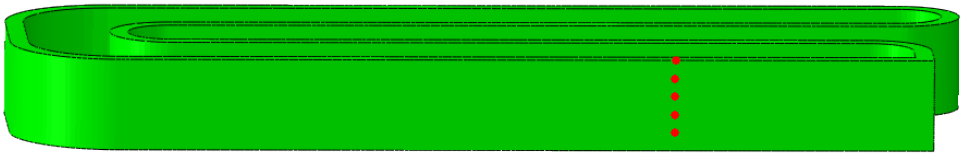

Figure 131 - Layer locations in the curved wedge used for extracting time-temperature history

Figure 132 shows the experimental and predicted transient temperature evolution at five different layers. The temperature predictions are in the worst case within $\pm 20\ ^{\circ}C$ of the experimental measurements. This great agreement between the simulations and the experimental measurements demonstrates that the relevant heat transfer mechanisms developed during the printing process are captured. The process simulations capture the rapid cooling developed at the surface of the printed bead upon being deposited (Figure 132). Such a behavior is caused by heat losses through radiation and through conduction with the surrounding material and with the material compacter. The spikes following the rapid cooling represents the deposition of molten material on top of the observed bead. This is seen for the first four layers under observation in Figure 132 (i.e., layer 4, layer 8, layer 12, and layer 16). The final layer (layer 20 in Figure 132) cools at a faster rate than the previous layers owing to the additional area exposed on top of the bead after all the layers have been deposited.

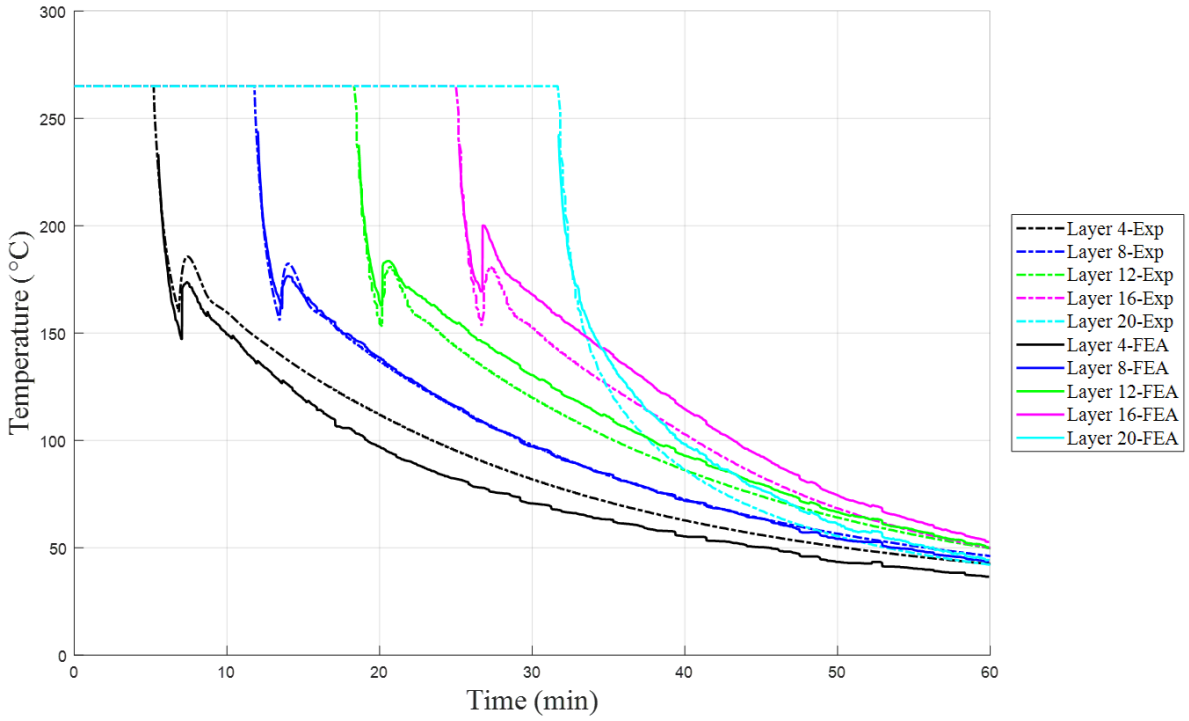

Figure 132 - Comparison of time-temperature history measured experimentally and predicted with process simulation for different layers in the racetrack

The predictions for deformation or shape change after removal from the build plate was also validated with the racetrack. The displacement caused by the "spring in" at the ends of the racetrack was used for validating the deformation predictions. Figure 133 shows the location in the racetrack where the deformation was measured experimentally and extracted from the process simulations. The same image also shows a great agreement between the experimental measurements and the simulation predictions. A difference of less than 2% was observed between the experimental measurements and the simulation predictions.

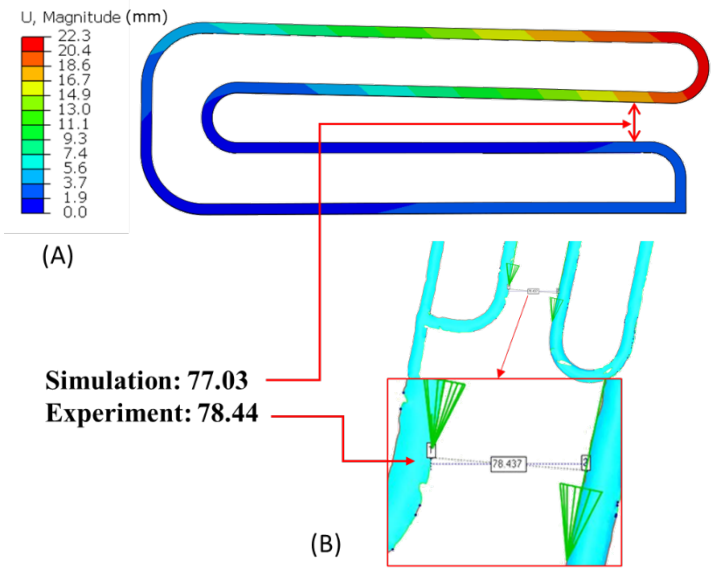

Figure 133 - Comparison of deformation developed at end of racetrack

Predictions for temperature and deformation were carried out for two geometries, a plate with antisymmetric print orientation and a racetrack. Temperature predictions were in great agreement with the experimental measurements; generally, within $\pm 20\ ^{\circ}C$ from the experimental measurements. Similarly, the predictions for deformation were in great agreement with experimentally measurements; in the worst case withing 7% from the experimental measurements. Finally, these results demonstrate that milestone 3.12.4.2 has been fulfilled and provided positive confidence for the go/no-go gate decision 3.12.3 related to predicting full field strains withing 10% of tests results.

Sub-element Structural Simulation

Milestone 3.12.4.1 Structural simulations of the sub-element tests from the first phase work (Project 3.6) have been completed and report delivered to Local Motors and briefed to DOE.

A box design printed in a previous IACMI program (Project 3.6) was selected to demonstrate the structural analysis carried out with ADDITIVE3D©. The manufacturing process of the box design was simulated with ADDITIVE3D© and the outcome of the manufacturing process, namely residual stresses, and local material orientation, was mapped to a performance analysis where the bending stiffness of the structure was analyzed. Figure 134 (A) shows the geometry of the subcomponent selected which is referred to as box with W infill. Similarly, Figure 134 (B) shows the voxel mesh used in both the additive process simulation and the structural analysis of the printed subcomponent.

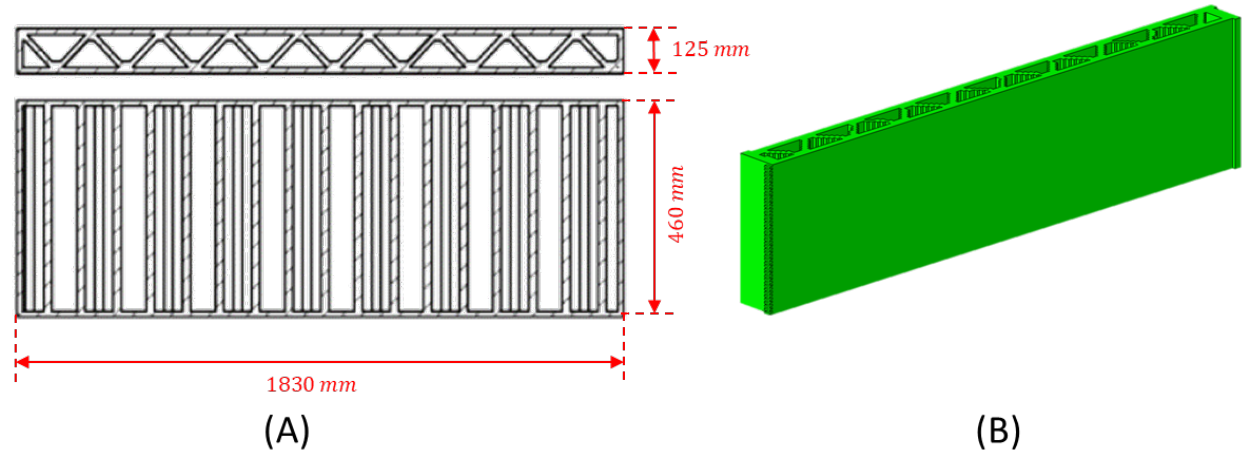

Figure 134 - Printed subcomponent with W infill architecture

The process simulation used the machine code generated from the slicing process and the material card generated for CF-PC. Figure 135 shows the evolution of temperature, stresses (σ_{33}), and displacement (U_3) developed in the 3-direction at the beginning of the printing process (A), halfway through the printing process (B), and end of the printing process (C).

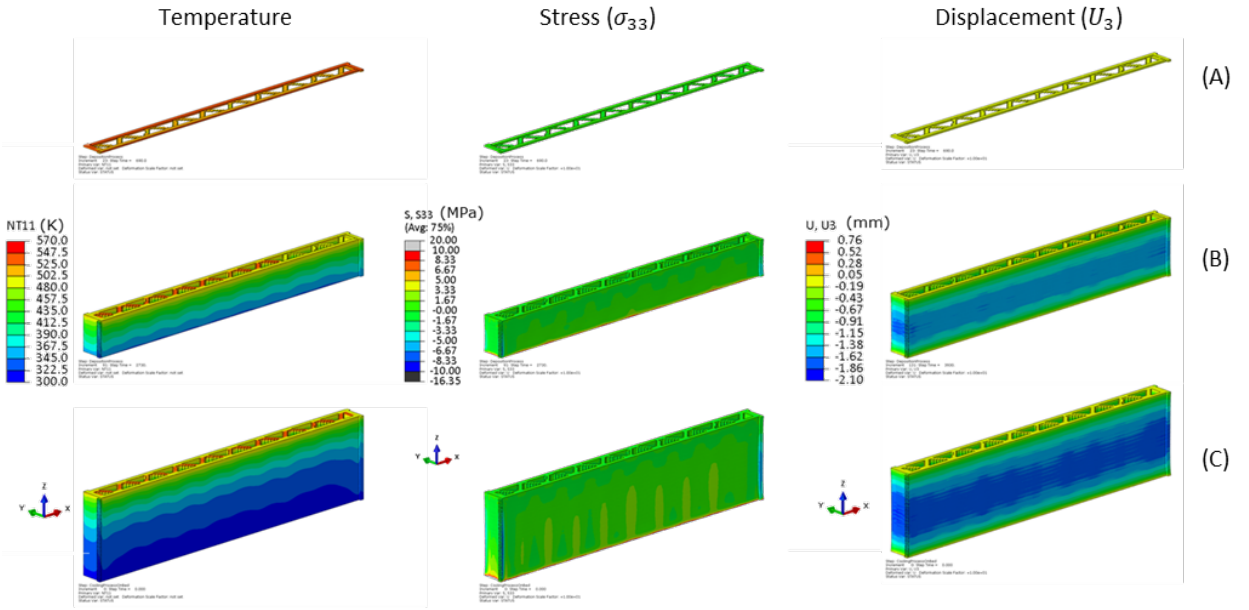

Figure 135 - Results of additive process simulation. Temperature, stress, and displacement developed at: A) Beginning of the printing process. B) Halfway through the printing process. C) End of the printing process.

Figure 135 shows the large temperature gradients that develop during the printing process along the 3-direction. Further, temperature gradients also lead to internal stresses due to differences in solidification and thermal shrinkage between adjacent layers. Stresses in the 3-direction are shown to develop primarily at the bottom where the printed part is attached to the build plate. Upon removal of the part from the build plate, internal stresses re-equilibrate which leads to a combination of deformation and residual stresses in the printed part. The coefficient of thermal expansion in the 3-direction is the highest of the three directions and shrinkage occurs as the material cools from the melt temperature to the ambient temperature. This results into changes in effective layer height as the print gains height during the process. Figure 135 shows

the displacement in the 3-direction that develops primarily due to the shrinkage in the 3-direction. Further shrinkage occurs in the 3-direction as the printed part cools down to the ambient temperature.

After performing the additive process simulation of the box with W infill, the performance under four-point bending was investigated with ADDITIVE3D©. Figure 136 shows the testing rig developed at Local Motors for four-point bending and the four-point bending conditions used to analyze the printed box with W infill. The performance analysis carried out with ADDITIVE3D© captured the residual stresses developed and the local material orientation resulting of the additive process.

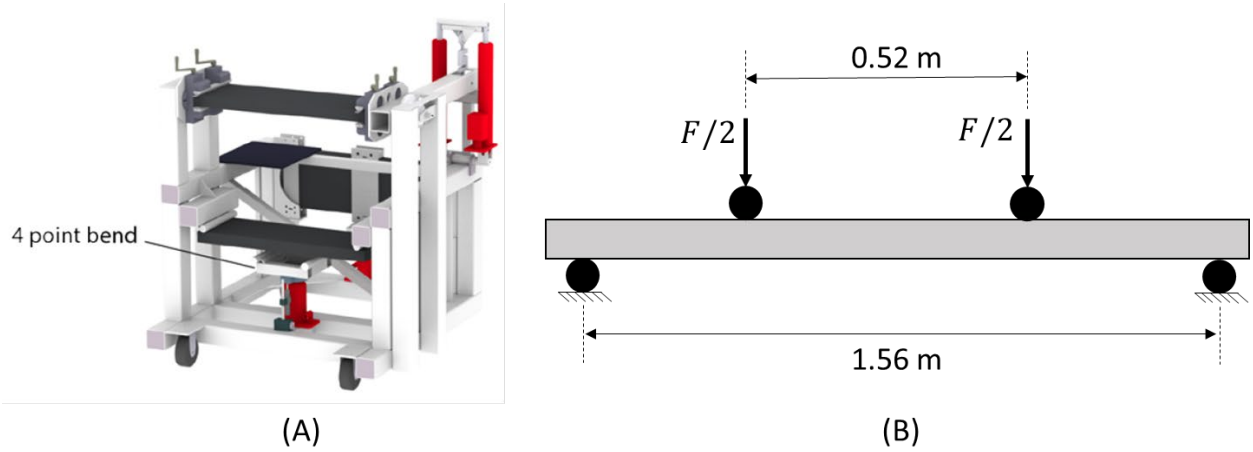

Figure 136 - Four-point bending. A) Testing rig developed at Local Motors for four-point bending. B) Schematic representation of the four-point bending conditions used to analyze the printed box with W infill.

The four-point bending test carried out virtually was displacement controlled with a maximum displacement of 10 mm at the two middle points of load introduction. Figure 137 shows the fields of normal stresses (1-direction) and shear stresses (1-2 plane) developed for a displacement of 5 and 10 mm.

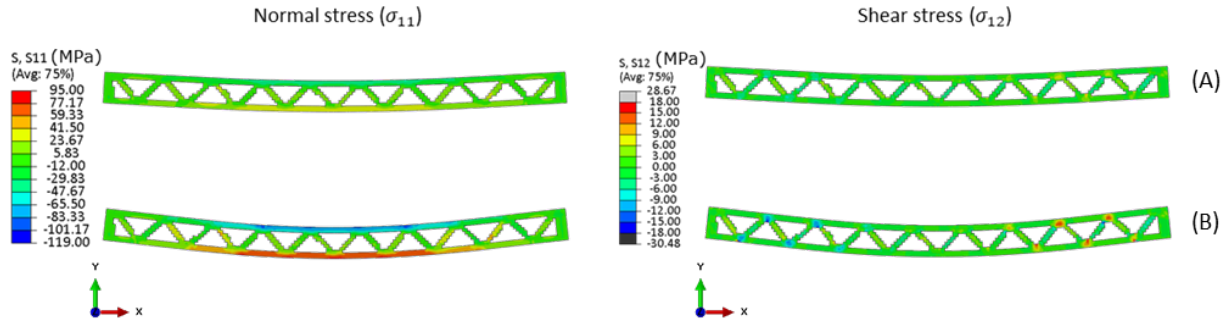

Figure 137 - Stress field developed during four-point bending under displacement control conditions. A) At 5 mm of displacement. B) At maximum displacement of 10 mm.

The stress levels developed at the maximum displacement of 10 mm (Figure 137 – B) indicate potential failure in shear at the joints between the infill and the perimeter layer in the printed box, whereas the lower side of the printed box develops tensile stresses that are near the ultimate tensile strength of the CF-PC. Significant compressive stresses develop also in the upper side of the printed box, however, the compressive strength of this class of material systems can be greater than the tensile strength. Future work should also consider characterizing the compressive behavior of printed material systems.

The bending stiffness was used to quantify the structural performance of the printed box. The reaction force at the two regions of load introduction and the displacement was used to compute bending stiffness ($K =$

$F/Deflection$). A bending stiffness of 87.5 KN/mm was obtained for the box with the W infilled. This work fulfills the goal of milestone 3.12.4.1 focused on demonstrating the use of ADDITIVE3D© to perform structural simulations of printed components in the as-manufactured state.

5. BENEFITS ASSESSMENT

This work has benefitted by making LSED more easily utilizable in a structural application. The more applications that LSED can be utilized for efficiently, the more areas it will have an impact on decreasing the embodied energy and carbon emissions in the production process. This is especially true when as it is possible to recycle these structures after their life cycle has been completed. The advancement of multimaterial structures also represents a step towards tunable large structures from the LSED process. As the feasibility of these tunable structures increase so will the likelihood of multimaterial LSED being commercialized.

6. COMMERCIALIZATION

The technology is currently being utilized by Local Motors to produce their Olli, which is deployed in several locations around the world at the release of this report. There are more companies adopting large scale additive manufacturing to create things such as furniture, boats, and architectural pieces. Thus, commercialization of this technology is well underway. The commercialization plan for this technology is to continue developing tools and materials that make it more easily utilizable in more scenarios. This includes better software, hardware, and design tools. Development of life cycle options, printing recycled or upcycled materials and recycling or upcycling printed materials, for the material once it has been used will also increase commercialization, due to a decrease in environmental impact.

7. ACCOMPLISHMENTS

i) Publications in scientific/ trade journals, conference proceedings etc.
   a. IACMI Members Meeting (July 2019)
   b. IACMI/GACC Lightweight Materials Conference (Oct 2019)
   c. Carbon Fiber Conference (Nov 2019)
   d. IACMI Members Meeting (Jan 2020)
   e. SPE ACCE Poster session (Sept. 2020)

ii) Graduate student's thesis based on the project work
   a. Akshay J. Thomas

iii) Non-thesis graduate research based on project work
   a. William Henken
   b. Frye Mattingly
   c. Dylan Hoskins

iv) Other products (e.g., software, data bases, inventions)
   a. Development of NDE approach for identifying print defects
   b. Development of an in-situ process monitoring methodology for measuring bead width and bead height in a large area additive manufacturing machine using profilometry

8. CONCLUSIONS

The work performed for this project has advanced the understanding of using LSED for structural applications. A new material, currently utilized by Local Motors in Olli, was investigated thoroughly to have a deeper understanding of the effect of print parameters on the material. An understanding of these parameters is key when designing and manufacturing parts for structural applications. Because in structural applications where safety is of a concern it is important to understand what material properties can be expected from a given set of print parameters. A thorough study on crack propagation was also performed which is still a topic that does not have large amounts of literature in LSED.

This project also utilized ORNL's multi-material printing capabilities in an important use case for structural application. The ability to increase energy absorption in a smaller design envelope and with a lighter part is very appealing in environments where space and weight are a valuable commodity, such as aerospace or vehicles. The current designs can likely be improved to further increase their applicability. Results from the experimentation also open the door to more possibilities for multi-material printing as the technology grows and becomes more available.

In process monitoring improvements and novel NDE techniques were developed during the duration of this work. The ability to track bead width and look for abnormalities and defects during printing is a valuable ability when creating parts for structural applications since in-situ data improve confidence in the part before being sold or to determine population affected. The consistency of bead width and height with a given scaling of parameters also gave insight into the process variability. A novel way to inspect parts for defects was also created. This inspection method would allow for defects in parts to be quickly and easily identified. Defects that could impact the structural integrity are important to be able to detect from a quality and safety standpoint before they are sold. Material property and bead width variation in manufacturing process was determined as well as critical factors for part quality and Z-direction strength.

The final major benefit was further progress in the development of simulation for additive manufacturing. Simulation for additive manufacturing, especially for large structures, will increase the attractiveness of LSED for more use cases. The ability to iteratively improve a design is one of the strengths of additive manufacturing, thus being able to simulate and improve structures continuously would further increase the flexibility and benefits of additive manufacturing. This works showed the ability to accurately predict print warpage of printed parts using a finite element-based simulation.

9. RECOMMENDATIONS

Recommendations for further research would be the utilization of print simulation on large complex structures to determine the error between simulation and experimental. Based on the results optimization of the FEA simulation for large parts (> 1 m^3) would be very useful as more parts of this scale are being created as LSED continues to grow in utilization. This may also lead to the development of new techniques centered around accurately modeling both the LSED process and behavior of LSED parts. The other recommendation would be further research on the multimaterial structures. Research centered around design rules and designing for multimaterial LSED would benefit commercialization of the technology and likely reveal important information about fundamental LSED process questions. It could also develop the method for tuning these structures to arrive at a desired behavior or bulk property. All of these would allow for an improvement in utilization of multimaterial LSED printing.

10. REFERENCES AND/OR BIBLIOGRAPHY

[1] M. Annunziata, "Reinventing Mobility And Manufacturing At Once: Local Motors," *Forbes*,

2020. https://www.forbes.com/sites/marcoannunziata/2020/03/17/reinventing-mobility-and-manufacturing-at-once-local-motors/?sh=34c460a660d8 (accessed Nov. 10, 2021).
[2] B. P. Heller, D. E. Smith, and D. A. Jack, "Planar deposition flow modeling of fiber filled composites in large area additive manufacturing," *Addit. Manuf.*, vol. 25, pp. 227–238, 2019, doi: 10.1016/j.addma.2018.10.031.
[3] C. E. Duty *et al.*, "Structure and mechanical behavior of Big Area Additive Manufacturing (BAAM) materials," *Rapid Prototyp. J.*, vol. 23, no. 1, pp. 181–189, 2017, doi: 10.1108/RPJ-12-2015-0183.
[4] A. Wedgewood, P. Pibulchinda, E. Barocio, C. Hill, and M. Bogdanor, *Materials Development and Advanced Process Simulation for Additive Manufacturing with Fiber-Reinforced Thermoplastics*. 2020.
[5] B. Brenken, E. Barocio, A. Favaloro, V. Kunc, and R. B. Pipes, "Development and validation of extrusion deposition additive manufacturing process simulations," *Addit. Manuf.*, vol. 25, pp. 218–226, 2019, doi: 10.1016/j.addma.2018.10.041.
[6] P. Chesser *et al.*, "Extrusion control for high quality printing on Big Area Additive Manufacturing (BAAM)systems," *Addit. Manuf.*, vol. 28, no. May, pp. 445–455, 2019, doi: 10.1016/j.addma.2019.05.020.
[7] M. Borish, B. K. Post, A. Roschli, P. C. Chesser, L. J. Love, and K. T. Gaul, "Defect Identification and Mitigation Via Visual Inspection in Large-Scale Additive Manufacturing," *Jom*, vol. 71, no. 3, pp. 893–899, 2019, doi: 10.1007/s11837-018-3220-6.
[8] J. Brackett *et al.*, "Characterizing material transitions in large-scale Additive Manufacturing," *Addit. Manuf.*, vol. 38, p. 101750, 2021, doi: 10.1016/j.addma.2020.101750.
[9] P. M. Bhatt, R. K. Malhan, A. V. Shembekar, Y. J. Yoon, and S. K. Gupta, "Expanding capabilities of additive manufacturing through use of robotics technologies: A survey," *Addit. Manuf.*, vol. 31, p. 100933, 2020, doi: 10.1016/j.addma.2019.100933.
[10] H. Shen, L. Pan, and J. Qian, "Research on large-scale additive manufacturing based on multi-robot collaboration technology," *Addit. Manuf.*, vol. 30, p. 100906, 2019, doi: 10.1016/j.addma.2019.100906.
[11] A. Standard, "E1269, 2005,'Standard Test Method for Determining Specific Heat Capacity by Differential Scanning Calorimetry,' ASTM International, West Conshohocken, PA." .
[12] ASTM, "Standard test method for thermal diffusivity of solids by the flash method (E1461-01)," *Am. Soc. Test. Mater.*, vol. 14, no. 2, pp. 1–13, 2001, doi: 10.1520/E1461-13.2.
[13] H. F. Brinson and L. C. Brinson, *Polymer engineering science and viscoelasticity: An introduction, Second edition*. 2015.
[14] B. Brenken, E. Barocio, A. Favaloro, V. Kunc, and R. B. Pipes, "Development and validation of extrusion deposition additive manufacturing process simulations," *Addit. Manuf.*, vol. 25, 2019, doi: 10.1016/j.addma.2018.10.041.
[15] S. P. C. Marques and G. J. Creus, "Computational viscoelasticity," *SpringerBriefs Appl. Sci. Technol.*, no. 9783642253102, pp. iv–v, 2012, doi: 10.1007/978-3-642-25311-9.
[16] B. Fan and D. O. Kazmer, "Low-temperature modeling of the time-temperature shift factor for polycarbonate," *Adv. Polym. Technol.*, vol. 24, no. 4, pp. 278–287, 2005, doi: https://doi.org/10.1002/adv.20049.
[17] R. A. Schapery, "A method of viscoelastic stress analysis using elastic solutions," *J. Franklin Inst.*, vol. 279, no. 4, pp. 268–289, 1965, doi: https://doi.org/10.1016/0016-0032(65)90339-X.
[18] E. A. Papon and A. Haque, "Fracture toughness of additively manufactured carbon fiber reinforced composites," *Addit. Manuf.*, vol. 26, pp. 41–52, Mar. 2019, doi: 10.1016/J.ADDMA.2018.12.010.
[19] N. Aliheidari, R. Tripuraneni, A. Ameli, and S. P. V Nadimpalli, "Fracture resistance measurement of fused deposition modeling 3D printed polymers," *Polym. Test.*, vol. 60, pp. 94–101, 2017.
[20] J. P. Isaac, S. Dondeti, and H. V Tippur, "Fracture behavior of additively printed ABS: Effects of

print architecture and loading rate," *Int. J. Solids Struct.*, vol. 212, pp. 80–95, 2021, doi: https://doi.org/10.1016/j.ijsolstr.2020.11.027.
[21] X.-K. Zhu and J. A. Joyce, "Review of fracture toughness (G, K, J, CTOD, CTOA) testing and standardization," *Eng. Fract. Mech.*, vol. 85, pp. 1–46, 2012, doi: https://doi.org/10.1016/j.engfracmech.2012.02.001.
[22] ASTM International, "ASTM D5045 - 14 Standard Test Methods for Plane-Strain Fracture Toughness and Strain Energy Release Rate of Plastic Materials." 2014.
[23] D. Lee, H. Tippur, M. Kirugulige, and P. Bogert, "Experimental Study of Dynamic Crack Growth in Unidirectional Graphite/Epoxy Composites using Digital Image Correlation Method and High-speed Photography," *J. Compos. Mater.*, vol. 43, no. 19, pp. 2081–2108, Jul. 2009, doi: 10.1177/0021998309342139.
[24] G. C. Sih, P. C. Paris, and G. R. Irwin, "On cracks in rectilinearly anisotropic bodies," *Int. J. Fract. Mech.*, vol. 1, no. 3, pp. 189–203, 1965, doi: 10.1007/BF00186854.
[25] Robert Bedsole, "High Strain Rate Elastic and Fracture Characterization of Isotropic and Orthotropic Materials with and without Nano Fillers," 2015.
[26] H. Uete and R. M. Caddell, "Determination of the fracture toughness of polycarbonate using an energy approach," *Int. J. Mech. Sci.*, vol. 25, no. 2, pp. 87–92, 1983, doi: https://doi.org/10.1016/0020-7403(83)90002-4.
[27] A. Salazar, J. Rodríguez, and A. B. Martínez, "Fracture Toughness Reliability in Polycarbonate: Notch Sharpening Effects," *Indian J. Mater. Sci.*, vol. 2013, p. 187802, 2013, doi: 10.1155/2013/187802.
[28] P. C. Tyler Smith, Ahmed Arabi Hassen, Randall Lind, John Lindahl and L. L. and V. K. Alex Roschli, Vipin Kumar, Vidya Kishore, Brian Post, Jordan Failla, Chad Duty, "Dual Material System for Polymer Large Scale Additive Manufacturing," *SAMPE Conf.*, 2020.
[29] M. Capriotti, S. Sternini, F. Lanza di Scalea, and S. Mariani, "Extraction of thermal Green's function using diffuse fields: a passive approach applied to thermography," *Sensors Smart Struct. Technol. Civil, Mech. Aerosp. Syst. 2016*, vol. 9803, p. 98030U, 2016, doi: 10.1117/12.2218998.
[30] E. Barocio, B. Brenken, A. Favaloro, M. Bogdanor, and R. B. Pipes, *Extrusion deposition additive manufacturing with fiber-reinforced thermoplastic polymers*. Elsevier Inc., 2020.
[31] E. Barocio, "Fusion Bonding of Fiber Reinforced Semi-Crystalline Polymers in Extrusion Deposition Additive Manufacturing," Ph.D. Dissertation - Purdue University, 2018.
[32] B. Brenken, "Extrusion Deposition Additive Manufacturing of Fiber Reinforced Semi-crystalline Polymers," Ph.D. Dissertation - Purdue University, 2017.
[33] D. W. Radford and R. J. Diefendorf, "Shape Instabilities in Composites Resulting from Laminate Anisotropy," *J. Reinf. Plast. Compos.*, vol. 12, no. 1, pp. 58–75, 1993, doi: 10.1177/073168449301200104.

11. APPENDICES

A. Raw Porosity data from image analysis and images of samples

Set A			
	A1	**A2**	**A3**
Layer Time (min)	*2:20*	*3:20*	*4:20*
Bead Porosities (%) 1	6.2	10.0	8.5
2	5.7	7.1	7.1
3	5.9	7.0	6.9

4	5.3	7.4	6.6
5	6.8	7.8	5.1
6	6.6	9.2	7.7
Average (%)	6.1	8.1	7.0
Std. Dev. (%)	0.5	1.1	1.1
S.D. / Avg (%)	8.2	13.6	15.7

Set B			
	B1	**B2**	**B3**
Print Speed (in/min)	*100*	*300*	*500*
Bead Porosities (%) 1	7.3	6.0	6.3
2	6.5	5.8	6.5
3	6.5	5.4	5.3
4	7.7	4.8	5.3
5	7.9	4.8	5.7
6	9.5	5.5	6.4
Average (%)	7.6	5.4	5.9
Std. Dev. (%)	1.0	0.5	0.5
S.D. / Avg (%)	13.2	9.3	8.5

Set C						
	C1	**C2**	**C3**	**C4**	**C5**	**C6**
Bead Aspect Ratio & Bead-to-Nozzle-Area Ratio	*3, 0.77*	*4, 0.77*	*5, 0.77*	*3, 0.97*	*4, 0.97*	*5, 0.97*
Bead Porosities (%) 1	8.4	8.5	10.2	4.7	12.2	12.3
2	8.1	8	9.2	4.5	11.5	11.4
3	7.9	7.8	8.8	4.5	11.5	11
4	7.7	7.8	8.6	5.1	12.2	10.5
5	8.7	8.3	8.5		12.9	11.2
6			8.5			
Average (%)	8.2	8.1	9	4.7	12	11.3
Std. Dev. (%)	0.3	0.3	0.6	0.3	0.5	0.6
S.D. / Avg (%)	3.7	3.7	6.7	6.4	4.2	5.3

Set D		
	D1	**D2**
Nozzle Size (in diam)	*0.3*	*0.4*
Bead Porosities (%) 1	10.1	13.5
2	10	11.2
3	10.1	10.8
4	10.5	10.3
5	10.9	10.6
6	10.8	10.5
7	10.3	11.2
8	9.1	
9	10	
Average (%)	10.2	11.1
Std. Dev. (%)	0.5	1

S.D. / Avg (%)	4.9	9.0

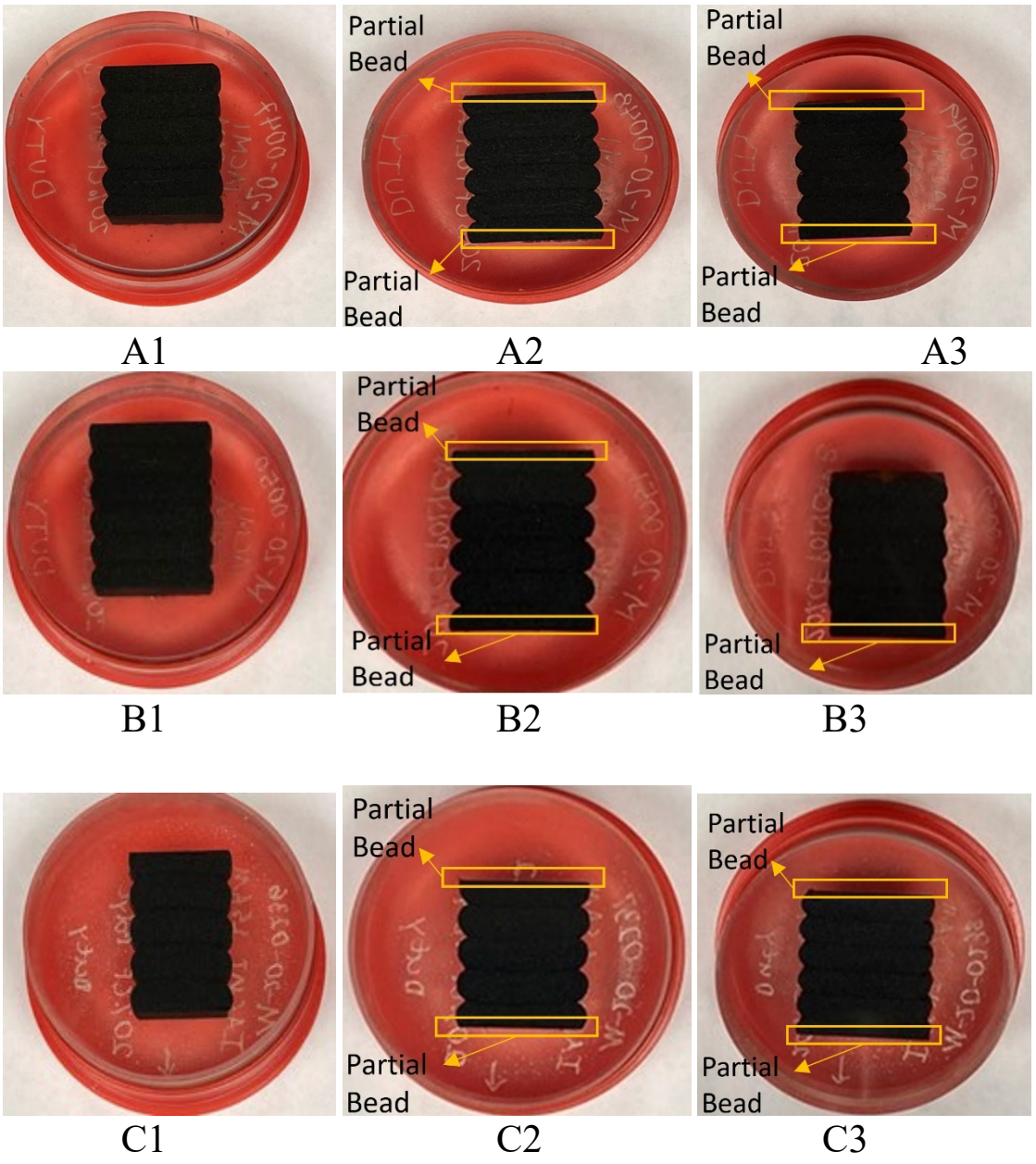

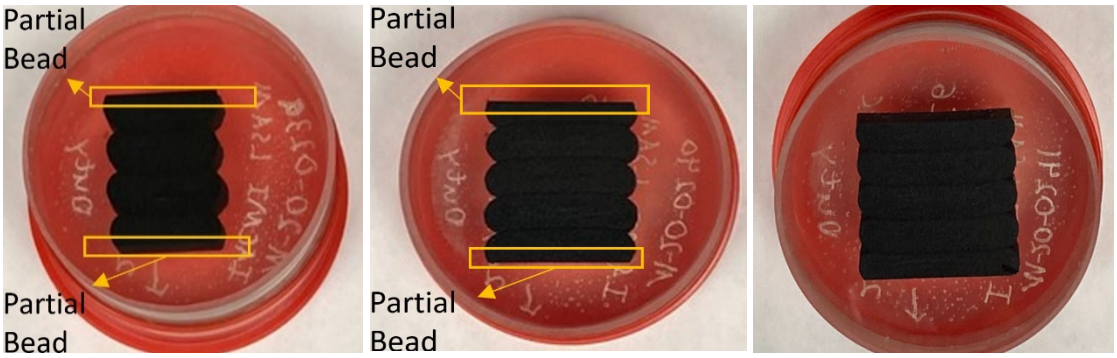
Partial
Bead
Partial
Bead
Partial
Bead
Partial
Bead

C4 C5 C6

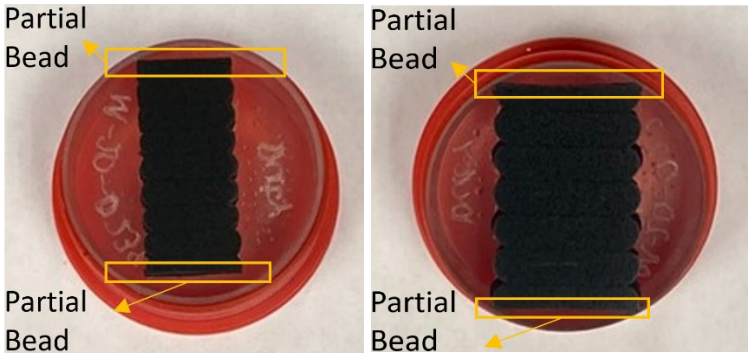
Partial
Bead
Partial
Bead
Partial
Bead
Partial
Bead

D1 D2